Faculté des Sciences Appliquées
École Polytechnique

Université Libre de Bruxelles,
Université d'Europe

ULB

Analytical and numerical studies of transverse beam splitting used for the CERN PS Multi-Turn Extraction

Cédric Hernalsteens

CERN-THESIS-2011-446
//2011

Mémoire présenté en vue de l'obtention
du grade d'Ingénieur Civil physicien,
orientation physique appliquée

Promoteurs:

Pr. Dr. Ir. Alain Dubus

ULB — Faculté des Sciences Appliquées — Service de Métrologie Nucléaire

Pr. Ir. Django Manglunki

CERN — Beams department — Operations group

Superviseur CERN:

Dr. Massimo Giovannozzi

CERN — Beams department — Accelerators and Beam Physics group

European Organization for Nuclear Research
Organisation Européenne pour la Recherche Nucléaire

Année académique 2010 – 2011

To Axelle,
for her invaluable support during these last three years.

Abstract

In view of the programme of reduction of beam losses in the PS for the high intensity beams, in particular that for the CNGS experiment, a novel extraction method was designed for beam transfer between the PS to the SPS. This method, called Multi-Turn Extraction (MTE) is based on the splitting of the proton beam in the horizontal transverse phase space by means of sextupoles and octupoles, using a specific tune variation. The split beam exhibits five beamlets: the core and four islands where a fraction of the beam is trapped.

This work analyses numerically and analytically the properties of the beam splitting in view of proposing possible optimizations regarding the trapping of the particles in the islands. We first introduce theoretical models describing this process, from the point of view of the Hamiltonian theory and the transfer map formalism of beam dynamics. The generalized Hénon mapping is then considered to describe the dynamics of the MTE method. We then use the Normal Form approach to analytically obtain properties of that model.

In order to explore the properties of the MTE method, we simulate numerically the evolution of the beam in the framework of the 2D and 4D Hénon models. We present a tracking code that we developed to assess the properties of the splitting process.

An extensive 2D simulation campaign has been performed to understand the effects of the parameters of the mappings on the fraction of particles trapped in the islands and on the emittances of the different beamlets. We determine the influences of physical parameters (strength of the nonlinearities and tune variation) on the trapping process and we propose ways to improve the trapping and the emittance sharing. In addition, we present results obtained from 4D simulations to investigate new effects introduced by the nonlinear coupling between the horizontal and vertical planes.

Résumé

Dans le cadre du programme de réduction des pertes pour des faisceaux de hautes intensités dans le PS, en particulier les faisceaux pour l'expérience CNGS, une nouvelle méthode d'extraction a été conçue pour le transfert de faisceaux du PS vers le SPS. Cette méthode, baptisée Multi-Turn Extraction (MTE) est basée sur la fragmentation du faisceau de protons dans l'espace des phases horizontal au moyen de sextupoles et d'octupoles, en utilisant une variation de tune particulière. Le faisceau est ainsi divisé en cinq parties : le coeur et quatre îlots dans lesquels une fraction du faisceau se retrouve trappée.

Ce travail analyse numériquement et analytiquement les propriétés de la division du faiseau en vue de proposer une possible optimisation du processus de capture des particles dans les îlots. Premièrement nous introduisons des modèles théoriques décrivant le processus, du point de vue de la théorie Hamiltonienne et du formalisme des fonctions de transfert de la dynamique de faisceau. Ensuite nous utilisons l'approche des formes normales pour comprendre analytiquement certaines propriétés du modèle.

Afin d'explorer en détails les propriétés de la méthode MTE, nous simulons numériquement l'évolution du faisceau dans le cadre des modèles de Hénon 2D et 4D. Nous présentons alors un code numérique que nous avons développé, destiné à analyser les propriétés du processus de division du faisceau.

Une large campagne de simulations 2D a été menée afin de comprendre l'influence des paramètres du mapping sur la fraction de particules trappées dans les lots et sur les émittances des différentes parties du faisceau. Nous déterminons donc l'influence de paramètres physiques (forces des non-linéarités et variation du tune) sur le processus de capture et nous proposons des moyens permettant d'améliorer la capture et le partage d'émittance entre les différentes parties de faisceau. En outre, nous présentons des résultats de simulations 4D permettant d'investiguer les effets introduits par le couplage non linéaire entre le plan horizontal et le plan vertical.

Contents

1 Introduction **1**

2 Single particle dynamics in a synchrotron **3**
2.1 Overview of synchrotron machines . . . 4
2.1.1 Historical introduction to particle accelerators physics . . . 4
2.1.2 Highlights about synchrotrons . . . 6
2.2 Transverse dynamics . . . 10
2.2.1 Reference frame . . . 10
2.2.2 Intuitive derivation of Hill's equation . . . 12
2.2.3 Betatron dynamics in the Hamiltonian formalism . . . 14
2.3 Transverse motion in the transfer maps formalism . . . 22
2.3.1 Symplectic matrices and maps . . . 23
2.3.2 Poincaré map and orbit tracking . . . 24
2.3.3 Linear transfer maps and linear normal forms . . . 25
2.3.4 Nonlinear transfer maps . . . 30

3 The Multi-Turn Extraction method **34**
3.1 Introduction to the CERN accelerator complex . . . 34
3.1.1 The CERN Proton Synchrotron machine . . . 36
3.1.2 Overview of extraction methods used at the Proton Synchrotron (PS) . . . 38
3.1.3 The CNGS experiment . . . 40
3.2 Specific methods used for the PS to Super Proton Synchrotron (SPS) transfer . . . 41
3.2.1 The CT method . . . 41
3.2.2 The MTE method and its implementation . . . 42
3.3 The modeling of the MTE method and the Hénon mapping . . . 45
3.3.1 Model for the MTE beam splitting . . . 45
3.3.2 The Hénon mapping and its fixed points . . . 47
3.3.3 Overview of the trapping process . . . 50

4 Analytical study of MTE: a Normal Form approach **52**
4.1 Normal forms: definition and construction . . . 52
4.1.1 Definition of the normal forms . . . 53
4.1.2 Construction of normal forms for 2D maps . . . 55
4.2 The quasi-resonant normal form of the Hénon map . . . 56
4.2.1 Explicit construction . . . 56
4.2.2 The quasi-resonant Normal Form . . . 58
4.3 Interpolating Hamiltonian of the Hénon map from normal form analysis . . . 58

4.3.1 Definition of the interpolating Hamiltonian . . . 58
4.3.2 Analysis of the fourth order resonance . . . 61
4.4 Analytical model of the trapping probability for MTE . . . 63

5 Manzoni: a numerical tool to study the MTE dynamics 65
5.1 Numerical tools for the study of beam dynamics . . . 65
5.2 Manzoni: a code for the tracking of symplectic mappings . . . 66
5.2.1 Comparison with the MTE Fortran code . . . 67
5.2.2 Implementation of the physical aspects of the beam tracking . . . 67
5.3 Setup of the simulations . . . 69
5.3.1 Initial beam distribution . . . 69
5.3.2 Parameters of the mapping . . . 69
5.4 Output of the simulations . . . 71
5.4.1 Histograms and plots . . . 71
5.4.2 Moments and population of the beamlets . . . 71
5.4.3 FFT analysis . . . 72

6 2D numerical studies of the MTE dynamics 74
6.1 Numerical study of the 2D generalized Hénon mapping . . . 75
6.2 Parametric dependence of the trapping fraction . . . 75
6.2.1 Comparison of methods used to compute the trapping fraction . . . 75
6.2.2 Effect of the initial beam emittance . . . 76
6.2.3 Comparison between a Gaussian and a uniform beam distribution . . . 78
6.2.4 Effect of the slope of the tune variation . . . 80
6.2.5 Effect of the functional form of the tune variation . . . 82
6.2.6 Effect of the value of κ . . . 82
6.3 Global fitted model of the trapping fraction . . . 87
6.4 Minimal trapping amplitude . . . 89
6.5 Parametric dependence of the emittance sharing between the beamlets . . . 90
6.5.1 Islands and core emittances ratio . . . 90
6.5.2 Tune curve slope effect on the emittance sharing . . . 92
6.5.3 Effect of the variation of κ on the emittances ratio . . . 93
6.6 Conclusions on the 2D numerical studies . . . 94

7 4D numerical studies of the MTE dynamics 96
7.1 Numerical study of the 4D generalized Hénon mapping . . . 96
7.2 Effects of the vertical emittance on the trapping fraction . . . 97
7.3 Emittance sharing in 4D . . . 98
7.4 Evolution of the vertical emittance . . . 100
7.5 Digression: double resonance crossing . . . 100
7.6 Conclusions on the 4D numerical studies . . . 101

8 Conclusion and perspectives 103

A Formal computation of Normal Form coefficients 105
A.1 Quasi-resonant Normal Form (fifth order resonance) . . . 105
A.1.1 Conjugating function . . . 105

A.1.2 Normal form 106
A.2 Nonresonant Normal Form 106
A.2.1 Conjugating function 106
A.2.2 Normal Form 107

B Typical simulation input file for Manzoni **108**
B.1 Input file 108

Bibliography **112**

Index **116**

List of Figures

2.1 Schematics of the "Wideroe Linac", the ancestor of modern RF-LINACs, using the principle of resonant acceleration (from Ref. [1]). 5
2.2 The Low Energy Ion Ring (LEIR) synchrotron at European Organization for Nuclear Research (CERN) [2]. (a) Dipolar bending magnet (b) Quadrupoles (c) Beam pipe (d) Injection and extraction lines (e) RF-cavities. 7
2.3 Schematics of the magnetic field of a quadrupole (from Ref. [3]). 9
2.4 Curvilinear coordinates system based on the reference trajectory. The origin of the $\boldsymbol{r}$-coordinate is arbitrary in the laboratory frame. 11
2.5 An idealized accelerator whose magnetic elements are piecewise constant. Each is represented by its transfer map from coordinates s_{i-1} to s_i. 22
2.6 Beta-functions and dispersion of a periodic ring made of seven FODO cells. Obtained with [4] 27

3.1 CERN accelerators complex schematic overview (from Ref. [5]). The path followed by the CERN Neutrino to Gran Sasso experiment (CNGS) proton beam is highlighted. 35
3.2 Schematic of a PS main magnetic unit (from Ref. [6]). 37
3.3 Pictures of the PS straight section 55 (from Ref. [7]): (left) on the right side of the picture, SS55 is shown and from right to left it shows a main magnetic unit, the SS56 and another MU (right) SS55 is shown from the other side. 37
3.4 A typical sequence of beams in the PS. The light overlays shows two CNGS beams produced by the PS machine (from Ref. [8]). 38
3.5 Orbit in the PS prior to a fast-extracted toward the East Hall (from Ref. [9]). . . . 39
3.6 Schematic layout of the CNGS facility on the CERN side (from Ref. [10]). 41
3.7 Schematic principle of the Continuous Transfer (CT) extraction (from Ref. [11]). (left) The PS ring and the main elements used for the extraction; (top right) the strength of the kicker magnets as a function of time and (bottom right) the regions of the shaved beam represented in the horizontal phase space of the beam. 42
3.8 3D representation of the four beamlets along the ring (from Ref. [12]). 44
3.9 Beam distribution in physical space: beam splitting in the PS and observation in the transfer line TT2 (from Ref. [12]). 44
3.10 Phase space topology of the quadratic Hénon mapping. Green dots are the elliptic fixed points and red dots are the hyperbolic ones (obtained with GIOTTO [13].) . 49
3.11 Phase space evolution during the trapping process. (left) Topology obtained with GIOTTO. (right) Numerical trapping simulation performed with Manzoni (see chapter 5). 51

4.1 Phase space topology of the quadratic 2D Hénon mapping with $\omega/2\pi = 0.251$ and of the associated quasi-resonant normal form for the fourth order resonance. 59
4.2 Phase space topology of the quadratic 2D Hénon mapping with $\omega/2\pi = 0.255$ and of the associated quasi-resonant normal form for the fourth order resonance. 60
4.3 Phase space topology of the Hamiltonian (4.33) for $\omega = 2\pi \times 0.255$ and $\kappa = 0$. . . 62
4.4 Phase space topology of the Hamiltonian of the fifth order resonance for $\omega = 2\pi \times 0.201$ and $\kappa = 0$. 63

5.1 Typical histograms of the beam distribution in the subspaces of the 4D phase space at the end of the trapping process. 72
5.2 Phase space plots (initial (top left) and final (top right)) and profiles of the projection on the horizontal coordinate (initial (bottom left) and final (bottom right)) of a typical simulation where the Multi-Turn Extraction (MTE) beam splitting is performed. The initial beam distribution is uniform in the horizontal and vertical planes. 73

6.1 Comparison between the results obtained from the two computation methods using a Gaussian distribution for a particular choice of the number of turns and of κ for different emittances. Results from the islands boxes are in purple and those from the core box are in brown. 76
6.2 Trapping fraction of a Gaussian beam distribution for different values of the number of turns and values κ. The points represent the simulated results. 77
6.3 Zoom of the trapping fraction for small emittances and comparison of the different fits. 79
6.4 Comparison of the fits from equation 6.2 (purple) and 6.3 (green). 80
6.5 Purple is the global fit from equation 6.3, pink is a polynomial fit of the first points and green is a fit from equation 6.3 but excluding the points concerned by the polynomial fit. 81
6.6 Trapping fraction for different values of the initial emittances for a Gaussian distribution (purple) and for a uniform distribution (orange). 81
6.7 Tune variation for simulations with different number of turns. 82
6.8 The plots show the results obtained for different number of turns, scanning over the values of κ. The trapping fraction systematically increase with the number of turns. 83
6.9 Gain in the trapping fraction using a tune curve where the slope is equal to zero at the resonance crossing (for two values of κ). 84
6.10 Results obtained for five different values of κ. The number of turns is different for each plots, we also compare Gaussian and uniform distributions. 85
6.11 Phase space topology of the generalized Hénon mapping obtained with GIOTTO [**?**]. 86
6.12 Trapping fraction for different variations of κ during the process. 87
6.13 Comparison between the global fit of equation 6.4 and the individual fit for different values of κ and the number of turns. 88
6.14 Zero of the trapping as a function of the number of turns and exponential fit. The figure also displays the asymptote of the exponential fit. Three values of κ are compared 89
6.15 Emittance ratio for the core and one island for different values of the number of turns and κ. The trapping fraction is also shown. 91
6.16 Histograms of the final beam distributions obtained for two different values of κ. . 92

6.17 Emittance ratios comparing a polynomial tune curve with a linear tune curve. . . 93
6.18 25000 turns, variation $\kappa = -1.1 \rightarrow -1.9$. 94

7.1 Trapping fraction (large dots and fits) and losses (small dots) for different values of κ and number of turns (Gaussian initial beam distribution). 98
7.2 Horizontal emittance ratios of the core and of the islands. 99
7.3 Vertical beam emittance as a function of the initial horizontal beam emittance. The plots compare the results obtained for different values of the initial vertical beam emittance (for different couples of the number of turns and value of κ). 101
7.4 Split beam obtained with a double resonance crossing. We observe the islands in the physical space (bottom right histogram). 102

Acronyms and abbreviations

AVF Azimuthally Varying Field

CERN European Organization for Nuclear Research

CNGS CERN Neutrino to Gran Sasso experiment

CT Continuous Transfer

CTF3 CLIC Test Facility 3

LEIR Low Energy Ion Ring

LHC Large Hadron Collider

LINAC Linear Accelerator

MAD Methodological Accelerator Design

MAD-X Methodological Accelerator Design (version X)

MTE Multi-Turn Extraction

PS Proton Synchrotron

PSB Proton Synchrotron Booster

PTC Polymorphic Tracking Code

RF-LINAC Radio-Frequency Linear Accelerator

SPS Super Proton Synchrotron

Forewords

This work has been done at CERN and at the Université Libre de Bruxelles.

I indeed had the opportunity to work at CERN in the ABP (Accelerator and Beam Physics) group of the BE (Beams) department under the supervision of Massimo Giovannozzi.

The work done during that stay at CERN eventually served as the core of the master's thesis here presented in view of the obtention of the master's degree in Engineering (Engineering Physics – Applied physics) at the Université Libre de Bruxelles.

Acknowledgments

First and foremost, I express my sincerest gratitude to my supervisor Massimo Giovannozzi, who supported me during my work with infinite patience and immense knowledge whilst also allowing me to explore my own ideas. I simply could not have wished for a better or friendlier supervisor. His door has never been shut and he has always welcomed discussion about my work, or my numerous questions about CERN accelerators, all of which have been very fruitful for my progression.

I also would like to thank Django Manglunki, with who I first discovered my passion for accelerator physics. During the months I spent at CERN, Django allowed me to discover many operational aspects of the CERN accelerators: it greatly contributed to my understanding of my work. I also thank him for all his explanations and for his patience in the control room.

It is also a pleasure for me to thank Alain Dubus for his constant and friendly support during my studies in Brussels and during this work. He has been a great help for me and I want to thank him for the frequent discussion we had about physics.

I am the most thankful to Simone Gilardoni for its support and for the motivation he inspired me; especially while he showed me the experimental aspects of MTE.

I am very thankful to Philip Bryant who allowed me to better understand beam dynamics and for the numerous discussions we had about the past and present CERN accelerators.

I would like to thank my friends and colleagues who helped me and encouraged me during my work. In particular I am very thankful to Philippe who helped me and encouraged me during my work but also during the exceptional months I spent in Geneva with him.

I am most grateful to Nicolo for his support and for the happy collaboration we had. It has been an immense pleasure and privilege to work with him these countless days, hours and nights. Apart from being an excellent colleague, Nicolo also greatly contributed to my daily routine; our “pauses café” being a real pleasure but also a great opportunity to discuss our works.

I am very grateful to Axelle for her continuous encouragement and for her patience during the months I spent in Geneva. Her help and support notably contributed to my motivation while working at CERN, *merci* ! Finally, I thank my parents and grandparents for supporting me throughout all my studies and whitout who this final work would not have been possible.

CHAPTER 1

Introduction

Nonlinear dynamics has become a very intense research field in accelerator physics and it is also the subject of intense efforts in theoretical classical mechanics. Although the linear theory of beam dynamics is well established, nonlinearities, although being now completely integrated in the design and analysis of the machines, induce many key complications that have yet to be fully understood and studied.

These nonlinear features are intimately present in all modern machines and one can cite examples ranging from high-energy collider machines (such as the nonlinear beam-beam effects in the Large Hadron Collider (LHC)) to circular accelerators (*e.g.* the coupling impedance of the accelerator components or the dynamical aperture reduction induced by nonlinear magnetic fields) and even in Linear Accelerators (LINACs) (for example the nonlinear space charge). Although these nonlinear effects are often viewed as undesired problems that have to be cured, they also suggest innovative beam manipulations such as the extraction method discussed in this work.

In view of the upgrade in beam intensity for high intensity beams in the Proton Synchrotron (PS), in particular those for the CERN Neutrino to Gran Sasso experiment (CNGS), studies have been made to reduce the losses occurring at the extraction of the CERN Proton Synchrotron (PS) during the transfer of the CNGS beam between the PS and the Super Proton Synchrotron (SPS). This leads to the design of a new extraction method based on nonlinear beam manipulation: the MTE method. An important feature of the CNGS beam extraction is the need to fill the SPS in two PS batches so as to reduce the duration of the process. The newly implemented extraction method allows to extract the beam from the PS in five consecutive turns thus allowing to fill a larger circumference of the SPS machine. This five-turn extraction is based on a nonlinear splitting of the beam: using dedicated nonlinear magnets (sextupoles and octupoles) and varying the tune in order to cross a resonance, the initial beam is split in five different parts: four islands separated from a central core.

This work is dedicated to the analytical and numerical study of selected aspects of the Multi-Turn Extraction (MTE) in order to provide a better understanding of the underlying nonlinear beam dynamics. To do so, our work is divided in two main parts: the analytical part, in which the normal form approach is used to analyze a simple model of the dynamics, and the

numerical part, that relies on the use of a tracking code to perform numerical simulations of the splitting process.

The normal form approach used in this work allows transforming the mapping describing nonlinear dynamics in the machine in presence of sextupolar and octupolar fields in another mapping exhibiting clearly the symmetries of the problem. From this mapping we extracted an Hamiltonian that we analyze to provide theoretical insight about dynamical quantities that characterize the MTE method. We were also able to introduce the concepts required for a novel approach to provide an analytical model of the trapping probability. Nevertheless no definitive results have been found following that approach. We show that this is linked to peculiarities of the resonance chosen in the actual MTE method (the fourth order resonance).

The problem can also be studied from a numerical point of view. It is possible to simulate the trapping process occurring when the particles are captured using a tracking code. We developed such a tool and we performed a large simulation campaign using both a two-dimensional model and a four-dimensional one. These simulations allow obtaining two quantities that are crucial in the optimization of the method: the fraction of particles that are trapped in the islands and the emittances of each beamlets at the end of the process. We then analyze these quantities and their dependence on the parameters of the method.

In chapter 2 we first introduce briefly some concepts about synchrotron accelerators and then we move on to a description of a few theoretical aspects of beam dynamics relevant to our work. In particular we derive step by step the Hamiltonian formalism of the transverse single particle dynamics in order to establish firm bases for the theoretical foundations of the nonlinear manipulations used in our studies. In chapter 3 we introduce the extraction method motivating our work, MTE extraction, and we construct a model for its dynamics. This dynamics is then studied in chapter 4 using a normal forms analysis. Next, we introduce the concepts needed for our numerical studies and we present the numerical tracking code that we shall use in chapter 5. We then discuss extensively the numerical simulation campaigns that we performed, in 2D in chapter 6 and in 4D in chapter 7. In particular, our main numerical results for the 2D simulations are discussed in sections 6.2, on the parametric dependence of the trapping probability, and 6.5, on the impact of the nonlinear beam splitting on the emittance. Regarding the 4D simulations, we discuss, as a function of the vertical beam emittance, the trapping fraction in section 7.2 and the emittance sharing in section 7.3. The vertical emittance blow-up is also analyzed in section 7.4. Finally we conclude in chapter 8.

CHAPTER 2

Single particle dynamics in a synchrotron

This chapter introduces the major concepts used to understand the developments of this work: notions about synchrotrons, the idea of "closed-orbit" in a circular machine, and the single particle dynamics associated with this orbit, in particular the transverse motion. We derive the main equations of this dynamics using two different methods in section 2.2 and we discuss their solutions in the linear case in section 2.3.3. Next in section 2.3 we introduce a core concept of this work: the transfer map formalism applied to the transverse dynamics.

2.1 Overview of synchrotron machines . . . 4
2.1.1 Historical introduction to particle accelerators physics . . . 4
2.1.2 Highlights about synchrotrons . . . 6
2.2 Transverse dynamics . . . 10
2.2.1 Reference frame . . . 10
2.2.2 Intuitive derivation of Hill's equation . . . 12
2.2.3 Betatron dynamics in the Hamiltonian formalism . . . 14
2.3 Transverse motion in the transfer maps formalism . . . 22
2.3.1 Symplectic matrices and maps . . . 23
2.3.2 Poincaré map and orbit tracking . . . 24
2.3.3 Linear transfer maps and linear normal forms . . . 25
2.3.4 Nonlinear transfer maps . . . 30

2.1 Overview of synchrotron machines

2.1.1 Historical introduction to particle accelerators physics

> Instead of an attic with a few test tubes, bits of wire and odds and ends, the attack on the atomic nucleus has required the development and construction of great instruments on an engineering scale.
>
> Ernest Lawrence (1901 - 1958)

The goal of this section is not to describe in a comprehensive way the history of particle accelerators from its beginning to the modern synchrotrons, nor to present in details the various types and components of a synchrotron. However it is interesting to give the reader a concise description of the machine that is at the heart of the developments presented in this work. Indeed, as the MTE extraction has been first proposed and applied to the CERN PS synchrotron, one of the oldest machines still in operation [1] and the first of its kind, we first recall some important historical steps in the development of accelerator physics related to the PS design.

The history of particle accelerators, although quite young [2], is very rich and comprises many different kind of accelerators. A complete historical treatment can be found in [14–17]. The first accelerators were electrostatic and could lead only to energies limited by the maximum achievable voltage in the device. In 1924, Ising was the first to suggest a method to overcome this difficulty [16] and this allowed Wideröe to build the first "proof-of-principle" LINAC in 1928 [16]. The main idea underlying these new machines is known as "resonant acceleration". Indeed with an electrostatic machine it is impossible to reuse the accelerating gap due to the fact that an electrostatic field is conservative. To accelerate the particles many times through the same gap therefore requires time varying fields. Mathematically this is expressed as $\boldsymbol{E} = -\nabla\Phi - \frac{\partial}{\partial t}\boldsymbol{A}$ where $\boldsymbol{B} = \nabla \times \boldsymbol{A}$. In that expression, Φ is the electrostatic potential leading to a conservative electric field, thus unable to accelerate the particle through repeated application. The non-conservative field comes from the vector potential $\boldsymbol{A}$ if it is time varying. This electric field is time varying in a periodic manner (usually sinusoidal and considered as such in the following discussion) and will accelerate the particle every time it goes through a gap where this field is applied. This is the idea of the first LINAC as depicted in figure 2.1.

The key point of the resonant acceleration is to have the particle to see the field at the same phase every time it traverses a gap thus providing a time average non zero acceleration. In LINACs this is achieved by tuning the drift lengths between the gaps as shown in figure 2.1.

A few years later, in 1929, Lawrence used the same idea of resonant acceleration but in a way that makes the machine circular. This is the principle of the cyclotron [17]. In a cyclotron the particles are "transported" to the next gap using a magnetic field to bend their trajectory into a spiral bringing them back to the same accelerating gap. In order to reach higher energies with a cyclotron one has to overcome difficulties related to relativistic effects. Although it is possible to modify the original concept to obtain either synchro-cyclotrons or isochronous (or Azimuthally Varying Field (AVF)) cyclotrons, with these machines, multi-GeV energies are still

[1] The PS indeed turned fifty at the end of 2009.

[2] The first step in this field is usually quoted as the Rutherford's experiment with α nuclei in 1911 [14].

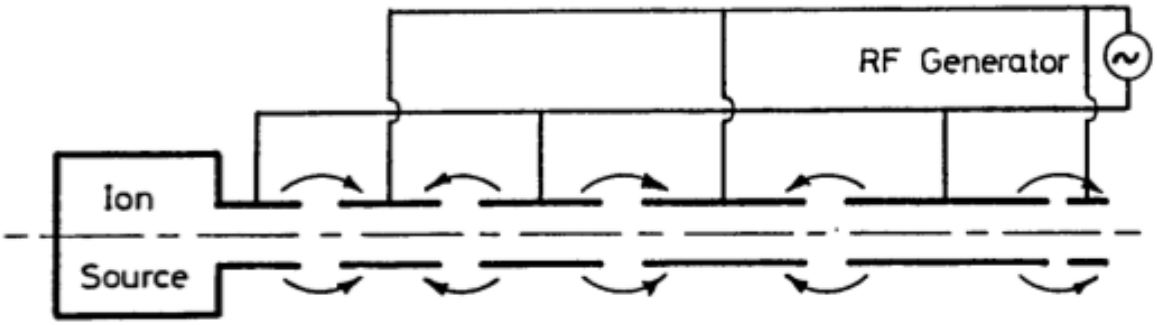

Figure 2.1: Schematics of the "Wideroe Linac", the ancestor of modern RF-LINACs, using the principle of resonant acceleration (from Ref. [1]).

not in reach due to technological constraints. Therefore a new idea was required: the concept of "synchrotron" that we shall now describe in more details.

In 1944 McMillan and Veksler discovered the principle of "phase stability" and invented the synchrotron [17]. In a synchrotron the trajectory of the particle is kept as a constant closed orbit using a magnetized path for the beam; the particle thus traverses the accelerating gaps once every turn. The phase stability principle allows to focus the beam in the longitudinal direction so that particles with momentum errors are not lost while the beam accelerates as a whole over a very high number of turns [3]. Quickly different synchrotron machines were built, including in 1946 the first synchrotron of Goward and Barnes, an electron machine built from a converted betatron magnet [16]. This first machine has been followed by proton machines as initially proposed by Oliphant, Gooden and Hyde in 1947. The first operating proton synchrotron was the Cosmotron at Brookhaven National Laboratory in 1952. As we shall discuss below, these first machines were "weak focusing" synchrotrons (also known as constant-gradient synchrotrons) and were inherently limited in energy at around 10 GeV by the size of the required magnetic system. The invention of the "strong focusing", or alternating gradient focusing, by Christophilos, Courant, Livingston and Snyder in 1952 opened the way for machines operating at much higher energies. This principle allows to focus the beam to a smaller size thus decreasing the magnet aperture needed to accommodate the beam pipe [15]. This is directly similar to the fact that in geometrical optics a pair of focusing and defocussing lenses can be globally focusing.

At that time, the newly created CERN team had just designed the first CERN synchrotron machine as a weak focusing machine. It had already been approved for construction, but under the impetus of O. Dahl, the project leader, it was abandoned in favor of a 25 GeV/c alternating gradient machine, what became the Proton Synchrotron (PS) [17]. Summarizing, three main different concepts were required to made the construction of the PS possible: the resonant acceleration, the phase stability and the strong focusing [4].

Nowadays the main distinction that can be made to classify accelerators is between the

[3] Indeed a particle spend a much longer time in a synchrotron than in a cyclotron (and thus will do a higher number of turns) so the longitudinal stability is a major issue

[4] To be complete we should add that the strong focusing concepts has an important consequence on the phase stability, *i.e.* the transition crossing which was feared and had to be understood during the design of the first strong focusing machines and proved possible during the commissioning of the PS, see for example [18].

LINACs and the circular accelerators. The linear accelerators comprise the continuous tension accelerators, the induction linear accelerators, and the Radio-Frequency Linear Accelerators (RF-LINACs). Only the RF-LINACs are of importance for high energy accelerators and are usually used as the first element of an acceleration chain (see section 3.1). The circular accelerators family mainly contains the cyclotron and the synchrotron [5]. In this work we shall consider only synchrotron machines, which we describe in more details in the next section.

2.1.2 Highlights about synchrotrons

The main idea behind a circular accelerator is then to have a magnetic field, perpendicular to the plane of the orbit, guiding the particle and an electric field, parallel to the direction of motion of the particle, to provide acceleration.

The motion of a single charged particle in an electromagnetic field is governed by the Lorentz force:

$$\boldsymbol{F} = q\left(\boldsymbol{E} + \boldsymbol{v} \times \boldsymbol{B}\right) , \tag{2.1}$$

where q is the charge of the particle, $\boldsymbol{v}$ is its velocity and $\boldsymbol{E}$ and $\boldsymbol{B}$ are the electric and the magnetic field respectively. In this work we shall always consider that these fields are externally imposed to the particles, *e.g.* by magnets and RF cavities. Thus we do not consider the effects of the beam itself *i.e.* space charge and wake fields. This is a simplifying approximation but in any case, the treatment of beam dynamics is always divided in the so-called "single particle dynamics" and in "collective effects" where the collective effects are viewed as perturbing the design of the machine.

The magnetic field can only bend the particle trajectory, and in the majority of cases, electric field is only used to accelerate longitudinally the particle, not to deflect it [6]. If we consider only a planar case where the magnetic field is perpendicular to the direction of motion, the particle will follow a trajectory that is instantaneously a circle. From equation (2.1) and equating the force with the centripetal component to obtain the relation between the momentum of the particle and the radius of that circle, we have (see section 2.2.1 for more detail):

$$p = qB\rho\,, \tag{2.2}$$

where p is the momentum of the particle, B is the magnetic field and ρ is the local radius of curvature of the trajectory. The quantity $B\rho$ is known as the magnetic rigidity of the particle; it is the property of the beam at a given momentum or energy. Another derived well known relation is the one giving the cyclotron frequency, *i.e.* $\nu = \frac{\omega}{2\pi} = \frac{qB}{2\pi m}$.

Thus if we have a spatially constant magnetic field not varying with time, the increase of momentum will lead to an increasing radius and the orbit will be a spiral: this is the basic idea behind a cyclotron .

This requires a magnetic field filling a large volume [15]: the maximal momentum will dictate the largest radius. Thus to reach a high energy one would need a very large magnetized volume. The cost of such a magnet would increase very rapidly, not to mention the difficulties to build it. Therefore to reach higher energies and to limit this volume the solution is to force

[5] In addition to the betatron which gave its name to the "betatronic motion" (see section 2.2), invented by Wideröe in 1923 and reinvented by Kerst in 1940, but now mainly of historical importance, the microtron and some variations of these types [14, 15, 17].

[6] Notable exceptions, being the electrostatic deflectors of very low energy machines and the so-called "crab-cavities" [19].

the particle to follow a closed orbit, *i.e.* an almost circular orbit [7]. Then in equation (2.2) ρ is constant and one can conclude that a magnetic field varying with time, synchronized with the momentum of the beam is needed. The synchrotron is thus a machine where the design is such that particles should follow a defined orbit which is constant with time (we shall make this statement more explicit in section 2.1.2). The first step in the design of a machine is to define such an orbit.

Now that we have the main elements to discuss the particle dynamics in a synchrotron we should not postpone a discussion of the concepts of reference particle, design orbit and real particle's orbit and motion.

Figure 2.2 shows the LEIR machine at CERN and allows to have an overview of a complete machine. The elements discussed in the next sections are shown: the beam pipe, bending magnets, quadrupole magnets, and the RF-cavities.

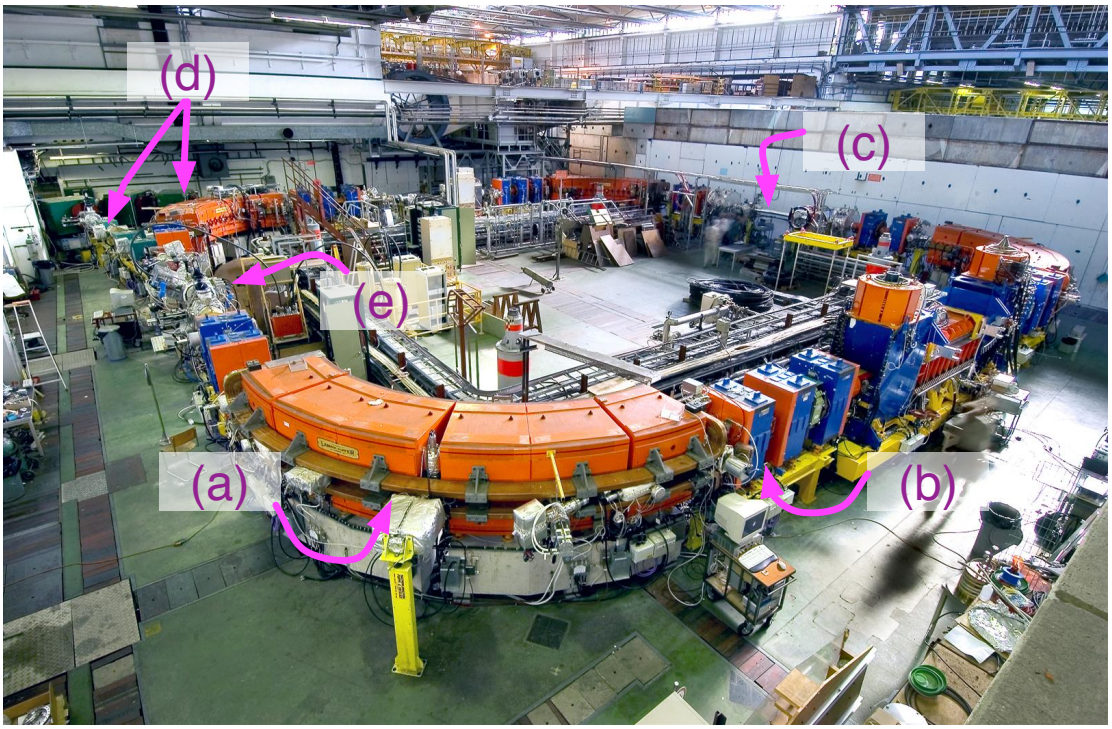

Figure 2.2: The LEIR synchrotron at CERN [2]. (a) Dipolar bending magnet (b) Quadrupoles (c) Beam pipe (d) Injection and extraction lines (e) RF-cavities.

Design orbit and reference particle

The *design orbit* is the orbit defined in such a way that it goes in the middle of the magnets.

We should also make a distinction between the so-called *closed orbit* and the design orbit. The orbit considered to be the perfect orbit at some point of the operation of the machine is

[7] Note that the reduction of the magnetized volume is recurring in the design of particle accelerators. As described in sections 2.1.1 and 2.3.3 this also subdivide the family of synchrotrons between weak and strong focusing machines. In addition, in the design of a high energy accelerator such as the LHC this problem is crucial in the design of the orbit.

called the closed-orbit or reference orbit. Ideally this is just the design orbit but the closed-orbit can differ from the design orbit during the operation of the machine. For example prior to extraction or injection a bump is made to the orbit and the closed-orbit is thus modified. In addition due to various errors (misalignment, field errors, fringe fields, etc.) the closed-orbit usually exhibits uncontrolled deviation from the design orbit that should be corrected [1, 20].

The *reference particle* is the particle that at each instant as a momentum equal to the design momentum for the given magnetic field at that instant and following the closed-orbit defined by the magnetic configuration of the machine. As we shall discuss later, in the machine the real particles oscillate around the trajectory of the reference particle and the solution to the dynamics is thus split in three parts: the definition of the design orbit defined by the features of the dipole magnets, the characterization of the closed-orbit with respect to the design-orbit, depending *e.g.* on energy-offset and corrector magnets, and the motion of the particles around the hypothetic reference particle whose motion follows the closed-orbit.

Key components for the dynamics of a synchrotron

The particles move in a beam pipe under vacuum; it allows the beam to follow the design orbit. A good vacuum is needed to reduce particle-matter interactions, hence improving emittance preservation and beam lifetime. A magnetic field guides the particles along this design orbit where it is not straight. Dipolar magnets surrounding the beam pipe provide this magnetic field. The design orbit can be decomposed in straight sections and arc sections where the dipolar field has to be matched to the curvature of the arc.

Dipole magnets produce a spatially constant field in the vicinity of the beam orbit, perpendicular to the plane of the orbit for the main dipoles defining the design trajectory. Indeed, this field, following equation (2.1) will bend the trajectory. The succession of these dipole magnets will therefore define the design orbit of the beam. From Lorentz equation (2.1) we can obtain the bending angle of a dipole starting in s_1 and ending in s_2:

$$\theta = \frac{q}{p}\int_{s1}^{s2} \boldsymbol{B}\cdot\boldsymbol{dl} = \frac{1}{B\rho}\int_{s1}^{s2} \boldsymbol{B}\cdot\boldsymbol{dl}\,, \tag{2.3}$$

where we used equation (2.2) to introduce the magnetic rigidity.

Of course the total bending over one turn should be 2π and therefore we have

$$\oint \boldsymbol{B}\cdot\boldsymbol{dl} = 2\pi B\rho\,, \tag{2.4}$$

and finally we obtain the needed total length of dipoles

$$L = \frac{2\pi B\rho}{B_{dipoles}}\,, \tag{2.5}$$

where $B_{dipoles}$ is the magnetic field inside the dipoles.

However this would in principle allow the particles to follow the design orbit, the imperfections of the magnets will induce errors and the orbit has to be corrected. This is done with small dipole magnets called dipole correctors. Other types of dipole magnet are also needed for injection and extraction: slow and fast kicker magnets used to modify the closed-orbit and septum magnets (see section 3.2). All these dipole magnets lead to a closed-orbit different from the design one.

In addition, other kinds of magnets modify the trajectory of particles exhibiting deviation from the closed-orbit. The magnets [8] are thus of different types, serving different functions:

Quadrupole magnets Quadrupole magnets are magnets whose field increases linearly with respect to the distance from the center. They serve as focusing and defocusing elements and under some conditions they allow the particles beam to remain focused around the trajectory of the reference particle [9]. Dipoles and quadrupoles define the so-called "linear optics" of the machine. Figure 2.3 schematically shows the magnetic field of a quadrupole: the field is zero at the center and in each directions it increases linearly with the distance from the origin.

Sextupoles and octupoles These magnets are non linear elements introduced to correct beam properties [10] or to introduce a desired non linear component in the dynamics. For example the key elements of the MTE is a combination of sextupoles and octupoles as we shall discuss later in this work.

Higher order magnets These magnets, mainly decapoles and dodecapoles, are used only in very few cases (an important one being the LHC) to correct for the undesired effects of the sextupoles and octupoles on the dynamical aperture. We shall not consider these here.

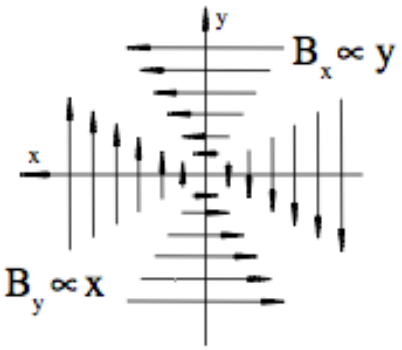

Figure 2.3: Schematics of the magnetic field of a quadrupole (from Ref. [3]).

Regarding beam injection or extraction, we also have to consider *septum magnets*, a special type of dipole magnet. These magnets comprise two different regions, one where no field is present and another one where a dipolar field is present. They are used during injection or extraction to leave the circulating beam unperturbed while at the same time deflecting the injected or extracted beam.

In addition to these magnets deflecting the particles trajectories, RF cavities are used to provide the accelerating electric field. As the methods discussed in this work do not involve energy changes, we shall not describe these elements here, see for example [21], [14] or [3].

[8] We do the usual approximation that consists of neglecting any fringe fields. In that case the magnetic fields are purely 2D transversal fields.

[9] Dipoles also act as weak focusing elements in the horizontal plane.

[10] For example, sextupoles are used to correct the chromaticity.

2.2 Transverse dynamics

In this section we derive and discuss the equations governing the transverse dynamics of a single particle in a synchrotron. As discussed in the previous section the magnetic fields show their effects on the transverse motion, also called betatron motion, of the particles and the equations derived bellow form a complete model for this motion.

In addition to the transverse motion, particles can lead or lag around the reference particle and have an momentum deviation compared to the reference particle (and possibly, all particles can have a momentum offset). We shall not consider these off-momentum effects here and we completely decouple the transverse motion from the longitudinal motion. Therefore these derivations lead to special cases of a more general theory including these off-momentum effects. Latter on we will introduce the first order manifestation of this effects, the so-called dispersion and chromaticity, and we will show how a basic model can be constructed to couple the longitudinal and the transverse motion.

This dynamics can be described starting from Newton's equation or from the Lagrangian or Hamiltonian formalisms. Although it is useful to start from Newton's equations to gain a more physical understanding of the properties of the motion, a more detailed analysis, especially one including non linear effects take huge benefits from the Hamiltonian formalism. Therefore we shall first provide an intuitive derivation of equations of the transverse motion (Hill's equation) in section 2.2.2 to characterize globally the dynamics and introduce some important concepts, and then in section 2.2.3 we shall derive the Hill's equation using the Hamiltonian formalism which shall provide, in addition to these equations, more tools to analyze the transverse dynamics.

2.2.1 Reference frame

For the treatment of the dynamics in a circular machine whose design orbit has been defined, we consider a curvilinear coordinate system. This reference frame is based on the trajectory of the reference particle [22]. The origin of the coordinates thus follow the reference trajectory that is a curve in space composed of straight and bent parts.

The s variable is the independent coordinate and the vector $\boldsymbol{r}_0(s)$ defines the reference trajectory. We make the assumption that the reference trajectory lie in a plane (referred to as the horizontal plane), *i.e.* the accelerator is flat, without torsion. The curvature is noted $h(s) = \frac{1}{\rho_0(s)}$ where ρ_0 is the local radius of curvature of the reference trajectory.

The successive location of the reference particle thus defines $\boldsymbol{r}_0(s)$ and the time dependence of the motion defines the *schedule* $t_0(s)$ along the path [22]. Doing so we directly consider s to be the independent variable, as it is usually the case for the treatment of accelerator dynamics.

The particle dynamics, *i.e.* $\boldsymbol{r}(s)$ shall be described with respect to the reference trajectory, *i.e.* the motion *in space* is not considered, only the motion with respect to the reference particle. It is also assumed that the lattice design of the accelerator allows the particles to follow a trajectory close to the reference trajectory. The curvilinear coordinate system used to describe this motion is constructed with its longitudinal axis (the s axis) being locally tangent to the reference trajectory. The two other axis (usually called x and y axis) are perpendicular to that axis and form a right-handed orthogonal set. The x-axis is chosen to lie in the horizontal plane, the y-axis thus being the vertical plane. This coordinate system is the Frenet-Serret reference frame.

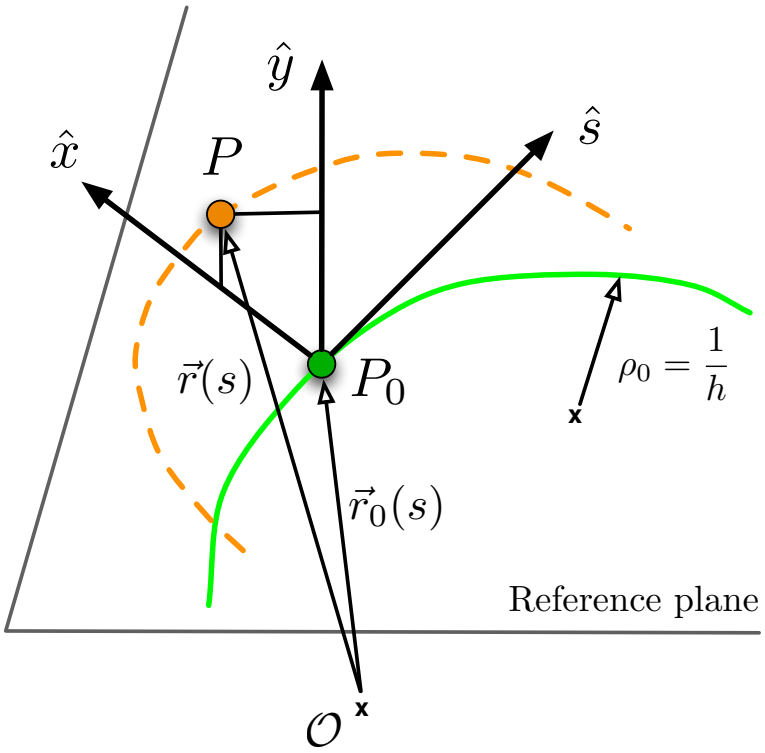

Figure 2.4: Curvilinear coordinates system based on the reference trajectory. The origin of the $\boldsymbol{r}$-coordinate is arbitrary in the laboratory frame.

The longitudinal coordinate of the real particle (whose position is $\boldsymbol{r}(s)$) is obtained by the orthogonal projection on the reference trajectory. Thus, at a given time, the s coordinates of the real particles can be different, *e.g.* due to momentum differences or path differences. The transverse coordinate system formed by the x and y axes has its origin at that point.

The unit vectors of this coordinate system are defined as

$$\begin{cases} \hat{\boldsymbol{s}} &= \frac{d\boldsymbol{r}_0}{ds}, \\ \hat{\boldsymbol{x}} &= \hat{\boldsymbol{y}} \times \hat{\boldsymbol{s}}, \\ \hat{\boldsymbol{y}} &= \hat{\boldsymbol{s}} \times \hat{\boldsymbol{x}}, \\ \hat{\boldsymbol{s}} &= \hat{\boldsymbol{x}} \times \hat{\boldsymbol{y}}. \end{cases} \tag{2.6}$$

The position vector of a particle is thus given by

$$\boldsymbol{r} = \boldsymbol{r}_0(s) + x(s)\hat{\boldsymbol{x}}(s) + y(s)\hat{\boldsymbol{y}}(s). \tag{2.7}$$

The vectors $\boldsymbol{r}_0(s)$, $\hat{\boldsymbol{x}}(s)$ and $\hat{\boldsymbol{y}}(s)$ are given by design and solving the dynamics implies the determination of $x(s)$, $y(s)$ and $t(s)$. These three unknown correspond to the three degrees of freedom of the dynamics of the particle in the accelerator: the transverse motion (xy plane) and the longitudinal motion, *i.e.* the motion around the reference particle in the s direction. In addition, it is usually possible to decouple the transverse motion from the longitudinal motion.

This coordinate system is local and follows the motion of the reference particle. Therefore the s-derivatives of the unit vectors have to be considered. This is the usual case of a Frenet-

Serret system with no torsion:

$$\frac{d\hat{\boldsymbol{x}}}{ds} = h(s)\hat{\boldsymbol{s}} \tag{2.8}$$

$$\frac{d\hat{\boldsymbol{y}}}{ds} = 0 \tag{2.9}$$

$$\frac{d\hat{\boldsymbol{s}}}{ds} = -h(s)\hat{\boldsymbol{x}} \tag{2.10}$$

In this work we mostly neglect the longitudinal dynamics; we consider that the particles have the reference momentum [11].

2.2.2 Intuitive derivation of Hill's equation

Here we derive the Hill's equations, *i.e.* the differential equation governing the transverse dynamics starting from Newton's equation. This approach is less "powerful" in many cases than the Hamiltonian approach, because it gives only the equations of motion and can't be easily used when one considers also nonlinearities. However in the plain linear case it gives a more intuitive feeling of the physical principles governing the transverse betatron motion. Therefore we derive them here in a particular case given by the following hypothesis (in addition to the ones already mentioned):

- In the median plane, the magnetic field is perpendicular to the horizontal plane at every location in the machine and the longitudinal magnetic field is zero everywhere: we exclude solenoidal fields and we consider a case without coupling between the horizontal and the vertical motions;
- We consider only a case with linear fields, or equivalently we consider the betatron oscillations only at the first order (small displacements with respect to the reference particle);
- The energy of the machine is constant or varies much slower than the period of the betatron oscillations [12]; in addition, the longitudinal motion is completely neglected;
- The amplitude of the oscillations is small compared to the wavelength of these oscillations and thus we have $p \approx p_s$ and $p_x, p_y << p_s$ where $\boldsymbol{p} = (p_x, p_y, p_s)$.

We start from the Lorentz equation (2.1) for $\boldsymbol{E} = 0$:

$$\frac{d\boldsymbol{p}}{dt} = q\boldsymbol{v} \times \boldsymbol{B}\,, \tag{2.11}$$

where $\boldsymbol{p}$ is expressed in the coordinates detailed in figure 2.4. The time derivative of the momentum in the Frenet-Serret coordinates is

$$\frac{d\boldsymbol{p}}{dt} = p_x\frac{d\boldsymbol{x}}{dt} + p_s\frac{d\boldsymbol{s}}{dt} + \frac{dp_x}{dt}\boldsymbol{x} + \frac{dp_y}{dt}\boldsymbol{y}\,, \tag{2.12}$$

[11] The reference momentum at a given time is the momentum of the reference particle allowing it to follow the reference orbit. The field strength of the bending magnets is adapted to this momentum according to equation (2.2).

[12] This hypothesis does not exclude the case of particles with momentum deviation from the reference particle.

taking into account that $\frac{dp_s}{dt} = 0$ because there is no momentum change. The derivation of the unit vectors in the Frenet-Serret coordinates, *i.e.* $\frac{d\hat{\boldsymbol{x}}}{dt} = \frac{d\hat{\boldsymbol{x}}}{ds}\frac{ds}{dt} = \frac{v}{\rho(s)}\hat{\boldsymbol{s}}$ and $\frac{d\hat{\boldsymbol{s}}}{dt} = \frac{d\hat{\boldsymbol{s}}}{ds}\frac{ds}{dt} = -\frac{v}{\rho(s)}\hat{\boldsymbol{x}}$ gives

$$\begin{aligned}\frac{d\boldsymbol{p}}{dt} &= p_x\frac{d\hat{\boldsymbol{x}}}{dt} + \frac{dp_x}{dt}\hat{\boldsymbol{x}} + \frac{dp_y}{dt}\hat{\boldsymbol{y}} + p_s\frac{d\hat{\boldsymbol{s}}}{dt} \\ &= \left(\frac{dp_x}{dt} - \frac{p_s v}{\rho}\right)\hat{\boldsymbol{x}} + \frac{dp_y}{dt}\hat{\boldsymbol{y}} + (\cdots)\hat{\boldsymbol{s}};\end{aligned} \tag{2.13}$$

where the s component, the longitudinal motion, is neglected [13].

As we have $\frac{dp_x}{dt} = v\frac{dp_x}{ds} = mv\frac{dv}{ds} = mv^2x''$, similarly for y we can write

$$\left(mv^2x'' - m\frac{v^2}{\rho}\right)\hat{\boldsymbol{x}} + \left(mv^2y''\right)\hat{\boldsymbol{y}} + (\cdots)\,\hat{\boldsymbol{s}} = q\boldsymbol{v}\times\boldsymbol{B}, \tag{2.14}$$

using the approximation $v \approx v_s$.

As we consider only linear fields, *i.e.* dipolar and quadrupolar fields, and no longitudinal fields, we have

$$B_x = B_{x;0} + B_{x;x}x + B_{x;y}y \tag{2.15}$$
$$B_y = B_{y;0} + B_{y;x}x + B_{y;y}y. \tag{2.16}$$

Considering that the B_x field is zero in the median plane, we have to set $B_{x;0}$ and $B_{x;x}$ to zero. As $\operatorname{div}\boldsymbol{B} = 0$ and $\operatorname{curl}\boldsymbol{B} = 0$ we also have the conditions $B_{x;y} = B_{y;x}$ and $B_{y;y} = 0$. We finally have

$$B_x = B_{x;y}y \tag{2.17}$$
$$B_y = B_{y;0} + B_{y;x}x, \tag{2.18}$$

where $B_{y;0} = B_0$ the dipolar guiding field defining the design orbit which is matched to the correct momentum and curvature *via* equation (2.2).

With the hypothesis considered above we can set $\rho \simeq \rho_0 + x \Rightarrow \frac{1}{\rho} \simeq \frac{1}{\rho_0}\left(1 - \frac{x}{\rho_0}\right)$ and $p = p_0 + \Delta p \Rightarrow \frac{p_0}{p} = 1 - \frac{\Delta p}{p_0}$, considering that a real particle can have a small constant momentum error compared to the reference particle.

We finally obtain the Hill's equations:

$$\begin{cases} x'' + \left(\frac{1}{\rho_0^2} + \frac{B_{x;y}}{B_0\rho_0}\right)x &= \frac{1}{\rho_0}\frac{\Delta p}{p_0} \\ y'' - \frac{B_{x;y}}{B_0\rho_0}y &= 0. \end{cases} \tag{2.19}$$

The right-hand side of the horizontal equation is a driving term present if the particle has a momentum offset with respect to the reference particle. This term forces the particle to follow what is called the *dispersive* orbit. Although this is an important aspect of the general theory, in this work we shall consider that all the particles in the beam have the reference energy and we shall neglect this term.

These equations are written in their general form [14] as

$$\begin{cases} x'' + K_x(s)x &= 0 \\ y'' + K_y(s)y &= 0, \end{cases} \tag{2.20}$$

[13] Differentiation with respect to s is denoted as $'$ while time differentiation are explicitly written.

[14] Neglecting the in-homogenous term.

where $K_x(s) = \frac{1}{\rho^2} - \frac{B_{x;y}}{B_0\rho_0}$ and $K_y(s) = +\frac{B_{x;y}}{B_0\rho_0}$. Equations of this form where the functions $K_{x,y}(s)$ are periodic (as it is the case in a circular accelerator) are called Hill's equations [14, 15].

These equation have the form of an oscillator with a longitudinal dependence on the focusing $K(s)$ functions. A few comments can be discussed:

- For the motion to be stable in one plane, the sign of $K(s)$ has to be positive. Obviously to achieve a stable beam in the machine, the oscillations have to be stable in both planes;
- The horizontal equation exhibit a focusing term $\frac{1}{\rho_0^2}$: this is the weak focusing effect of the dipoles, the deflection angle being larger if the particle enter on the outer side of the magnet and vice-versa. This effect can usually be neglected for large machines (*e.g.* the LHC), but is of more relevance for smaller machines;
- We notice that the sign of the term coming from the quadrupole gradient is opposite in x and y planes, this means that a horizontally focusing quadrupole is defocusing in the vertical plane. Nevertheless it is possible to obtain positive focusing functions $K_{x,y}(s)$ for all s due to the weak focusing term if ρ is small enough. As mentioned in the historical overview, this possibility was exploited by the weak focusing synchrotrons [14–16]: a small defocusing s-independent gradient [15] was chosen in the horizontal plane, but the horizontal motion was maintained stable by the weak focusing term, doing that the vertical motion was automatically stable. In modern strong focusing machines, the gradients are stronger but are not constant along the circumference of the machine and although locally defocusing the global motion is stable in both plane. This imply that some conditions are fulfilled, as discussed in sections 2.3.3 and 2.3;
- The motion induced by these equations is thus of the form of oscillations around the closed-orbit, these oscillations are called *betatron motion*. The oscillations are those of an oscillator with a s dependence: the amplitude and the phase advance are not constant as we shall discuss in section 2.3.3.

2.2.3 Betatron dynamics in the Hamiltonian formalism

Now that we introduced the main concept of the betatron dynamics we derive the equations of the motion in a more general way, including the nonlinear terms, from the Hamiltonian formalism.

Derivation of the Hamiltonian of the motion expressed in the Frenet-Serret coordinate system can be found in many references. However even if we do not introduce new ideas or a new point of view in this section we try to derive the betatron Hamiltonian step by step and by exposing clearly the successive approximations. In addition we try to fully justify these approximation and to highlight the subtleties that we encountered the first time we were exposed to formalism in the literature. We found interesting try to fully expose these details from the beginning, as we think it makes it easier to deal with the later developments.

[15] A purely constant gradient is not achievable due to the finite length of the magnets but the machine design was trying to make it as constant as possible.

Derivation of the general Hamiltonian

We start the description considering the usual case of classical mechanics where time is the independent variable and where the motion of a particle is described by the functions $x(t)$, $y(t)$ and $s(t)$ *via* the position vector $\boldsymbol{r} = \boldsymbol{r}_0(s(t)) + x(s(t))\boldsymbol{x} + y(s(t))\boldsymbol{y}$.

The relativistic Lagrangian of a charged particle in a electromagnetic field is expressed in term of scalar and vector potentials Φ and $\boldsymbol{A}$. The fields are derived from the potentials *via*

$$\boldsymbol{E} = -\operatorname{grad}\Phi - \frac{\partial \boldsymbol{A}}{\partial t}, \tag{2.21}$$

$$\boldsymbol{B} = \operatorname{curl}\boldsymbol{A}. \tag{2.22}$$

The Lagrangian reads [22, 23]

$$L(\boldsymbol{r}, \boldsymbol{v}, t) = -mc^2\sqrt{1-\beta^2} - q\left[\Phi(\boldsymbol{r}, t) - \boldsymbol{v}\cdot\boldsymbol{A}(\boldsymbol{r}, t)\right], \tag{2.23}$$

where β is the relativistic $\beta = \frac{v}{c}$ and $\boldsymbol{r}$ and $\boldsymbol{v}$ are the physical position and velocity.

The velocity is written

$$\boldsymbol{v} = \frac{\boldsymbol{r}}{dt} = \dot{x}\hat{\boldsymbol{x}} + \dot{y}\hat{\boldsymbol{y}} + (1+hx)\dot{s}\hat{\boldsymbol{s}} \tag{2.24}$$

due to the definition of the unit vectors (equation (2.6)) and their derivatives (equation (2.8)) and where the overhead dot is for the total differentiation with respect to time.

The vector potential is $\boldsymbol{A} = A_x\hat{\boldsymbol{x}} + A_y\hat{\boldsymbol{y}} + A_s\hat{\boldsymbol{s}}$ and the canonical momenta are given by

$$P_x = \frac{\partial L}{\partial \dot{x}} = \frac{m\dot{x}}{\sqrt{1-\beta^2}} + qA_x \tag{2.25}$$

$$P_y = \frac{\partial L}{\partial \dot{y}} = \frac{m\dot{y}}{\sqrt{1-\beta^2}} + qA_y \tag{2.26}$$

$$P_s = \frac{\partial L}{\partial \dot{s}} = \frac{m(1+hx)^2\dot{s}}{\sqrt{1-\beta^2}} + q(1+hx)A_s. \tag{2.27}$$

The other canonical coordinates, the positions are simply $Q_x = x$, $Q_y = y$ and $Q_s = s$. Our goal is to obtain the Hamiltonian of the motion written in term of the canonical variables related to the Frenet-Serret reference frame. To do this we use the classical relation

$$H = \sum_k P_k \cdot Q_k - L. \tag{2.28}$$

However, in the expression of the Lagrangian we have to replace all the generalized velocities by the canonical momenta. In addition, in the expression of the momenta, equation (2.25) the velocities appear both explicitly and hidden in the physical velocity v of the relativistic γ. To invert these relation we first write the mechanical momentum vector $\boldsymbol{p}$ as a function of the canonical momenta [22]:

$$\boldsymbol{p} = \frac{m\boldsymbol{v}}{\sqrt{1-\beta^2}} = (P_x - qA_x)\,\hat{\boldsymbol{x}} + (P_y - qA_y)\,\hat{\boldsymbol{y}} + \left(\frac{P_s}{1+hx} - qA_s\right)\hat{\boldsymbol{s}}, \tag{2.29}$$

and from the first equality we extract the usual relation [16]

$$v = \frac{+cp}{\sqrt{p^2 + m^2c^2}}. \tag{2.30}$$

[16] The sign is chosen so that a positive momentum corresponds to a positive velocity.

Finally we obtain the desired inverted relation giving the generalized velocities:

$$\dot{x} = (P_x - qA_x)\frac{c}{\sqrt{p^2 + m^2c^2}} \tag{2.31}$$

$$\dot{y} = (P_y - qA_y)\frac{c}{\sqrt{p^2 + m^2c^2}} \tag{2.32}$$

$$\dot{s} = \left(\frac{P_s}{1+hx} - qA_s\right)\frac{c}{(1+hx)\sqrt{p^2 + m^2c^2}} \tag{2.33}$$

Using these relations we can derive the Hamiltonian from equation (2.28):

$$H = c\sqrt{(P_x - qA_x)^2 + (P_y - qA_y)^2 + \left(\frac{P_s}{1+hx} - qA_s\right)^2 + m^2c^2} + q\Phi. \tag{2.34}$$

This is the main Hamiltonian at the foundation of all the beam dynamics [17].

This Hamiltonian is expressed in term of the canonical variables of the Frenet-Serret frame: the canonical coordinates are the x, y and s physical coordinates but the canonical momenta are not simply the projection of the physical momenta added to the components of the potential vector! Indeed, they are modified due to the presence of the curvature h.

This derivation is rather laborious but it allows to observe in detail the consequences of our choice of coordinates. The main point is that the Hamiltonian cannot be written in the usual form that is valid only for a Cartesian system of coordinates:

$$H = c\sqrt{(\underline{\boldsymbol{P}} - q\underline{\boldsymbol{A}})^2 + m^2c^2} + q\Phi, \tag{2.35}$$

where the underline denotes a vector in the Cartesian system. Nevertheless, we can think of our Frenet-Serret frame as a curvilinear frame embedded in the physical Cartesian space. In that case we can start from the Hamiltonian (2.35) and perform the change of coordinates using the generating function method [22–24].

To do that we use a generating function of the third kind where the old coordinates are the Cartesian coordinates (the q_k) and the corresponding canonical momenta in the Cartesian frame, *i.e.* the mechanical momenta plus the charge times the vector potential (the p_k). The new canonical variables are the coordinates in the Frenet-Serret system (Q_k) and the unknown conjugated momenta (P_k).

The generating function reads

$$F_3 = -\underline{\boldsymbol{p}} \cdot [\underline{\boldsymbol{r}}_0(s) + x\hat{\boldsymbol{x}}(s) + y\hat{\boldsymbol{y}}], \tag{2.36}$$

where $\underline{\boldsymbol{p}}$ is the old canonical momentum vector.

This generating function performs the following canonical transformation:

$$q_k = -\frac{\partial F_3}{\partial p_k} \tag{2.37}$$

$$P_k = -\frac{\partial F_3}{\partial Q_k}, \tag{2.38}$$

while the new Hamiltonian is equal to the old one (where the old coordinates are replaced by the new ones) as the transformation is time independent.

[17] At this point this Hamiltonian is still very general and is *not* limited to the transverse dynamics.

Therefore we obtain

$$\boldsymbol{r}(s) = \boldsymbol{r}_0(s) + x\hat{\boldsymbol{x}} + y\hat{\boldsymbol{y}} \tag{2.39}$$
$$P_x = \underline{\boldsymbol{p}} \cdot \hat{\boldsymbol{x}} \tag{2.40}$$
$$P_y = \underline{\boldsymbol{p}} \cdot \hat{\boldsymbol{y}} \tag{2.41}$$
$$P_s = (1 + hx)\underline{\boldsymbol{p}} \cdot \hat{\boldsymbol{s}}. \tag{2.42}$$

The first equality just gives the desired relation between the two sets of coordinates and the other three equalities give the expression of the canonical momenta conjugated to the Frenet-Serret coordinates.

Replacing these new coordinates in the Cartesian Hamiltonian (2.35) gives the same result as our derivation from the Lagrangian: we obtain the main Hamiltonian (2.34).

From this Hamiltonian we have the equations of motion:

$$\dot{x} = \frac{\partial H}{\partial P_x}, \tag{2.43}$$
$$\dot{P}_x = -\frac{\partial H}{\partial x}, \tag{2.44}$$
$$\dot{y} = \frac{\partial H}{\partial P_y}, \tag{2.45}$$
$$\dot{P}_y = -\frac{\partial H}{\partial y}, \tag{2.46}$$
$$\dot{s} = \frac{\partial H}{\partial P_s}, \tag{2.47}$$
$$\dot{P}_s = -\frac{\partial H}{\partial s}, \tag{2.48}$$

and the total time derivative of the Hamiltonian is $\dot{H} = \frac{\partial H}{\partial t}$.

As mentioned before we want to obtain a description where the independent variable is the longitudinal coordinate s instead of the time t [18], *i.e.* we want to go from $H(x, P_x, y, P_y, s, P_s; t)$ to $\mathcal{H}(x, P_x, y, P_y, t, -H)$ (because the old independent variable becomes a canonical coordinate and the momentum conjugated to the time is the energy).

To do this, we use the often repeated procedure of [22] and [14]: we use the last two equations of the motion to write the following expressions, where the prime denote the differentiation

[18] As stated in [22] this is possible because the longitudinal motion never reverse and s is thus a monotonically increasing function of t.

with respect to s:

$$x' = \frac{\dot{x}}{\dot{s}} = \frac{\left(\frac{\partial H}{\partial P_x}\right)_{P_s}}{\left(\frac{\partial H}{\partial P_s}\right)_{P_x}} = -\left(\frac{\partial P_s}{\partial P_x}\right)_H, \tag{2.49}$$

$$P_x' = \frac{\dot{P}_x}{\dot{s}} = -\frac{\left(\frac{\partial H}{\partial x}\right)_{P_s}}{\left(\frac{\partial H}{\partial P_s}\right)_x} = \left(\frac{\partial P_s}{\partial x}\right)_H, \tag{2.50}$$

$$y' = \frac{\dot{y}}{\dot{s}} = \frac{\left(\frac{\partial H}{\partial P_y}\right)_{P_s}}{\left(\frac{\partial H}{\partial P_s}\right)_{P_y}} = -\left(\frac{\partial P_s}{\partial P_y}\right)_H, \tag{2.51}$$

$$P_y' = \frac{\dot{P}_y}{\dot{s}} = -\frac{\left(\frac{\partial H}{\partial y}\right)_{P_s}}{\left(\frac{\partial H}{\partial P_s}\right)_y} = \left(\frac{\partial P_s}{\partial y}\right)_H, \tag{2.52}$$

$$H' = -\frac{\partial P_s}{\partial t}, \tag{2.53}$$

$$t' = \frac{\partial P_s}{\partial H}. \tag{2.54}$$

Looking at these equation we observe that we have a Hamiltonian system of equations where $(s, -P_s)$ is the independent variable and where the new Hamiltonian is

$$\mathcal{H} = -P_s\left(x, P_x, y, P_y, t, -H\right) \tag{2.55}$$

$$\Rightarrow \mathcal{H} = -(1+hx)\left\{\sqrt{\left(\frac{H-q\Phi}{c}\right)^2 - (P_x - qA_x)^2 - (P_y - qA_y)^2 - m^2c^2} + qA_s\right\}, \tag{2.56}$$

where the canonical variables are the pairs (x, P_x), (y, P_y) and $(t, -H)$.

This Hamiltonian is the principal Hamiltonian in beam dynamics, it is expressed in the Frenet-Serret coordinate system and it is a s-dependent Hamiltonian [19].

This Hamiltonian depends parametrically on the magnetic and electric fields present in the machine through the scalar and vector potentials. The usual equations of motion apply and they give the s-evolution of the transverse positions and momenta (the transverse dynamics) but also the variation of the energy of the particle (H) and the "schedule" of the particle (t) (longitudinal dynamics). At this point these two dynamics are intimately coupled and we shall discuss later approximations leading to a Hamiltonian where they are decoupled.

The total energy of the particle is $E = H - q\Phi$ and its momentum is given by $P = \sqrt{E^2/c^2 - m^2c^2}$. We now introduce our first approximation:

Approximation 1. As the transverse momenta P_x and P_y are much smaller than the total momentum we can Taylor expand the Hamiltonian (2.56) in P_x and P_y [14]. Expansion to the second order gives the Hamiltonian [20]

$$\mathcal{H}_1 = -P\left(1 + \frac{x}{\rho}\right) + \frac{1 + \frac{x}{\rho}}{2P}\left[(P_x - qA_x)^2 + (P_y - qA_y)^2\right] - (1 + \frac{x}{\rho})qA_s. \tag{2.57}$$

[19] It is worth noting that even if this is a s-dependent Hamiltonian, in the literature, the choice of s as the independent variable is so often made that this Hamiltonian is sometimes called a time-dependent Hamiltonian.

[20] In our notation the subscript of the Hamiltonian refers to the successive degree of approximation with respect to equation (2.56).

The second approximation that can directly be made concerns the potentials.

Approximation 2. As we consider mainly a synchrotron where the magnetic fields are transverse and neglecting the acceleration itself we can assume $A_x = A_y = 0$ and $\Phi = 0$. The Hamiltonian then reads

$$\mathcal{H}_2 = -P\left(1 + \frac{x}{\rho}\right) + \frac{1 + \frac{x}{\rho}}{2P}\left(P_x^2 + P_y^2\right) - (1 + \frac{x}{\rho})qA_s, \tag{2.58}$$

with the momentum given by $P = \sqrt{H^2/c^2 - m^2c^2}$.

We now obtained the Hamiltonian of the motion in a suitable form. The next step is to express the potential vector in our system of coordinates to provide a model of the magnetic field for the elements of our machine.

Expression of the magnetic field

We assume a separate function lattice, *i.e.* a lattice where the sector magnets provide only a dipolar field and where quadrupolar and higher-order magnets are straight elements. This approximation is valid in any case for large rings as, if the curvature is small, it provides consistent results even if the machine features a combined-function lattice [25].

We also neglect fringe-fields and longitudinal fields, such as solenoids, and therefore the magnetic field is assumed to be only two-dimensional, in the transverse plane of the magnets. This simplifies the equations as only the A_s component of the vector potential is different from zero. A more complete derivation in a generic case can be found in [3].

For all but the dipole magnets we use the Cartesian geometry where we have $B_x = -\frac{\partial A_s}{\partial y}$ and $B_y = \frac{\partial A_s}{\partial x}$. The vector potential can be written as a multipole expansion [25]:

$$\frac{q}{p_0}A_s = -\operatorname{Re}\sum_{n=1}^{\infty}\frac{1}{n}\left[ia_n(s) + b_n(s)\right](x + iy)^n, \tag{2.59}$$

where n is the order of the $2n$-pole magnet. The coefficients b_n are for the regular multipoles while the a_n are those of the skew multipoles. As we do not consider coupling between the two transverse plane we can assume there is no skew multipoles and the vector potential developed up to the fourth order is

$$\frac{q}{p_0}A_s = -\frac{b_2}{2}(x^2 - y^2) - \frac{b_3}{3}(x^3 - 3xy^2) - \frac{b_4}{4}(x^4 - 6x^2y^2 + y^4), \tag{2.60}$$

where we removed the dipolar term as we consider that the dipoles are sector magnets.

We finally have the magnetic field expanded to the fourth order (dipoles, quadrupoles, sextupoles and octupoles):

$$B_y = -\frac{p_0}{q}\left(b_1 + b_2x + b_3(x^2 + y^2) + b_4(x^3 - 3xy^2)\right), \text{ and} \tag{2.61}$$

$$B_x = -\frac{p_0}{q}\left(b_2y + b_3xy + b_4(y^3 - 3x^2y)\right). \tag{2.62}$$

The situation in the curvilinear system is more complicated, but restricting ourselves to the dipolar case of a piece-wise constant field we obtain the following solution for the vector potential [25]:

$$\frac{q}{p_0}A_s = -\frac{b_1}{2}\frac{1 + hx}{h}, \tag{2.63}$$

where h local curvature of the magnet. The field is then given by $B_y = -\frac{p_0}{q} b_1$ which is the dipolar field of the dipole magnet.

Transverse Hamiltonian

We are now able to express the Hamiltonian for the transverse motion. As the longitudinal dynamics can be neglected and as no longitudinal field is present, the energy (the third canonical coordinate) or the momentum can be viewed as a parameter of the motion [21](its canonical conjugate, the time was no present directly in the Hamiltonian and the fields are assumed to be time independent). In addition we shall refer to the normalize momentum deviation with respect to the parameter δ:

$$\delta = \frac{P - P_0}{P_0}, \tag{2.64}$$

where P_0 is given *a priori*.

In these variable we have the Hamiltonian $\mathcal{H}_2 = \mathcal{H}_2(x, P_x, y, P_y; \delta)$.

Before we insert the fields in the Hamiltonian we introduce one more approximation related to the choice of the canonical variables.

Approximation 3. As the momentum of the reference particle is constant (approximation of no acceleration) we can normalize both the Hamiltonian itself and the transverse momenta with the total momentum of the reference particle [22]. This leads to the Hamiltonian

$$\mathcal{H}_3 = -(1 + \frac{x}{\rho}) \left(1 + \delta - \frac{\tilde{P}_x^2 + \tilde{P}_y^2}{2(1+\delta)} + \frac{q}{P_0} A_s \right), \tag{2.65}$$

where $\mathcal{H}_3 = \mathcal{H}_2/p_0$ (apart from notational changes) and $\tilde{P}_{x,y} = P_{x,y}/P_0$.

We now introduce the expressions of the vector potential for the dipoles (equation (2.63)) and for the other multipoles (equation (2.60)) to obtain the Hamiltonian parameterized by the multipole coefficients.

Approximation 4. Under the approximation concerning the vector potential of section 2.2.3 we obtain the following Hamiltonian:

$$\mathcal{H} = -(1+hx) \left[1 + \delta - \frac{\tilde{P}_x^2 + \tilde{P}_y^2}{2(1+\delta)} \right] + \frac{b_1}{2} \frac{(1+hx)^2}{h} + \frac{b_2}{2}(x^2+y^2) + \frac{b_3}{3}(x^3 - 3xy^2) + \frac{b_4}{4}(x^4 - 6x^2y^2 + y^4). \tag{2.66}$$

In this Hamiltonian the curvature term does not appear in the multipole terms as it is assumed to be zero in the multipoles magnets (*i.e.* where the multipole coefficients are different from zero). We now also formally set the fact that the dipole magnets actually define the reference trajectory upon which the Frenet-Serret coordinates are constructed. This means that the magnetic rigidity (see equation (2.2)) of the reference particle corresponds to the dipolar field. This leads to the Hamiltonian $\mathcal{H}_4$ (the constant terms are removed as they do not contribute to the equations of motion):

$$\mathcal{H}_4 = (1+hx) \frac{\tilde{P}_x^2 + \tilde{P}_y^2}{2(1+\delta)} - b_1 x\delta + \frac{b_1^2}{2} x^2 + \frac{b_2}{2}(x^2+y^2) + \frac{b_3}{3}(x^3 - 3xy^2) + \frac{b_4}{4}(x^4 - 6x^2y^2 + y^4). \tag{2.67}$$

[21] Even if there is no acceleration, particles can have a constant momentum different from the one of the reference particle.

[22] One should note that by doing so we make both the Hamiltonian and the transverse momenta dimensionless.

This is almost our final Hamiltonian. To be complete we introduces one last step and approximation: in the accelerator physics literature and codes it is customary to use (x, x') and (y, y') as coordinates instead of (x, P_x) and (y, P_y). The coordinate x' is $\frac{dx}{ds}$ (and the same for y') and can be geometrically interpreted as the divergence angle in the paraxial approximation ($x' \ll 1$). Although this is a valid approximation in all practical cases, it is not evident that this gives a valid set of coordinates; indeed these coordinates might not be canonical. Nevertheless we can verify that if we write the expression of x' from the Hamilton equations of motion using our Hamiltonian (2.67):

$$x' = \frac{\partial H}{\partial P_x} = (1 + hx)\frac{\tilde{P}_x}{1+\delta} = (1 + hx)\frac{P_x}{P}. \tag{2.68}$$

We observe that x' is not equal to P_x, the canonical momentum conjugated to x. Nonetheless if we assume that we are at constant energy and if we can neglect the curvature term, (x, x') could be considered as a conjugated pair up to the normalization with respect to the momentum [23]. This is the object of our last approximation:

Approximation 5. In the expansion (2.67) of the Hamiltonian the curvature in the kinematic term can be neglected. This approximation is justified for large rings where $\frac{1}{\rho^2} \ll b_2$ [26], for smaller rings this term should be considered while using a high order Hamiltonian. If we indeed neglect this term we obtain the final Hamiltonian $\mathcal{H}_5$:

$$\mathcal{H}_5 = \frac{\tilde{P}_x^2 + \tilde{P}_y^2}{2(1+\delta)} - b_1 x\delta + \frac{b_1^2}{2}x^2 + \frac{b_2}{2}(x^2 + y^2) + \frac{b_3}{3}(x^3 - xy^2) + \frac{b_4}{4}(x^4 - 6x^2y^2 + y^4). \tag{2.69}$$

This is the Hamiltonian of the transverse motion in its final form. It includes the kinematic terms expanded to the second order and the field terms up to the octupoles. The energy dependence is viewed has an external parameter δ. It should also be kept in mind that the accelerator lattice itself is modeled by the s-dependence of the multipole coefficients.

Using this Hamiltonian, x' can be considered to be a canonical variable if we stay at constant energy. In the following chapters, as we shall consider the MTE process which takes place at constant energy, we shall use the the phase space variables (x, x') and (y, y').

Generalized Hill's equations

The Hamiltonian (2.69) is considered as the main equation for the transverse dynamics. Using the Hamilton equations we can derive the equations of motion:

$$x' = \frac{\partial \mathcal{H}_5}{\partial \tilde{P}_x} = \frac{\tilde{P}_x}{1+\delta} \tag{2.70}$$

$$\tilde{P}_x' = -\frac{\mathcal{H}_5}{\partial x} = b_1\delta - (b_1^2 + b_2)x - b_3(x^2 - y^2) - b_4(x^3 - 3xy^2) \tag{2.71}$$

$$y' = \frac{\partial \mathcal{H}_5}{\partial \tilde{P}_y} = \frac{\tilde{P}_y}{1+\delta} \tag{2.72}$$

$$\tilde{P}_y' = -\frac{\mathcal{H}_5}{\partial y} = b_2 y + 2b_3 xy + b_4(y^3 - 3x^2 y). \tag{2.73}$$

[23] In any case if A_x and A_y were not equal to zero, x' couldn't be considered a canonical variable.

Therefore we can write $x'' = \frac{\tilde{P}'_x}{1+\delta}$ (same for the y equations) and we obtain equations usually called the "generalized Hill's equations":

$$\begin{cases} x'' + b_1\delta - (b_1^2 + b_2)x - b_3(x^2 - y^2) - b_4(x^3 - 3xy^2) = 0 \\ y'' - b_2 y + 2b_3 xy + b_4(y^3 - 3x^2 y) = 0 \end{cases} \tag{2.74}$$

If we consider a on-momentum particle with $\delta = 0$ and if we drop the nonlinear terms, we recover the Hill's equations (2.20).

2.3 Transverse motion in the transfer maps formalism

We introduced the equations of the transverse motion from the Hamiltonian formalism and we established the generalized Hill's equations (equations (2.74)). We shall now discuss how these equation can be analyzed using the transfer maps formalism, a formalism allowing to obtain the solution in a discrete number of points by propagating initial conditions.

Under a good approximation, the magnetic elements can be assumed to have constant gradients. Therefore one can try to represent the effect of the element using a transfer map. The transfer map of the i^{th} element of the accelerator as $\boldsymbol{\mathcal{M}}^{(i)}$. Figure 2.5 details this model of the representation of an accelerator and the transfer maps of the magnetic elements.

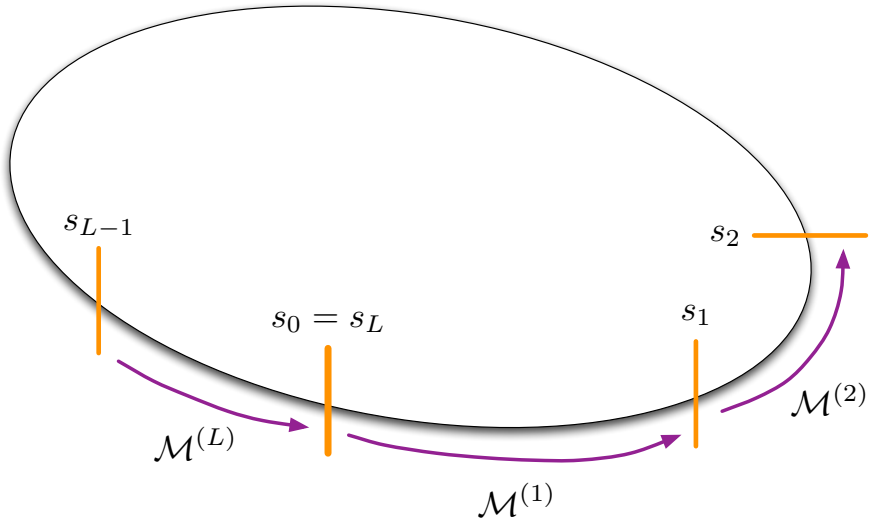

Figure 2.5: An idealized accelerator whose magnetic elements are piecewise constant. Each is represented by its transfer map from coordinates s_{i-1} to s_i.

We represent the coordinates of the particles in the 4D transverse phase space by

$$\boldsymbol{x} = \begin{pmatrix} x_1 \\ x_2 \\ x_3 \\ x_4 \end{pmatrix} = \begin{pmatrix} x \\ p_x \\ y \\ p_y \end{pmatrix}. \tag{2.75}$$

The transfer map $\boldsymbol{\mathcal{M}}^{(i)}$ can be written down in its components:

$$\begin{aligned} x_1(s_i) &= \boldsymbol{\mathcal{M}}_1^{(i)}\left(\boldsymbol{x}(s_{i-1})\right) \\ x_2(s_i) &= \boldsymbol{\mathcal{M}}_2^{(i)}\left(\boldsymbol{x}(s_{i-1})\right) \\ x_3(s_i) &= \boldsymbol{\mathcal{M}}_3^{(i)}\left(\boldsymbol{x}(s_{i-1})\right) \\ x_4(s_i) &= \boldsymbol{\mathcal{M}}_4^{(i)}\left(\boldsymbol{x}(s_{i-1})\right), \end{aligned} \tag{2.76}$$

where $\boldsymbol{\mathcal{M}}_j^{(i)}$ is a function from $\Re^4$ to $\Re$ ($j = 1, 2, 3, 4$).

Although this theoretically allows to propagate the initial conditions to reconstruct the motion, *i.e.* to solve the equation of motion, the transfer maps of each the magnetic elements has to be obtained first. In general it is not possible to have the exact transfer map of an element but we shall see that under some approximations one can construct an approximation of the actual transfer map.

In the next subsections we shall first introduce some general properties and definitions and then we shall discuss how the transfer maps of some linear and non linear elements can be constructed.

2.3.1 Symplectic matrices and maps

The equations of motion (equations (2.70)) are derived from the fundamental transverse time-dependent Hamiltonian (2.69). The transfer map are thus equivalent to the Hamiltonian flow propagating the coordinates $\boldsymbol{x}(s_{l-1})$ to $\boldsymbol{x}(s_l)$ [27]. Therefore as the Hamilton equations exhibit directly the symplectic nature of the motion and the solutions of the equation of the motion are expected to satisfy this symplecticity, the transfer maps must preserve the symplecticity of the motion, *i.e.* their application to the initial coordinates of the particle must be symplectic. We thus briefly recall some notions about symplectic matrices and maps to be able to prove that the transfer maps we shall use are indeed symplectic:

Definition 1. A 4×4 matrix $\boldsymbol{A}$ is symplectic if it satisfies

$$\boldsymbol{A}\boldsymbol{J}\boldsymbol{A}^T = \boldsymbol{J}, \tag{2.77}$$

where $\boldsymbol{J}$ is defined as [24]

$$\boldsymbol{J} = \begin{pmatrix} 0 & 1 & 0 & 0 \\ -1 & 0 & 0 & 0 \\ 0 & 0 & 0 & 1 \\ 0 & 0 & -1 & 0 \end{pmatrix}. \tag{2.78}$$

From this definition of a symplectic matrix we can define a symplectic map [27]:

Definition 2. A map $\boldsymbol{\mathcal{M}} : \Re^4 \to \Re^4$ is symplectic if its Jacobian $\boldsymbol{M}_J$ is a symplectic matrix for every $\boldsymbol{x}$:

$$\boldsymbol{M}_J(\boldsymbol{x})\boldsymbol{J}\boldsymbol{M}_J^T(\boldsymbol{x}) = \boldsymbol{J}. \tag{2.79}$$

[24] This assumes the coordinates are ordered as in equation (2.75) [22] as $\boldsymbol{J}$ just represents the signs of the Hamilton equations written in the matrix form.

In 2D, the matrix $\boldsymbol{J}$ reduces to

$$\boldsymbol{J} = \begin{pmatrix} 0 & 1 \\ -1 & 0 \end{pmatrix} \tag{2.80}$$

and it is easily shown that the symplectic conditions for a matrix $\boldsymbol{M}$ is equivalent to the area preserving condition $|\boldsymbol{M}| = 1$.

A more detailed discussion of the properties of symplectic maps and matrices, and their relation with the Hamiltonian formalism can be found in [22].

2.3.2 Poincaré map and orbit tracking

The Hamiltonian (2.69) describe the motion of the particles around the circular machine but we shall mostly be interested in the transverse coordinates of the particles at a given location, on a turn by turn basis: this is called a *Poincaré section* of the Hamiltonian motion. The transfer map formalism provides this information directly as we can compose the individual transfer maps in a single *one-turn* map, called the Poincaré map. As the individual transfer maps represent the Hamiltonian flow and thus the motion governed by the Hamiltonian dynamics, the Poincaré map represents the Hamiltonian flow over one turn.

This map transform the coordinates $\boldsymbol{x}(s_0)$ of a particle into its coordinates $\boldsymbol{x}(s_L)$ after one complete revolution. The Poincaré map $\boldsymbol{\mathcal{M}}$ is defined by

$$\boldsymbol{x}(s_L) = \boldsymbol{\mathcal{M}}\left(\boldsymbol{x}(s_0)\right) \tag{2.81}$$

or using a more compact notation

$$\boldsymbol{x}' = \boldsymbol{\mathcal{M}}\left(\boldsymbol{x}\right), \tag{2.82}$$

where

$$\boldsymbol{\mathcal{M}} = \boldsymbol{\mathcal{M}}^{(L)} \circ \boldsymbol{\mathcal{M}}^{(L-1)} \circ \boldsymbol{\mathcal{M}}^{(L-2)} \circ \cdots \circ \boldsymbol{\mathcal{M}}^{(2)} \circ \boldsymbol{\mathcal{M}}^{(1)}, \tag{2.83}$$

following the notation of figure 2.5.

Usually the transfer map are polynomial and the Poincaré map is obtained by the composition of individual transfer maps. The resulting map is then easily written as a Taylor serie of the form

$$x_j(s_L) = \sum_{i_1,i_2,i_3,i_4 \geq 0} m_{j;i_1,i_2,i_3,i_4} \left(x_1(s_0)\right)^{i_1} \left(x_2(s_0)\right)^{i_2} \left(x_3(s_0)\right)^{i_3} \left(x_4(s_0)\right)^{i_4}, \tag{2.84}$$

that in practice is truncated at some order.

In this work we assume that the closed-orbit is located at $x(s) = p_x(s) = y(s) = p_y(s) = 0$ all around the machine (this assumes that all particles have the reference momentum), *i.e.* for all s and therefore the Poincaré map $\boldsymbol{\mathcal{M}}$ will have no constant term, the first term of $\boldsymbol{\mathcal{M}}$ is thus linear:

$$\boldsymbol{M}(\boldsymbol{x}) = \boldsymbol{L}(\boldsymbol{x}) + O\left(|\boldsymbol{x}|^2\right), \tag{2.85}$$

where the linear part can be written as a 4×4 matrix $\boldsymbol{L}$:

$$\boldsymbol{x}'_j = \sum_{k=1}^{4} \boldsymbol{L}_{j,k} x_k. \tag{2.86}$$

The orbit along the machine is obtained by the tracking of an initial condition $\boldsymbol{x}(s_0)$ using the transfer maps:

$$\boldsymbol{x}(s_{jL+l}) = \boldsymbol{\mathcal{M}}^{(l)}\left(\boldsymbol{x}(s_{jL+l-1})\right), \tag{2.87}$$

where $\boldsymbol{x}(s_{jL+l})$ is the orbit in $s = s_l$ after j complete turns.

To obtain the Poincaré section of a given location we have to iterate the Poincaré map $\boldsymbol{\mathcal{M}}(s_l)$ for fixed l:

$$\boldsymbol{x}\left(s_{(j+1)L+l}\right) = \boldsymbol{\mathcal{M}}\left(s_l; \boldsymbol{x}\left(s_{jL+l}\right)\right). \tag{2.88}$$

The Poincaré section is then given by the truncated sequence $\left\{\boldsymbol{x}\left(s_{(j+1)L+l}\right)\right\}_{j=0}^{N}$. This is the basis of the tracking code that we describe in chapter 5.

2.3.3 Linear transfer maps and linear normal forms

To build a model of a machine using the transfer map formalism, we thus need to obtain the transfer maps for each elements of the machine and to construct the Poincaré map from it.

As we discussed in chapter 2, the design and the analysis of a machine usually involves two steps: first the linear lattice of the machine and second the nonlinearities. In addition, usually there is only a few important nonlinear magnetic elements that need to be modeled.

To build the Poincaré map of a machine we first need to obtain the linear transfer maps of the elements, in the linear case they are just transfer matrices defined by equation (2.86).

The transfer matrices of the linear elements (drift space, dipole, focusing or defocussing quadrupole) can be easily obtained and are discussed in great details in [3, 14, 16, 21]. In spite of that, it is also possible to directly construct the general transfer matrix of a linear lattice because a formal solution to the linear Hill's equations can be obtained.

Solutions of the linear betatron motion

We consider here the equations of motion for a linear lattice, considering only on-momentum particles ($\delta = 0$). As the derivation is the same for both plane, we consider only the horizontal equation of motion:

$$x'' + K(s)x = 0 \tag{2.89}$$

obtained from equation (2.74). This equation can be solved using what is called the Floquet transformation [14, 21]:

$$x(s) = aw(s)e^{i(\psi s+\eta)}, \tag{2.90}$$

$$x'(s) = aw(s)e^{-i(\psi s+\eta)}. \tag{2.91}$$

where a is a constant, $w(s)$ is called the amplitude function and $\psi(s)$ is the phase function. If we inject these ansatz in the Hill's equation, assuming that $K(s)$ is real as it is the case for our purposes we obtain

$$w'' + K(s)w - \frac{1}{w^3} = 0, \tag{2.92}$$

$$\psi' = \frac{1}{w^2}. \tag{2.93}$$

The first equation is called the *betatron envelope equation* and the second is the *phase equation* [14]. The first equation is a nonlinear differential equation which will not be of great

help to solve the problem, but the other equation provides the relation between w and ψ. The function $w(s)$ does not need to be periodic, but as we have the periodicity L (the circumference of the accelerator) we are allowed to choose $w(s)$ to have the same periodicity, this is the Floquet theorem [21]. In addition the theorem states that the phase function also satisfy: $\psi(s+L) - \psi(s) = 2\pi\mu$ where μ is independent of s.

The solutions to the linear motion are thus similar to those of an oscillator, where the amplitude and phase advance are s-dependent.

Linear transfer map

We are now able to write a transfer map using the solution written in term of $w(s)$ and $\psi(s)$. First we want the transfer map between $s = s_1$ and $s = s_2$ using the initial condition $x(s_1)$ where $w(s_1) = w_1$ and $\psi(s_1) = \psi_1$ (the same notation in s_2). After a little algebra we obtain the transfer matrix $\boldsymbol{M}(s_2|s_1)$:

$$\boldsymbol{M}(s_2|s_1) = \begin{pmatrix} \frac{w_2}{w_1}\cos\psi - w_2 w_1' \sin\psi & w_1 w_2 \sin\psi \\ -\frac{1+w_1 w_1' w_2 w_2'}{w_1 w_2}\sin\psi - \left(\frac{w_1'}{w_2} - \frac{w_2'}{w_1}\right)\cos\psi & \frac{w_1}{w_2}\cos\psi + w_1 w_2' \sin\psi \end{pmatrix}, \tag{2.94}$$

where $\psi = \psi(s_2) - \psi(s_1)$.

If we consider a special case for the matrix (2.94) where we write a one-turn matrix we obtain (using the results of the Floquet theorem):

$$\boldsymbol{M} = \begin{pmatrix} \cos\psi - ww'\sin\psi & w^2\sin\psi \\ -\frac{1+w^2w'^2}{w^2}\sin\psi & \cos\psi + ww'\sin\psi \end{pmatrix}, \tag{2.95}$$

At this point it is customary to introduce what is known to be the Courant-Snyder parameterization which is a central point in accelerator physics. A we discussed, the matrix (2.95) has to be symplectic, and being a 2×2 matrix, it has to have a unit modulus. Such a matrix can be parameterized as [14]

$$\boldsymbol{M} = \begin{pmatrix} \cos\psi + \alpha\sin\psi & \beta\sin\psi \\ -\gamma\sin\psi & \cos\psi - \alpha\sin\psi \end{pmatrix} \tag{2.96}$$

where α, β and γ are the Courant-Snyder parameters, where $\beta\gamma = 1 + \alpha^2$. ϕ is the phase advance. We want to express our solution in the Courant-Snyder parameterization, to do that we equate the matrices (2.95) and (2.96) to obtain

$$w^2 = \beta, \text{ and} \tag{2.97}$$

$$\alpha = -ww' = -\frac{\beta'}{2}. \tag{2.98}$$

The Courant-Snyder parameters characterize completely a linear lattice. The function β (or beta-function) is called the *betatron amplitude function* and we see that the parameter α is related to the slope of the beta-function. In addition we call Φ the one-turn *betatron phase advance* or simple the "tune" ν:

$$\Phi = \nu = \int_0^L \frac{ds}{\beta(s)}. \tag{2.99}$$

Equation (2.96) represents the Poincaré map of a linear lattice expressed in the Courant-Snyder parameterization. It is therefore a fundamental matrix as periodic linear lattices form the basis of the models including nonlinear elements.

These parameters can be computed manually or using a computer code by equating the one-turn matrix (2.96) at one location s with the composition of the individual transfer matrices of the linear elements. This procedure should be repeated for different locations, except for the phase advance which is independent of s.

The betatron functions α, β and γ are usually called the Twiss' parameters.

The result of such procedure is shown in figure 2.6 for a periodic lattice made of a few FODO cells.

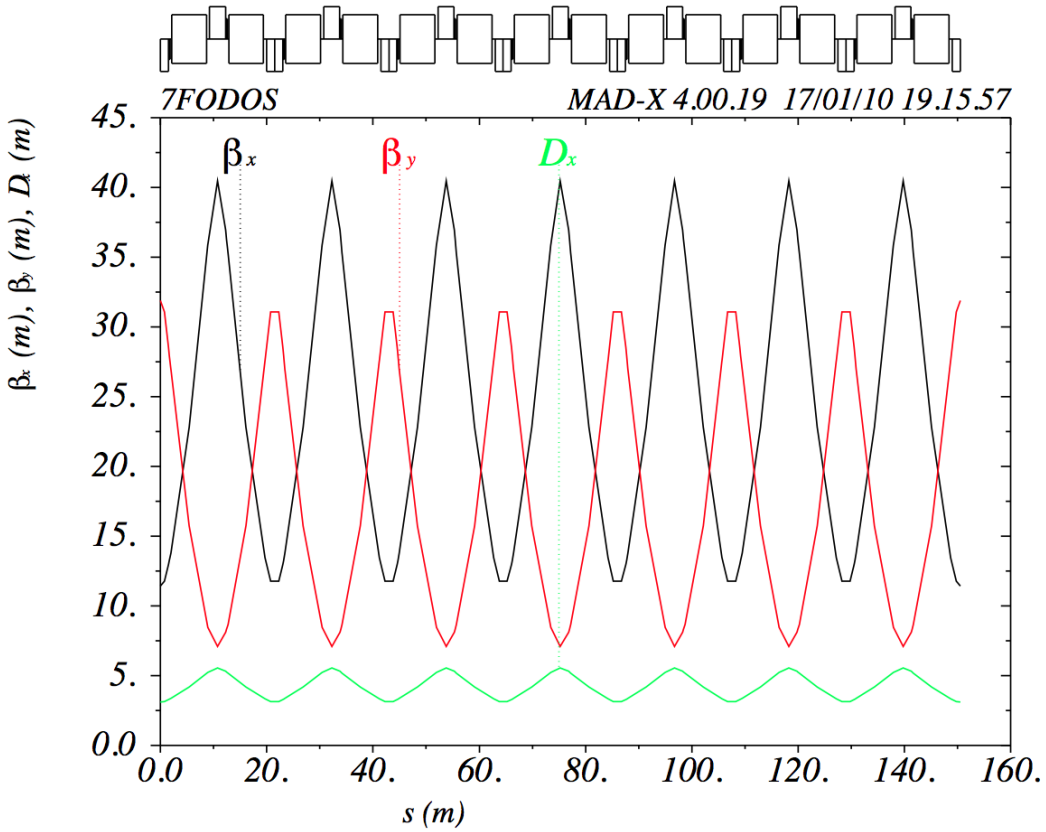

Figure 2.6: Beta-functions and dispersion of a periodic ring made of seven FODO cells. Obtained with [4]

Now going back from the one turn matrix expressed in the Courant-Snyder parameterization to the transfer matrix between two locations s_1 and s_2, we do the substitution (2.97) in the matrix (2.94) to obtain what we consider to be generic linear transfer map expressed in the usual Courant-Snyder lattice parameters:

$$\boldsymbol{M}(s_2|s_1) = \begin{pmatrix} \sqrt{\frac{\beta_2}{\beta_1}}\left(\cos\psi + \alpha_1 \sin\psi\right) & \sqrt{\beta_1\beta_2}\sin\psi \\ -\frac{1+\alpha_1\alpha_2}{\sqrt{\beta_1\beta_2}}\sin\psi + \frac{\alpha_1-\alpha_2}{\sqrt{\beta_1\beta_2}}\cos\psi & \sqrt{\frac{\beta_1}{\beta_2}}\left(\cos\psi - \alpha_2\sin\psi\right) \end{pmatrix}. \tag{2.100}$$

These derivations have been made in the 2D horizontal case but obviously it can be extended to the vertical plane. In the 4D case, the transfer matrices are defined as the direct product of the 2D matrices of each plane, each parameter being defined for both planes.

Linear normal form

We shall now express the linear transfer matrix in a formalism and using notation that shall be extended in chapter 4 where we discuss the normal forms. As we shall see our goal is to find a change of coordinates allowing to express the matrix (2.100) as a simple rotation. We shall see later that this is the normal form approach applied to the simple linear case.

Our starting point is the solution of the linear Hill's equation expressed in the Courant-Snyder parameterization, where the initial conditions are given by ϵ (we shall see that this parameter is related to the Courant-Snyder invariant) and η:

$$x(s) = \sqrt{\epsilon\beta(s)}\sin(\psi_x(s) + \eta). \tag{2.101}$$

The transfer matrix (2.100) transports the initial condition $x(s_0)$ to $x(s)$. We follow [27] to express the initial conditions as a vector:

$$\vec{w} = \begin{pmatrix} \sqrt{\epsilon}\sin\eta \\ \sqrt{\epsilon}\cos\eta \end{pmatrix}. \tag{2.102}$$

It allows writing (2.101) in compact notation [27]:

$$\boldsymbol{x}(s) = \boldsymbol{T}(s)\boldsymbol{R}(s)\boldsymbol{w}, \tag{2.103}$$

where $\boldsymbol{T}(s)$ is

$$\boldsymbol{T}(s) = \begin{pmatrix} \sqrt{\beta(s)} & 0 \\ -\frac{\alpha(s)}{\sqrt{\beta(s)}} & \frac{1}{\sqrt{\beta(s)}} \end{pmatrix} \tag{2.104}$$

and where $\boldsymbol{R}(s)$ is a rotation matrix whose angle is the phase function:

$$\boldsymbol{R}(s) = \begin{pmatrix} \cos\psi(s) & \sin\psi(s) \\ -\sin\psi(s) & \cos\psi(s) \end{pmatrix}. \tag{2.105}$$

If we evaluate (2.103) in $s = s_0 = 0$ we have $\boldsymbol{x}(0) = \boldsymbol{T}(0)\boldsymbol{w}$ and we can therefore express the coordinates at the location s in term of the initial condition $\boldsymbol{x}(0)$:

$$\boldsymbol{x}(s) = \boldsymbol{T}(s)\boldsymbol{R}(\psi(s))\boldsymbol{T}(0)^{-1}\boldsymbol{x}(0) \tag{2.106}$$

The one-turn matrix can then be expressed using the periodicity of $\boldsymbol{T}$:

$$\boldsymbol{x}' = \boldsymbol{L}\boldsymbol{x} \tag{2.107}$$

where the prime denotes the one-turn transport and where the Poincaré map $\boldsymbol{L}$ reads

$$\boldsymbol{L} = \boldsymbol{T}\boldsymbol{R}\boldsymbol{T}^{-1} \tag{2.108}$$

where $\boldsymbol{R} = \boldsymbol{R}(\psi_L)$ is a rotation where the angle is the one-turn phase advance.

The structure of this equation suggests that we define new coordinates conjugated to the coordinates $\boldsymbol{x}$. These are the *Courant-Snyder coordinates* $\hat{\boldsymbol{x}}$:

$$\hat{\boldsymbol{x}} = \boldsymbol{T}^{-1}\boldsymbol{x}. \tag{2.109}$$

In these coordinates, the motion over one turn is simply a rotation:

$$\hat{\boldsymbol{x}}' = \boldsymbol{R}\hat{\boldsymbol{x}}. \tag{2.110}$$

This procedure shall be exploited extensively when we shall discuss the normal forms in chapter 4. This conjugation process can be represented by the following commutation diagram [27]:

$$\begin{array}{ccc} \boldsymbol{x} & \xrightarrow{\quad\boldsymbol{L}\quad} & \boldsymbol{x}' \\ \Big\uparrow \boldsymbol{T} & & \Big\uparrow \boldsymbol{T} \\ \hat{\boldsymbol{x}} & \xrightarrow[\quad\boldsymbol{R}\quad]{} & \hat{\boldsymbol{x}}' \end{array} \tag{2.111}$$

The one-turn map $\boldsymbol{L}$ is a symplectic matrix. 2×2 symplectic matrices are required to have eigenvalues λ_1 and λ_2 such that $\lambda_1\lambda_2 = 1$. This set of real matrices can be classified in three groups depending of the absolute value of their trace:

$$|Tr\boldsymbol{A}| \begin{cases} < 2 & \lambda_1 = \lambda_2^* = e^{i\omega} \quad \text{with } \omega \in \Re & \text{elliptic case} \\ = 2 & \lambda_1 = \lambda_2 = \pm 1 & \text{parabolic case} \\ > 2 & \lambda_2 = 1/\lambda_1 = \pm e^{\tau} \quad \text{with } \tau \in \Re & \text{hyperbolic case} \end{cases} \tag{2.112}$$

where $|Tr\boldsymbol{A}|$ is the trace of $\boldsymbol{A}$.

The linear one-turn transfer map is always elliptic as the lattice is designed to lead to a stable motion [25].

To define the linear normal form one more step is required. An elliptic 2×2 matrix $\boldsymbol{A}$ can be diagonalized to the matrix $\boldsymbol{\Lambda}(\omega)$ [27]:

$$\boldsymbol{\Lambda}(\omega) = \begin{pmatrix} e^{i\omega} & 0 \\ 0 & e^{-i\omega} \end{pmatrix}. \tag{2.113}$$

This matrix is the *elliptic linear normal form* of $\boldsymbol{A}$. To put our one-turn transfer matrix into its normal form representation we use one more conjugating matrix:

$$\boldsymbol{K}^{-1} \equiv \begin{pmatrix} 1 & -i \\ 1 & i \end{pmatrix}. \tag{2.114}$$

With this matrix we transform the Courant-Snyder coordinates into the *complex Courant-Snyder* coordinates:

$$\begin{pmatrix} z \\ z^* \end{pmatrix} = \boldsymbol{K}^{-1}\begin{pmatrix} \hat{\boldsymbol{x}} \\ \hat{\boldsymbol{p}}_x \end{pmatrix} \equiv \begin{pmatrix} \hat{\boldsymbol{x}} - i\hat{\boldsymbol{p}}_x \\ \hat{\boldsymbol{x}} + i\hat{\boldsymbol{p}}_x \end{pmatrix}. \tag{2.115}$$

We can summarize these last steps in a few words:

[25] The following procedure can be done also for the hyperbolic case (and the parabolic case), details can be found in [27].

- The solution of the linear Hill's equation are in the form an anharmonic oscillator using the Floquet transformation;
- from this solution we construct a transfer matrix in term of the amplitude function and phase function;
- using the Floquet theorem to express the periodicity of the machine we write the one-turn map and we parameterize it using the Courant-Snyder parameterization;
- equalities between the Courant-Snyder parameters and the parameters of the Floquet solution provides the transfer matrix in term of the betatron functions and phase;
- we then transform our coordinates into the Courant-Snyder coordinates using the conjugating matrix $\boldsymbol{T}$;
- at this point the transfer matrix is simply a rotation $\boldsymbol{R}$ whose angle is the betatron phase advance.
- The last step is to conjugate the transfer matrix into its elliptic normal form using the change of coordinates from the Courant-Snyder coordinates to the complex Courant-Snyder coordinates made by the matrix $\boldsymbol{K}$
- this gives the transfer map of a linear lattice:

$$\begin{cases} z' = e^{i\omega} z \\ z'^{*} = e^{-i\omega} z^{*} \end{cases} \tag{2.116}$$

  where the second equation can be omitted as it is the complex conjugate of the first.

The transfer matrix in the physical canonical coordinates is $\boldsymbol{L}$ and it has been transformed into $\boldsymbol{\Lambda}$ *via*

$$\boldsymbol{L} = \boldsymbol{T}\boldsymbol{R}\boldsymbol{T}^{-1} = \boldsymbol{T}\boldsymbol{K}\boldsymbol{\Lambda}\boldsymbol{K}^{-1}\boldsymbol{T}^{-1}. \tag{2.117}$$

2.3.4 Nonlinear transfer maps

Transfer map of a single sextupole or octupole

We now analyze how we can construct a transfer map for nonlinear elements (we focus on sextupoles and octupoles) and we discuss the approximations that have to be done.

The transfer map of a nonlinear element $\boldsymbol{\mathcal{M}}$ cannot in general be obtained exactly [27]. Indeed the equations of motion are nonlinear:

$$\frac{d\boldsymbol{x}}{ds} = \boldsymbol{A}(s) + \boldsymbol{f}(x, y; s), \tag{2.118}$$

where $\boldsymbol{x}$ is given by equation (2.75) and $\boldsymbol{A}$ and $\boldsymbol{f}$ are based on the generalized Hill's equations (2.74) (on-momentum case as for the solution of the linear motion):

$$\boldsymbol{A}(s) = \begin{pmatrix} 0 & 1 & 0 & 0 \\ b_2(s) - \rho^{-2}(s) & 0 & 0 & 0 \\ 0 & 0 & 0 & 1 \\ 0 & 0 & -b_2(s) & 0 \end{pmatrix}, \tag{2.119}$$

and

$$\boldsymbol{f}(x,y;s) = \begin{pmatrix} 0 \\ f_x(x,y;s) \\ 0 \\ f_y(x,y;s) \end{pmatrix} = \begin{pmatrix} 0 \\ b_3(x^2-y^2)+b_4 \\ 0 \\ b_3 xy + b_4 \end{pmatrix}, \tag{2.120}$$

where we restricted the nonlinearities to normal sextupoles and octupoles.

These equations are nonlinear and no closed form solution exists. One can find a solution expressed in the integral form based on the linear transfer map of the system [27] but this is just a formal solution.

Two kind of approximations can be made to find an approached solution: the *thick lens* approximation and the *thin lens* approximation. The thick lens solution is a recursive method but it is not suitable for our purpose has it is not exactly symplectic [27]: the recursive solution at order n violates the symplectic condition with terms of order $|\boldsymbol{x}|^n$.

The thin lens approximation is the one that is most used, notably by tracking code. It allows the construction of a polynomial approximation of the map $\boldsymbol{\mathcal{M}}$ [27] that is exactly symplectic.

The idea of the approximation is to consider that the nonlinear element only acts in a discrete number of points, for example at the entrance of the element. Polynomial approximation can be build by composing the effect of these discrete kicks. Here we shall only use the one-kick approximation, *i.e.* the nonlinear content of $\boldsymbol{f}$ is assumed to act only at the entrance of the element [26].

We therefore make the substitution

$$\boldsymbol{f}(x,y;s) \to \boldsymbol{f}(x,y;s) l \delta(s - (s_{l-1} + 0)), \tag{2.121}$$

where l is the length of the element and δ is the "delta function". The presence of l in the expression assures that the integrated effect of the nonlinear element is preserved. The $+0$ denotes the fact that the nonlinearity acts just after the entrance of the element [27] (s_l is the coordinate at the exist of the element, as depicted in figure 2.5).

With this approximation we are now able to easily obtain the transfer map of the element: from $s_{l-1} + \epsilon$ to s_l, the nonlinearity is zero and therefore the partial transfer map is simply the linear transfer matrix $\boldsymbol{L}$:

$$\boldsymbol{x}(s_l) = \boldsymbol{L}(s_l, s_{l-1} + \epsilon)\boldsymbol{x}(s_{l-1} + \epsilon). \tag{2.122}$$

The kick given by the nonlinear content of $\boldsymbol{f}$ only affects the momentum and has no effect on the coordinate, therefore one can write

$$\begin{pmatrix} x \\ p_x \\ y \\ p_y \end{pmatrix}_{s=s_{l-1}+0} = \begin{pmatrix} x \\ p_x + l f_x(x,y;s) \\ y \\ p_y + l f_y(x,y;s) \end{pmatrix}_{s=s_l-1}. \tag{2.123}$$

For example, in the case of a sextupole we have

$$\begin{pmatrix} x \\ p_x \\ y \\ p_y \end{pmatrix}_{s=s_{l-1}+0} = \begin{pmatrix} x \\ p_x + K_2(x^2+y^2) \\ y \\ p_y + K_2 xy \end{pmatrix}_{s=s_l-1}, \tag{2.124}$$

[26] An example of two-kicks approximation is discussed in [27]

and for an octupole

$$\begin{pmatrix} x \\ p_x \\ y \\ p_y \end{pmatrix}_{s=s_{l-1}+0} = \begin{pmatrix} x \\ p_x + l f_x(x,y;s) \\ y \\ p_y + l f_y(x,y;s) \end{pmatrix}_{s=s_l-1}, \tag{2.125}$$

where K_2 and K_3 are the integrated gradients: $K_n = b_n l$ and l is the magnetic length of the magnet [28].

The transfer map of the complete element is then given by

$$\boldsymbol{x}(s_l) = \boldsymbol{L}(s_l, s_{l-1})(\boldsymbol{x}(s_{l-1})) + l\boldsymbol{f}(x,y;s_{l-1}). \tag{2.126}$$

When using the thin lens approximation, one should be concerned with the existence of the transfer map, *i.e.* the problem of the convergence of the Taylor expansion of the transfer map in a neighborhood of the reference orbit. The proof of the existence of the transfer map is given in [27] in the 2D case.

Nonlinear Poincaré map

The previous section gives the transfer map of single nonlinear element expressed in the physical coordinates. We discuss here the one-turn map that can be obtained for a lattice containing nonlinear elements. As this transfer map is obtained as a polynomial expansion we write

$$\boldsymbol{x}' = \boldsymbol{\mathcal{M}}(\boldsymbol{x}) = \sum_{n\geq 1} [\boldsymbol{\mathcal{M}}]_n (\boldsymbol{x}), \tag{2.127}$$

where $[\cdot]_n$ stands for the projection over the homogenous polynomial of order n [27]. The jth component of the map, at order n then reads

$$[\boldsymbol{\mathcal{M}}_j]_n = \sum_{i_1+i_2+i_3+i_4=n} m_{j;i_1,i_2,i_3,i_4} x^{i_1} p_x^{i_2} y^{i_3} p_y^{i_4}. \tag{2.128}$$

In general the one-turn map of a lattice that contains nonlinearities has to be obtained by the composition and truncation of the individual nonlinear maps. This can be done using different methods described in [27]. In our case we will deal with linear lattices containing only a single nonlinearity are therefore we are not directly concerned with this composition.

We can express our Poincaré map $\boldsymbol{\mathcal{M}}$ in the coordinates discussed in the previous section. We can first express the map in the Courant-Snyder coordinates and then in the complex Courant-Snyder coordinates or we can directly transform to the complex Courant-Snyder coordinates using the conjugation matrix $\boldsymbol{V}$:

$$\boldsymbol{z} = \boldsymbol{V}^{-1}\boldsymbol{x}, \tag{2.129}$$

where $\boldsymbol{z}$ are the complex Courant-Snyder coordinates and $\boldsymbol{V}$ is defined as $\boldsymbol{V} = \boldsymbol{T}\boldsymbol{K}$. The map $\boldsymbol{\mathcal{M}}$ is therefore transformed to the map $\boldsymbol{\mathcal{F}}$:

$$\boldsymbol{z}' = \boldsymbol{V}^{-1} \circ \boldsymbol{\mathcal{M}} \circ \boldsymbol{V}\boldsymbol{z} \equiv \boldsymbol{\mathcal{F}}(\boldsymbol{z}). \tag{2.130}$$

[27] Polynomial containing only monomials of order n.

The linear part of the map $\boldsymbol{\mathcal{F}}$ is simply the matrix $\boldsymbol{\Lambda}$ and the map can be written as

$$\boldsymbol{\mathcal{F}}(\boldsymbol{z}) = \boldsymbol{\Lambda}\boldsymbol{z} + \sum_{n\geq 2} [\boldsymbol{\mathcal{F}}]_n (\boldsymbol{z}), \tag{2.131}$$

or more explicitly for each components of $\boldsymbol{z}$, where the components of $\boldsymbol{\mathcal{F}}$ are defined as $\boldsymbol{\mathcal{F}} \equiv (F_1, F_1^*, F_2, F_2^*)$:

$$\begin{cases} z_1' &= e^{i\omega_1} z_1 + \sum_{n\geq 2} [F_1]_n (\boldsymbol{z}) \\ z_1^{*\prime} &= e^{-i\omega_1} z_1^* + \sum_{n\geq 2} [F_1^*]_n (\boldsymbol{z}) \\ z_2' &= e^{i\omega_2} z_2 + \sum_{n\geq 2} [F_2]_n (\boldsymbol{z}) \\ z_2^{*\prime} &= e^{-i\omega_2} z_2^* + \sum_{n\geq 2} [F_2^*]_n (\boldsymbol{z}) \end{cases} \tag{2.132}$$

where the generalization of the linear part for the four dimensional case has been done, introducing the tunes for both planes: ω_1 and ω_2.

The map (2.131) form the basis of the analysis of the nonlinear transverse dynamics. Nevertheless it is not as easily analyzable as the linear map. The linear map depends just on the tune of the machine and its properties are readily obtained: the map is reduced to a simple rotation in the phase space formed by the Courant-Snyder coordinates.

In addition the only fixed point of the linear map is the origin and by construction we made that fixed point elliptic and thus stable. Obviously, as the topology of the phase space is linear in that case, the whole phase space will be stable.

On the other hand the impact of the nonlinear map is more difficult to analyze: the origin is still elliptic and stable but the topology of the phase space is modified and one can obtain different structures. Additional fixed points can be created, either stable or unstable. The presence of unstable fixed points reduces the stable region around the origin: this region is called the *dynamic aperture* of the mapping.

We shall analyze such effects in chapter 3 in the case of the mapping modeling the MTE process.

CHAPTER 3

The Multi-Turn Extraction method

In this chapter we discuss the MTE extraction method itself: we first introduce the various CERN accelerators and their relationships in section 3.1 to understand the use made of the multi-turn extraction. Then we review the different methods used to extract a beam from a synchrotron: fast and slow extraction and two specific methods used to transfer the beam from the CERN PS to the SPS are described in section 3.2. Finally we present the advantages of the MTE method, the way it is implemented in the PS and the theoretical model upon which it is based is discussed in section 3.3.

3.1 Introduction to the CERN accelerator complex . . . 34
3.1.1 The CERN Proton Synchrotron machine . . . 36
3.1.2 Overview of extraction methods used at the PS . . . 38
3.1.3 The CNGS experiment . . . 40
3.2 Specific methods used for the PS to SPS transfer . . . 41
3.2.1 The CT method . . . 41
3.2.2 The MTE method and its implementation . . . 42
3.3 The modeling of the MTE method and the Hénon mapping . . . 45
3.3.1 Model for the MTE beam splitting . . . 45
3.3.2 The Hénon mapping and its fixed points . . . 47
3.3.3 Overview of the trapping process . . . 50

3.1 Introduction to the CERN accelerator complex

The CERN accelerators form a complete and interconnected accelerator complex comprising as its main elements, two LINACs and six synchrotrons [1]. These various accelerators form the

[1] We do not consider the electron machines of the CLIC Test Facility 3 (CTF3).

acceleration chain used to serve experiments ranging from nuclear physics at relatively low energy [2] to very high energy colliding beams physics with the LHC beams at 7 TeV.

In this view, the importance of the understanding of the extraction and transfer methods can be readily understood. Indeed, taking the example of the PS machine, up to four different extraction methods can be used during the same *supercycle*: fast extraction (*e.g.* LHC type beams), slow extraction (North Hall beams), and CT or MTE extraction for fixed-target SPS experiments or CNGS.

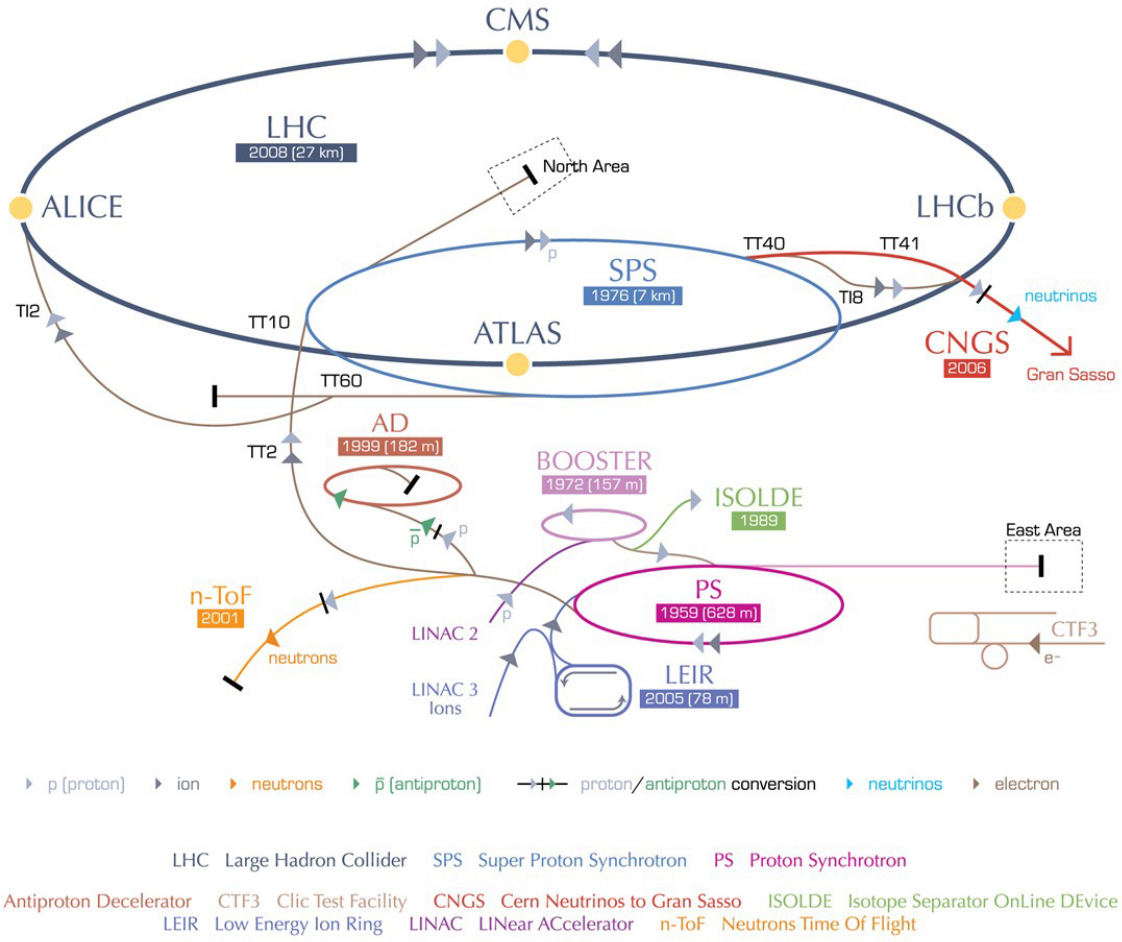

Figure 3.1: CERN accelerators complex schematic overview (from Ref. [5]). The path followed by the CNGS proton beam is highlighted.

Figure 3.1 schematically details these accelerators and the related transfer lines. The beams produced and manipulated consist of different types of particles: the main beam are either proton beams or ions beam [3] and secondary beams of neutrons and antiprotons are also produced and manipulated.

[2] This is the case of the ISOLDE experiment whose beam comes from the Proton Synchrotron Booster (PSB) at 1 GeV/c or 1.4 GeV/c.

[3] Currently lead ions, but in the past various ions we used: Deuteron, α particles, Sulfur, Indium and Oxygen.

These beams are uniformly controlled and produced using the so-called *supercycle* of the control system of the accelerators chain: a sequence of beams can be requested, each accelerator thus being controlled in a way that they are cycling in synchronism to serve each destination and experiments with the suitable beams.

The MTE extraction was designed to be used to serve the CNGS experiment. The journey of this proton beam through the complex is the following: the LINAC 2 provides a p^+ beam at 50 MeV injected in the PSB and accelerated at 1.4 GeV. This beam is injected in the PS, manipulated in view of the MTE extraction (as we describe bellow), accelerated to 14 GeV/c and extracted from the machine. It then follows the TT2 and TT10 transfer lines to be injected in the SPS where it undergoes the final acceleration to 400 GeV/c. The beam is finally extracted and directed to the CNGS proton target *via* the TT40 and TT41 lines.

3.1.1 The CERN Proton Synchrotron machine

From the previous discussion one can understand that the PS machine plays a key role as most of the beams are either directly used when extracted from it or were transferred and manipulated by the PS toward their final destination.

The PS was the first synchrotron at CERN; it was first operated in 1959. As we discussed in chapter 2 it is a strong-focusing synchrotron achieving a maximum energy of 26 GeV/c. For a review of its history and the various types of beams it produced, references [29, 30] can serve as a good basis for the interested reader.

The machine has a total circumference of 628 meters and comprises 100 main magnetic units and therefore 100 straight sections. The main magnets are combined function magnets: they act as the main dipole magnets and have the main quadrupoles. Each magnetic unit is divided in two halves: one with a (horizontally) focusing quadrupolar field and the other with a defocusing field (see figure 3.2). This gives the machine a "FD-O-DF-O" structure, where "O" stands for a section with no magnetic field (a straight section). Some straight sections are 3 meters long and others are 1.6 meters long (only 2.8m and 1m are available for the installation of elements). The main units form the linear lattice of the machine but in addition to their linear fields, higher-order multipoles are also generated by these magnets (due to the so-called "pole-face winding" [30]). For our purpose the lattice can be assumed to be a regular linear lattice (a simple Courant-Snyder rotation) with a discrete number of nonlinear components located in the straight sections.

Various components are located in these straight sections: kicker magnets, dipole correctors, septa, RF-cavities, nonlinear magnets, etc. For example the sextupoles and octupoles used for the MTE extraction are located in the straight sections 39 and 55. Figure 3.3 shows the straight section 55 where two MTE sextupoles (in yellow) and a MTE octupole (between the sextupoles in dark yellow) are placed.

The PS is able to handle a large variety of beams. A central notion in the CERN accelerator complex is the notion *supercycle*. As the main accelerators (LINAC2, PSB, PS and SPS) are controlled in an integrated way it is possible to define a sequence of beams that has to be produced by the different accelerators. These beam are scheduled in time for each accelerator. For example to produce a beam in the SPS it has to be produce first in the LINAC2, then extracted with the right timing to the PSB, etc. up to the injection in the SPS. The supercycle control system takes care of these requirements.

Figure 3.4 shows a typical sequence of beams in the PS. The overlays shows two CNGS beams that have been produce. One can observe that the supercycle also contains n-TOF, LHC

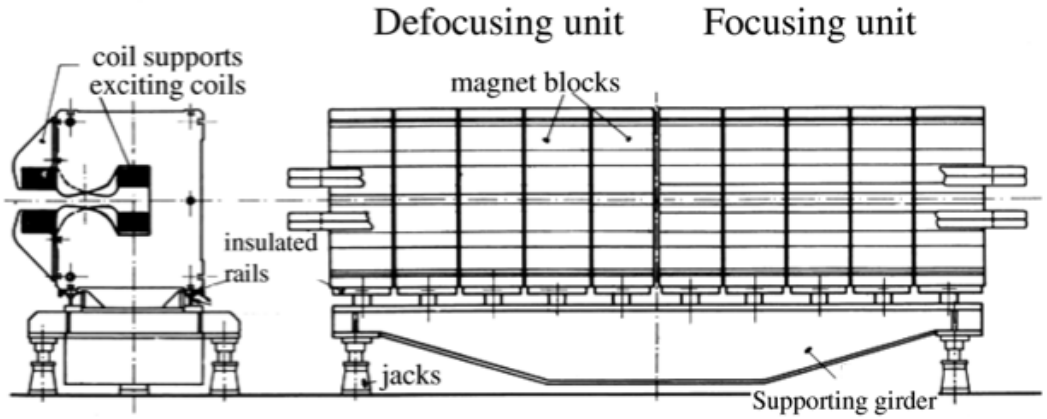

Figure 3.2: Schematic of a PS main magnetic unit (from Ref. [6]).

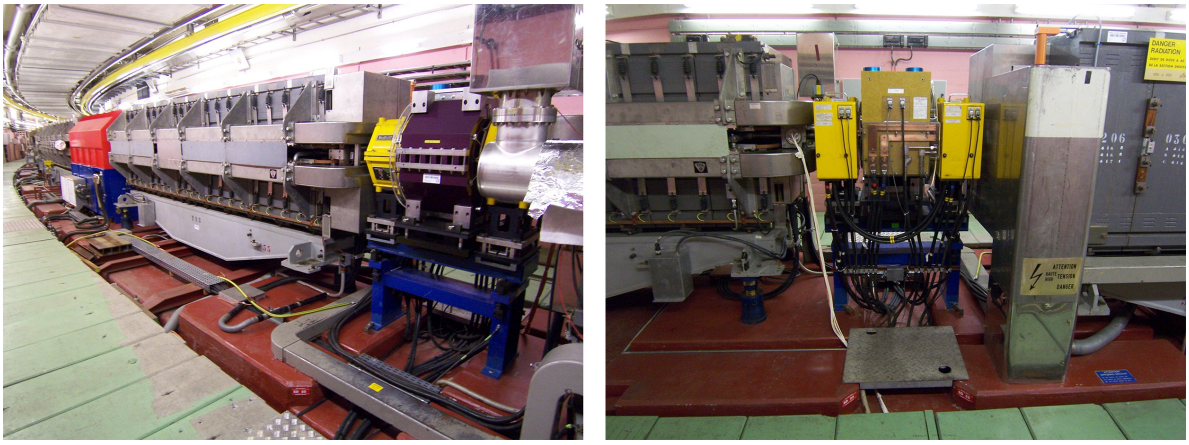

Figure 3.3: Pictures of the PS straight section 55 (from Ref. [7]): (left) on the right side of the picture, SS55 is shown and from right to left it shows a main magnetic unit, the SS56 and another MU (right) SS55 is shown from the other side.

and East Hall beams.

These beams, once produced, have to be extracted from the machine. Depending on the beam type different options exist: fixed-target beams can be slowly extracted to the East Hall, n-TOF beams can be fast extracted to the n-TOF experimental area and other beams can be extracted to the SPS. Three extraction methods are used for the transfer from the PS to the SPS (see section 3.2): fast extraction (for the different flavors of the LHC beams), the CT extraction (for North Hall beams and CNGS) and the new MTE extraction whose goal is to replace the CT extraction.

These beams are extracted by the magnetic septum of straight section 16 and are directed toward the transfer line TT2. In TT2 they are finally deflected to TT10, the transfer line used for injection of positively charged particles in the SPS.

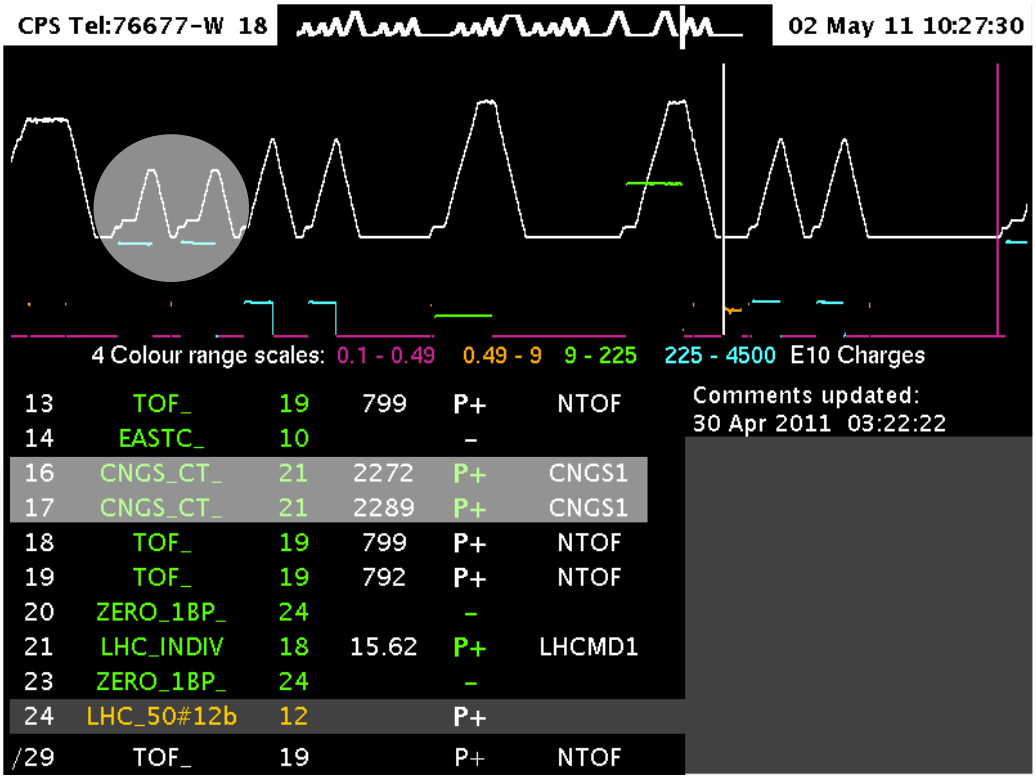

Figure 3.4: A typical sequence of beams in the PS. The light overlays shows two CNGS beams produced by the PS machine (from Ref. [8]).

3.1.2 Overview of extraction methods used at the PS

We describe here in more details the methods used to extract beams from the PS, either to a fixed-target experiment or to the SPS.

Fast extraction

This method is the more common extraction method used today in circular accelerators. In the case of the PS this was the first implemented extraction method but it required detailed design studies, as the method did not exist when the machine started its operation [9].

In this method, "fast" means that the beam (or only a selection of bunches) is extracted in one turn from the machine.

Figure 3.5 gives a schematic view of the orbit of a fast-extracted beam in the PS [4]

First the closed-orbit is deformed with dipole magnets (slow closed-bump) to put the beam orbit closer to the blade of the septum magnet (where the extraction itself will occur). Then, pulsed kicker magnets deflect the beam that then starts to oscillate around the deformed closed-orbit. The kickers are arranged in such a way that this oscillation puts the beam on the other side of the septum blade.

[4] In that case the beam was fast-extracted to the East Hall. Nowadays no fast extraction is used for the East Hall and the only fast-extraction implemented concerns the straight section 16.

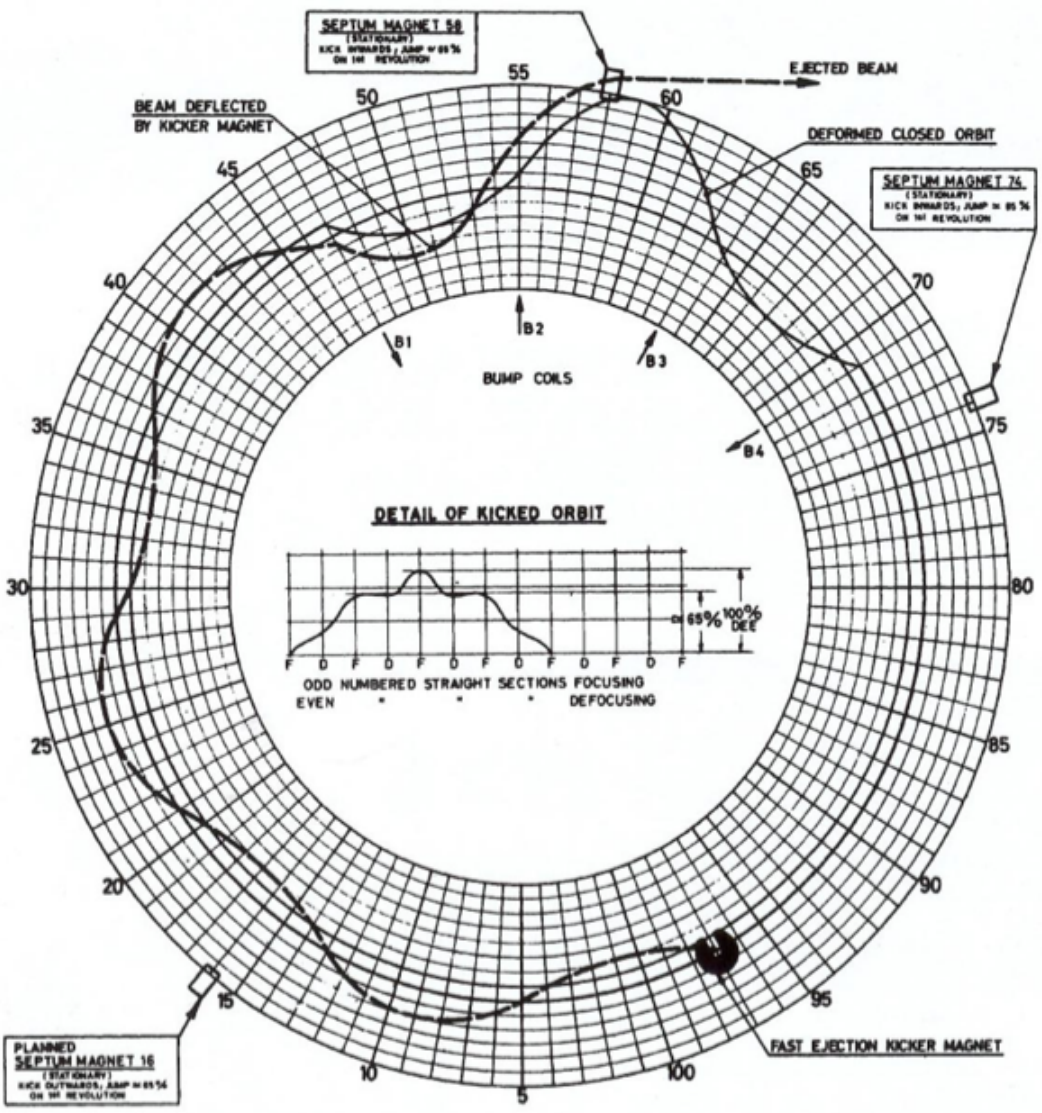

Figure 3.5: Orbit in the PS prior to a fast-extracted toward the East Hall (from Ref. [9]).

Currently this method is used in the PS to extract beams to the SPS and also to extract beams for the n-TOF experiment.

Slow extraction

To serve fixed-target experiments it is interesting to extract the beam over a large number of turns, thus providing a long spill (from a few milliseconds to a few seconds) to the experiments rather than a very short pulse.

Slow extraction, also called resonance extraction use nonlinear elements to deform the topology of the transverse phase space close to a resonance. Usually the third order resonance extraction is used. The tune is moved to the resonance value $Q_x = .33$ and the separatrix moves closer to the center thus reducing the space available for the beam [21]. Even if the tune

variation and the squeeze of the separatrix is slow, the motion of particles with large amplitude, *i.e.* close to the unstable fixed points, fails to be adiabatic. Therefore these particles "jump" on the other side of the separatrix and move in the unstable area following the outgoing "arms" of the separatrix [21].

These outgoing particles jump on the "out" side of a properly located very-thin (but weak) electrostatic septum and therefore receive a kick allowing them to be extracted by another stronger septum.

It is then possible to provide a slow extraction by properly tuning the nonlinear magnets (to adjust the phase space) and making the tune variation slow.

Multi-turn extraction

In addition to the two classical fast and slow extraction schemes, the PS features two unique extraction methods able to extract the beam in a few turns: the CT extraction and the MTE extraction methods. As our work is mainly concerned with these methods, we describe them in more details in section 3.2.

3.1.3 The CNGS experiment

The MTE method was developed to allow an intensity upgrade for the proton beams of the CNGS experiment. To be complete we quickly describe the CNGS experiment.

CNGS is a neutrino facility producing a neutrino beam from 400 GeV/c protons delivered by the SPS. The neutrino beam is directed towards the Gran Sasso Laboratory in Italy, located 732km from CERN [10] where it is detected. The goal of the experiment is to observe *neutrino oscillations*, oscillations of the neutrinos between two flavors (for example a neutrino oscillating between its electronic flavor and its muonic flavor). To detect these oscillations the idea is to produce a beam whose flavor composition is known and then detect the beam and observe a change in the composition. To make that measurement possible, a large distance between the production target and the detectors is needed to allow the neutrinos to oscillate at least once.

The Gran Sasso Laboratory is an underground laboratory thus providing shielding against cosmic rays; the minimum thickness of rock above the experimental halls is 1400m of rock. Only high energy neutrinos and muons can filter through that natural shielding and even then, the muon fluence in the laboratory is extremely low (about $1\mathrm{m}^{-2}\mathrm{h}^{-1}$).

The main idea is thus to produce a neutrino beam on the CERN side, direct it to Gran Sasso and leave the neutrinos travel to the detectors through the earth's surface.

Neutrino beams produced by an accelerator facility are created by the decay of light mesons, mainly through the following reactions [10]:

$$\pi^{+(-)} \rightarrow \mu^{+(-)} + \nu_\mu(\bar{\nu_\mu}),$$
$$K^{+(-)} \rightarrow \mu^{+(-)} + \nu_\mu(\bar{\nu_\mu}).$$

The mesons are produced from a high-energy and high-intensity proton beam (in this case the 400 GeV/c of the SPS) hitting a target.

Figure 3.6 shows the schematic layout of the CNGS facility on the CERN side. The proton beam hits the target and the mesons travel in a vacuum pipe 1000 meters long to allow them to decay and produce the neutrino beam. A hadron stop absorbs the remaining hadrons and the muons and neutrinos then travels directly in the rock (molasse) where the muons are progressively absorbed. The neutrino beam remains and can travel to Gran Sasso.

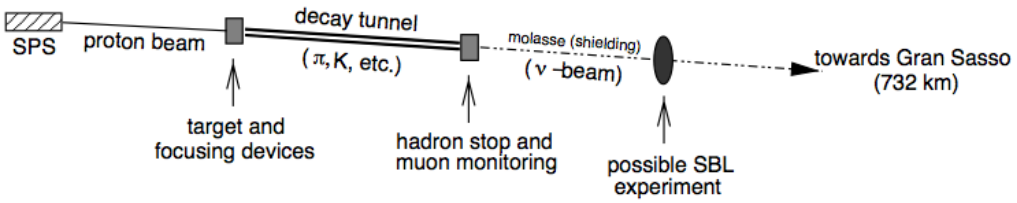

Figure 3.6: Schematic layout of the CNGS facility on the CERN side (from Ref. [10]).

3.2 Specific methods used for the PS to SPS transfer

In addition to the fast extraction described in section 3.1.2, two unique transfer methods have been developed to fill the SPS with a PS beam. These methods are used for the two fixed-target use of the SPS: the CNGS experiment and the experiments of the North Hall.

In both cases the idea is to fill the SPS machine in only two PS cycles. The two methods allow to extract the beam in a few turns (five in the present implementation) thus being methods in between the fast and slow extractions. The SPS is 11 times bigger than the PS and therefore if one extract a PS beam in five turns two injections can fill ten eleventh of the SPS. The remaining empty eleventh portion of the machine allows to accommodate for the rise time of the SPS extraction kicker.

Filling the machine almost completely in only two injections is efficient for the experiments as it allows shorter supercycles. In addition it is preferable to have a machine completely filled before extraction to the experiment as it produces a longer spill.

It should be noted that both methods mainly rely on the horizontal phase space manipulation of the beam and are used to extract beams at 14 GeV/c.

3.2.1 The CT method

To allow such an extraction schema, the CT method was developed in the seventies for the North Hall beams of the SPS.

We describe very briefly this method to allow the reader to understand how the novel MTE presents advantages compared to the CT extraction. References [11, 31, 32] provide more details.

Just before the extraction the fractional tune is set to .25 and the closed-orbit is modified by two dipoles to generate a slow closed bump around the electrostatic septum located in the straight section 31 of the PS. Then a second closed bump around the septum is generated using kicker magnets. Varying the strength of the kickers, a specific portion of the beam jumps the blade of the septum, allowing it to be *shaved* by the septum. The kick given by the electrostatic septum induces an oscillation of the shaved beam that makes it jump over the blade of the extraction magnetic septum located in the straight section 16.

As the tune is set to .25, the beam is extracted as a continuous ribbon over four turns (one complete rotation in phase space at the location of the septum). As the core remains in the machine, it is extracted during the fifth turn by mean of a higher strength of the kicker magnets.

Figure 3.7 schematically summarizes the principle of the CT extraction. The PS ring and the main elements used for the extraction are sketched, and the phase space location of the five extracted beamlets is shown.

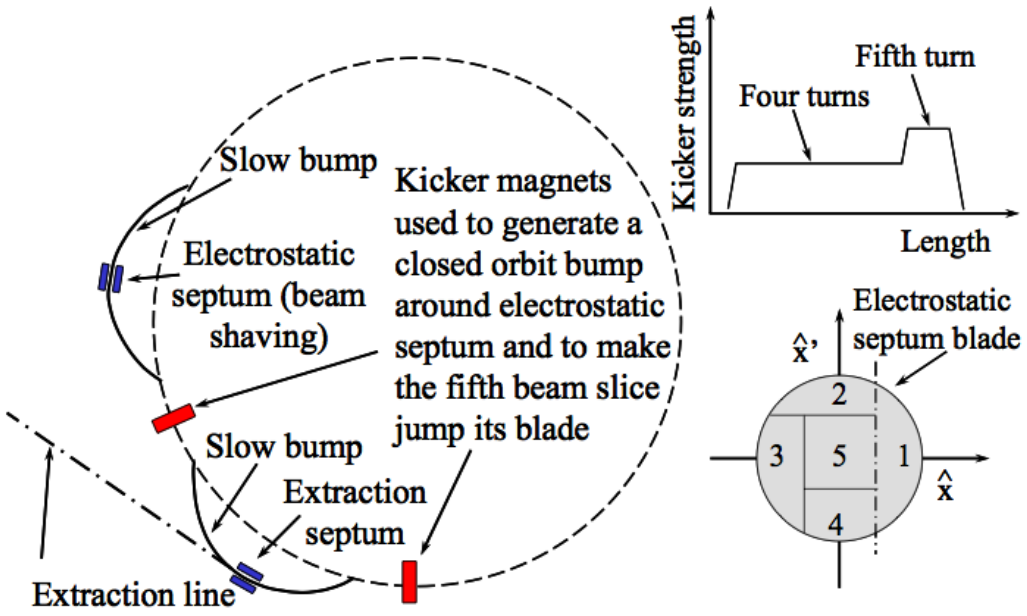

Figure 3.7: Schematic principle of the CT extraction (from Ref. [11]). (left) The PS ring and the main elements used for the extraction; (top right) the strength of the kicker magnets as a function of time and (bottom right) the regions of the shaved beam represented in the horizontal phase space of the beam.

The extracted beam is then five PS turns long. The strength of the kicker magnets is adjusted to shave the beam in five beamlets whose intensities are as equal as possible.

Nonetheless two main disadvantages should be pointed out:

- As the beam is physically moved through the septum beam during the shaving, particles intercept the blade and this produces losses. Even if actions are taken to reduce them (see [11]) these losses are intrinsic to the method;
- there is a mismatch of the optical parameters of the beamlets thus leading to filamentation and emittance blow-up in the SPS.

The method is still in use for North Hall beams and for CNGS beams but in both cases it should be replaced by the MTE extraction method.

3.2.2 The MTE method and its implementation

The new MTE technique was designed after an analysis performed in view of an intensity increase for the CNGS beams to provide beams of intensity bigger than the nominal value of 3.3×10^{13} protons per PS batch [11]. Indeed it was found that among the intensity of 4.5×10^{19} protons per year destined to the neutrino experiment approximately 1.7×10^{19} were lost in the accelerators chain, *i.e.* the losses amounts for 40% of the total intensity [11]. A new extraction

method was then proposed as it was seen that a large part of these losses (40%) were due to the losses occurring at the electrostatic septum blade during the CT extraction from the PS to the SPS.

Therefore a novel extraction method was proposed were the horizontal phase space of the beam is split in five distinct parts by means of nonlinear manipulations. In addition to a reduction in the losses, as the beamlets are created without physical interception of the blade of a septum, this new method, called MTE, is expected to provide beamlets whose optical parameters should better match those of the receiving machine.

The core of the MTE method is to use nonlinear elements (sextupoles and octupoles) to generated stable islands in the horizontal phase space. Indeed the nonlinear dynamics introduced by these elements modify the topology of the phase space, and if the tune is close to a resonant value, stable fixed points and stable islands are created (see section 3.3 for more details). The tune is viewed as an external parameter of the method and its value controls the parameters of the islands (size and position).

The goal is then to trap a fraction of the beam in these islands to obtain at the end of the process separated beamlets. This is the key point of the method: a variation of the horizontal tune in order to cross a resonance (for example close to .25 in the case of the fourth order resonance). If the variation is slow, the adiabaticity of the process is not completely lost and when particles cross the separatrix of the islands can be trapped inside the separatrix of one island.

The beam is then split in a few parts (depending on the number of islands) separated in phase space without the need of any mechanical action [31]. It is also possible to control the stability around the origin: if the nonlinear elements are set in such a way that the resonance is stable, the particles will be trapped in the islands or stay in the central core, but if the resonance is made unstable, then no particle will remain close to the origin.

In the current implementation, the fourth-order (stable) resonance is crossed and the beam is thus split in four islands plus the central core. In addition to this fourth order resonance (required in the actual case of the five turn PS to SPS transfer) other resonances have been tested (second, third and fifth order) [33, 34].

When the particles are trapped in the islands it is also possible to move adiabatically these islands to higher amplitudes to increase the separation between the slices to provide enough room to make the beamlets jump over a septum blade [31]. At the end of the process, the islands and the core are well separated and it is possible to eject each beamlets separately. As the beamlets are separated the blade of the septum will not intercept any particles and it is possible to achieve a multi-turn extraction with reduced losses compared to the CT method [5]

In the fourth order case, as the tune is close to .25, at a given location of the ring, the particles jump from one island to another at each turn and therefore the closed-orbit of a particle with zero amplitude with respect to the fixed points of the islands is four times larger than the circumference of the ring. Two distinct structures are thus present in the machine. On one hand, the dynamics of the core around the origin, whose parameters (optical parameters and tune) are those of the linear machine with the nonlinear perturbation. On the other hand the dynamics of the islands, where the close-orbit is larger and where the optical parameters and tune are modified by the nonlinear resonance.

Figure 3.8 shows the orbits of the four islands along the circumference in the PS.

[5] It should be noted that this process is in principle reversible in time and that it could also be used for *multi-turn injection*. This possibility is analyzed in [28].

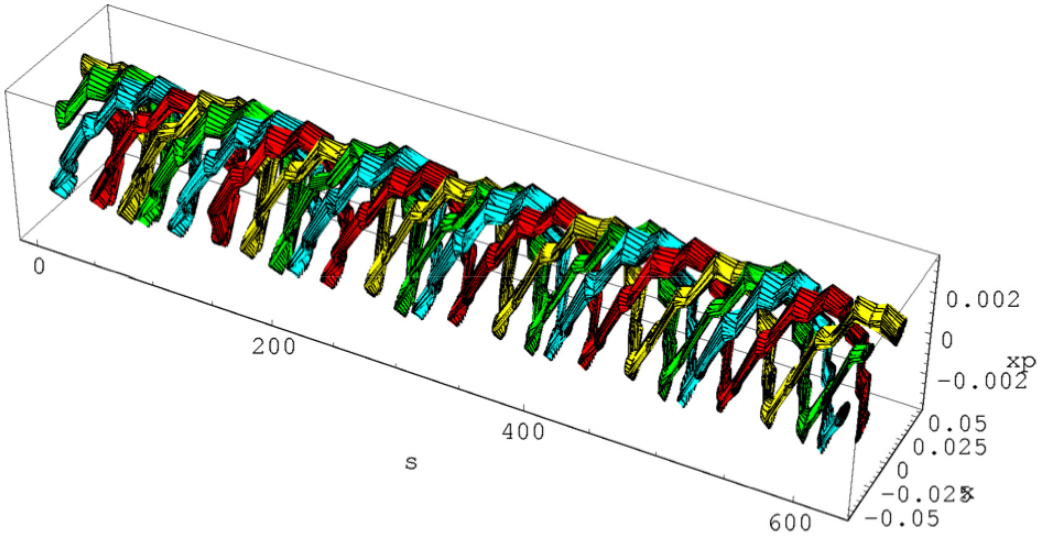

Figure 3.8: 3D representation of the four beamlets along the ring (from Ref. [12]).

More details about the actual implementation of MTE in the PS machine can be found in references [12, 35]. Experimental tests of the method have been performed in 2002 and in 2004, experimental evidences of beam splitting have been observed for different beam intensities [36]. Then other experimental campaigns have been launched and the method has finally been used in operation for CNGS beams in 2010.

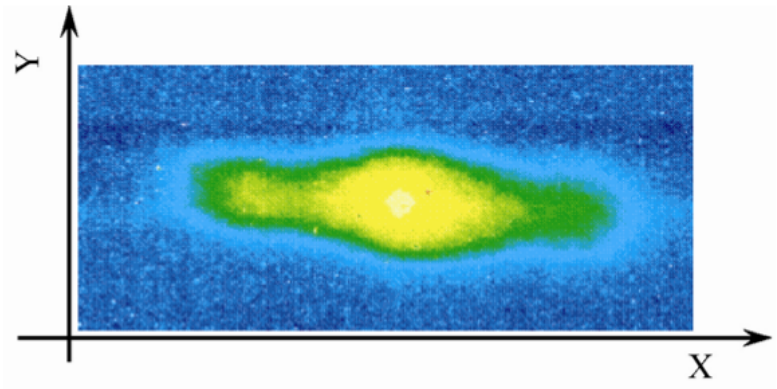

Figure 3.9: Beam distribution in physical space: beam splitting in the PS and observation in the transfer line TT2 (from Ref. [12]).

Figure 3.9 shows the split beam in physical space after a fast ejection of the whole beam (every beamlets during the same turn) in the transfer line. The peculiar beam distribution is clearly observed. In the latter section we shall analyze the properties of the beam in phase space that better exhibit the properties of the islands.

More details about the implementation and the elements used in the PS can be found in [11, 36].

3.3 The modeling of the MTE method and the Hénon mapping

We now focus on the splitting process itself. To do so, we mostly deal with the nonlinear beam manipulation involved in the splitting process of the MTE method. Therefore we will not focus on the extraction proper but rather on the nonlinear dynamics that is involved during the splitting.

3.3.1 Model for the MTE beam splitting

The PS machine is obviously a very complex machine [6] and won't try to model all the specificities.

A simple model has been used since the beginning of the design of the method. It represents a periodic lattice under the influence of sextupole and octupole magnets [31]. This model is first discussed in its 4D formulation, but, as the splitting process mainly involves the horizontal phase space we shall see that we can in many cases use the 2D restriction of the complete model.

The sextupole and octupole effects are both represented in the single kick approximation, and it is assumed that both magnets are at the same location. The model, in the physical coordinates is then the composition of a one-turn Courant-Snyder matrix (equation (2.96)) and a nonlinear kick combining the one of a sextupole (equation (2.125)) and the one of an octupole (equation (2.125)). We thus have $\boldsymbol{x}_{n+1} = \boldsymbol{\mathcal{M}}_n \boldsymbol{x}_n$:

$$\begin{pmatrix} x \\ x' \\ y \\ y' \end{pmatrix}_{n+1} = \boldsymbol{R}(\omega_x, \omega_y) \circ \begin{pmatrix} x \\ x' + K_2(x^2 + y^2) + K_3(x^3 - 3x^2 y) \\ y \\ y' + K_2 xy + K_3(y^3) \end{pmatrix}_n , \tag{3.1}$$

where $\boldsymbol{R}(\omega_x, \omega_y)$ is the generalization to four dimensions of the one turn Courant-Snyder rotation matrix (with no coupling):

$$\begin{pmatrix} \cos\omega_x + \alpha_x \sin\omega_x & \beta_x \sin\omega_x & 0 & 0 \\ -\gamma_x \sin\omega_x & \cos\omega_x - \alpha_x \sin\omega_x & 0 & 0 \\ 0 & 0 & \cos\omega_y + \alpha_y \sin\omega_y & \beta_y \sin\omega_y \\ 0 & 0 & -\gamma_y \sin\omega_y & \cos\omega_y - \alpha_y \sin\omega_y \end{pmatrix} . \tag{3.2}$$

As we want to analyze the mapping using the normal form approach and using a tracking code, it is useful to express it in a set of coordinates where the mapping exhibit its core properties [33]. To do that we first transform this mapping into the Courant-Snyder using the 4D generalization of the conjugation matrix $\boldsymbol{T}$ (equation (2.104)):

$$\boldsymbol{T} = \begin{pmatrix} \sqrt{\beta_x} & 0 & 0 & 0 \\ -\frac{\alpha_x}{\sqrt{\beta_x}} & \frac{1}{\sqrt{\beta_x}} & 0 & 0 \\ 0 & 0 & \sqrt{\beta_y} & 0 \\ 0 & 0 & -\frac{\alpha_y}{\sqrt{\beta_y}} & \frac{1}{\sqrt{\beta_y}} \end{pmatrix} . \tag{3.3}$$

[6] Many aspects of the machine makes it even more complicated if one want to proceed with the "next order" of modeling: it is a combined function machine, the dispersion is non zero everywhere, etc.

We then use the property $\boldsymbol{R}(\omega_x, \omega_y) = \boldsymbol{T}^{-1}\boldsymbol{M}\boldsymbol{T}$ to rewrite the mapping in the Courant-Snyder coordinates ($\hat{\boldsymbol{x}} = \boldsymbol{T}^{-1}\boldsymbol{x}$):

$$\begin{pmatrix} \hat{\boldsymbol{x}} \\ \hat{\boldsymbol{x}}' \\ \hat{\boldsymbol{y}} \\ \hat{\boldsymbol{y}}' \end{pmatrix}_{n+1} = \boldsymbol{R}(\omega_x, \omega_y) \circ \begin{pmatrix} \hat{\boldsymbol{x}} \\ \hat{\boldsymbol{x}}' + \sqrt{\beta_x}\left(\frac{K_2}{2}\beta_x^{3/2}(\hat{\boldsymbol{x}}^2 - \chi\hat{\boldsymbol{y}}^2 + \frac{K_3}{6}\beta_x^2(\hat{\boldsymbol{x}}^3 - 3\chi\hat{\boldsymbol{x}}\hat{\boldsymbol{y}}^2))\right) \\ \hat{\boldsymbol{y}} \\ \hat{\boldsymbol{y}}' + \sqrt{\beta_y}\left(-K_2\beta_x^{3/2}\chi\hat{\boldsymbol{x}}\hat{\boldsymbol{y}} - \frac{K_3}{6}\beta_x^2(\chi^2\hat{\boldsymbol{y}}^3 - 3\chi\hat{\boldsymbol{x}}^2\hat{\boldsymbol{y}})\right) \end{pmatrix}_n, \tag{3.4}$$

where χ is a dimensionless parameter representing the coupling between the two planes: $\chi = \beta_y/\beta_x$.

We can go one step further and make the coefficient of $\hat{\boldsymbol{x}}^2$ equal to one using a nonsymplectic transformation (scaling) to define new dimensionless coordinates $(\hat{\boldsymbol{X}}, \hat{\boldsymbol{X}}', \hat{\boldsymbol{Y}}, \hat{\boldsymbol{Y}}') = \lambda(\hat{\boldsymbol{x}}, \hat{\boldsymbol{x}}', \hat{\boldsymbol{y}}, \hat{\boldsymbol{y}}')$ with $\lambda = \frac{1}{2}K_2\beta_x^{3/2}$ [33].

This produces the mapping

$$\begin{pmatrix} \hat{\boldsymbol{X}} \\ \hat{\boldsymbol{X}}' \\ \hat{\boldsymbol{Y}} \\ \hat{\boldsymbol{Y}}' \end{pmatrix}_{n+1} = \boldsymbol{R}(\omega_x, \omega_y) \circ \begin{pmatrix} \hat{\boldsymbol{X}} \\ \hat{\boldsymbol{X}}' + \hat{\boldsymbol{X}}^2 - \chi\hat{\boldsymbol{Y}}^2 + \kappa\left(\hat{\boldsymbol{X}}^3 - 3\chi\hat{\boldsymbol{X}}\hat{\boldsymbol{Y}}^2\right) \\ \hat{\boldsymbol{Y}} \\ \hat{\boldsymbol{Y}} - 2\chi\hat{\boldsymbol{X}}\hat{\boldsymbol{Y}} - \kappa\left(\chi^2\hat{\boldsymbol{Y}}^3 - 3\chi\hat{\boldsymbol{X}}^2\hat{\boldsymbol{Y}}\right) \end{pmatrix}_n, \tag{3.5}$$

where we defined the parameter κ:

$$\kappa = \frac{2}{3}\frac{K_3}{K_2^2}\frac{1}{\beta_x}. \tag{3.6}$$

This parameter κ represents the normalized ratio between the strength of the octupole and the strength of the sextupoles.

The mapping (3.5) shall be considered as the main model used in your analysis of the splitting process. This mapping depends on four parameters: the horizontal and vertical tunes ($\omega_{x,y} = 2\pi\nu_{x,y}$), the coupling between the two planes (χ) and the strength of the nonlinearities (κ).

As we shall discuss in section 3.3.3, the main point of the method is the time dependence of the horizontal tune. Therefore the mapping is time dependent and its properties and impact on the phase space evolves with the tune.

In some cases we can neglect completely the coupling between the horizontal and the vertical motion, thus considering that, as in the ideal case, the nonlinearities act only on the horizontal plane. The splitting would thus be purely done in that plane, while the dynamics in the vertical plane would stay linear (a pure rotation). In this 2D case the mapping is written as follow:

$$\begin{pmatrix} \hat{\boldsymbol{X}} \\ \hat{\boldsymbol{X}}' \end{pmatrix}_{n+1} = \boldsymbol{R}(\omega_x) \begin{pmatrix} \hat{\boldsymbol{X}} \\ \hat{\boldsymbol{X}}' + \hat{\boldsymbol{X}}^2 + \kappa\hat{\boldsymbol{X}}^3 \end{pmatrix}_n. \tag{3.7}$$

It can easily be proved that these mappings are the Poincaré map of an Hamiltonian derived from the general Hamiltonian of the transverse motion, $\mathcal{H}_5$, given by equation (2.69). If we set the momentum to the reference momentum ($\delta \to 0$) as it the case in our model of the MTE method, we obtain, in the 4D case, the following Hamiltonian [27]:

$$\mathcal{H} = \frac{\tilde{P}_x^2 + \tilde{P}_y^2}{2} + \frac{b_2}{2}(x^2 + y^2) - \left[\frac{K_2}{6}(x^3 - 3xy^2) + \frac{K_3}{24}(x^4 - 6x^2y^2 + y^4)\right]\sum_{n=-\infty}^{+\infty}\delta(s - nl), \tag{3.8}$$

where we also neglected the weak focusing effect of the dipoles: the Hamiltonian is thus the model of a periodic straight FODO cell containing thin sextupoles and octupoles (located at the same position); l is the length of the cell.

3.3.2 The Hénon mapping and its fixed points

The mappings (3.5) and (3.7) are called *generalized Hénon mappings*, in reference to the work of M. Hénon on quadratic area-preserving mappings [37]. In this work he analyses quadratic area-preserving mappings (symplectic condition in 2D) and proves that quadric area-preserving mappings where the origin is an elliptic fixed point can be cast into the form (3.7) (without the cubic term). Therefore the mappings we consider here are generalizations that include a cubic term, and in the case of (3.5) that are generalized to four dimensions (still satisfying the symplectic condition). The properties of the Hénon mapping have been studied extensively as it is the "simplest nontrivial symplectic polynomial map" [27].

The properties of the MTE method depends on those of these mappings. Therefore we discuss here the properties of the Hénon mapping, in particular its fixed points. In this context, we also introduce the notion of *resonant frequency* [7].

Resonant frequencies

We introduce here the notion of resonant frequency in the 2D case. A generalization to the 4D case can be found in Ref. [27].

The linear part of a 2D symplectic mapping can be cast in the form of a rotation generated by $e^{i\omega}$ (see equation (2.113)). If we consider the symmetry group $\mathcal{G}_\omega$ generated by $e^{i\omega}$, the following theorem can be proved (from Ref. [27]):

Theorem 1. *The elements of the group $\mathcal{G}_\omega$ are the transformations $\zeta \to e^{in\omega}\zeta$ ($\zeta \in \mathcal{C}$). The group $\mathcal{G}_\omega$ is then equivalent to the group of translations on the 1D torus [8]. If $\omega/2\pi$ is irrational then the orbit of the group is dense on the torus. If $\omega/2\pi$ is a rational number p/q then the orbit on the torus is a closed set and consists of q elements (p and q are integers with no common divisor).*

It follows that the orbit, generated by the mapping, of a particle can return to its initial point after a finite number of turns k, or never come back to it [27]. We formally define this if we consider the coordinate of the orbit on the torus. We denote it as $\phi^{(k)} = \left(\phi^{(0)} + k\omega\right) \mod 2\pi$. The condition for the orbit to come back to the same point after k turns then reads $\phi^{(k)} = \phi^{(0)}$ and we have the condition

$$\omega k - 2\pi j = 0, \tag{3.9}$$

where j is the integer part of $k\omega/2\pi$ [27].

This condition can be written in the compact form $\tilde{\boldsymbol{\omega}} \cdot \boldsymbol{k} = 0$ if we define

$$\tilde{\boldsymbol{\omega}} = (\omega, 2\pi), \text{ and} \tag{3.10}$$

$$\boldsymbol{k} = (k, -j). \tag{3.11}$$

[7] In beam dynamics the concept of nonlinear resonance is omnipresent and is discussed following different approaches in references [3, 14, 21, 26, 38]. Although the concepts are the same, the approaches differ and some aspects might be confusing. Here we follow the very general approach of [27] to introduce the concept of resonance from the properties of the frequencies of the mapping (3.7).

[8] We define the 1D torus as the interval $[0, 2\pi]$ whose ends are identified.

Based on these definitions we can therefore distinguish two cases depending on the frequency of the mapping [27]:

Nonresonant case The frequency ω is nonresonant when

$$\tilde{\boldsymbol{\omega}} \cdot \boldsymbol{k} = 0 \text{ if and only if } \boldsymbol{k} = 0. \tag{3.12}$$

This condition is satisfied if $\omega/2\pi$ is irrational.

Resonant case The frequency ω is resonant when

$$\tilde{\boldsymbol{\omega}} \cdot \boldsymbol{k} = 0 \text{ if and only if } \boldsymbol{k} = l(q, -p), \tag{3.13}$$

where q and p are two integers with no common divisor and l is an arbitrary integer [27]. This condition is obtained if $\omega/2\pi = p/q$ is rational.

Therefore, in the resonant case, the orbit will be periodic and consists only of q points on the torus.

The MTE method use the fourth order resonant, *i.e.* the horizontal tune is set to $\nu_x = p/q = 1/4$.

Properties of the fixed points of the mapping

The qualitative behavior of a map $\boldsymbol{\mathcal{F}}$ is indeed given by the fixed points [27].

Definition 3. $\left(\hat{\boldsymbol{X}}, \hat{\boldsymbol{P}}\right)$ is a fixed point of order m of the map $\boldsymbol{\mathcal{F}}$ if

$$\boldsymbol{\mathcal{F}}^{\circ m}\left(\hat{\boldsymbol{X}}, \hat{\boldsymbol{P}}\right) = \left(\hat{\boldsymbol{X}}, \hat{\boldsymbol{P}}\right), \tag{3.14}$$

where $^{\circ m}$ denotes the mth iteration of the map.

The properties of a fixed point of order m depend on the linearization of the mth iteration of the map in the neighborhood of the fixed point [27]. In the case of a 2D mapping, we follow [27] and we write

$$\begin{pmatrix} \hat{\boldsymbol{X}}' \\ \hat{\boldsymbol{P}_{\boldsymbol{X}}}' \end{pmatrix} = \begin{pmatrix} \hat{\boldsymbol{X}}_0 \\ \hat{\boldsymbol{P}}_{\boldsymbol{X}0} \end{pmatrix} + \boldsymbol{A} \begin{pmatrix} \hat{\boldsymbol{X}} - \hat{\boldsymbol{X}}_{\boldsymbol{0}} \\ \hat{\boldsymbol{P}_{\boldsymbol{X}}} - \hat{\boldsymbol{P}_{\boldsymbol{X0}}} \end{pmatrix} + \mathcal{O}\left((\hat{\boldsymbol{X}} - \hat{\boldsymbol{X}_{\boldsymbol{0}}})^2 + (\hat{\boldsymbol{P}_{\boldsymbol{X}}} - \hat{\boldsymbol{P}_{\boldsymbol{X0}}})^2\right), \tag{3.15}$$

where $\boldsymbol{A}$ is the Jacobian matrix of $\boldsymbol{\mathcal{F}}$ computed at the fixed point $(\hat{\boldsymbol{X}_{\boldsymbol{0}}}, \hat{\boldsymbol{P}_{\boldsymbol{X0}}})$. As we consider a symplectic mapping, the determinant of the matrix $\boldsymbol{A}$ is equal to one and its eigenvalues follows the classification given in (2.112).

Analytical expressions can be found for the fixed points of various orders in the case of the Hénon mapping [37]. The position of the fixed points can also be found numerically. Figure 3.10 displays the phase portrait of the Hénon mapping for different tunes. For tunes close to a resonant value one can observe that the fixed points of the corresponding order close to the origin. We observe that both elliptic and hyperbolic fixed points are present and As we shall see, a chain of islands arise from the alternation of these elliptic and hyperbolic fixed points.

First we define formally the notion of stable fixed point:

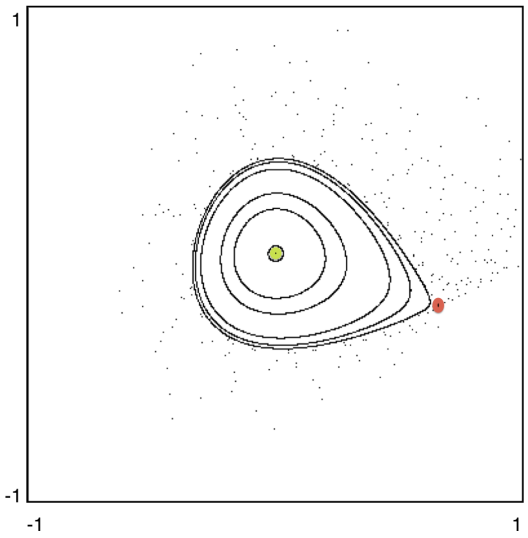

(a) $\nu = 0.101$.

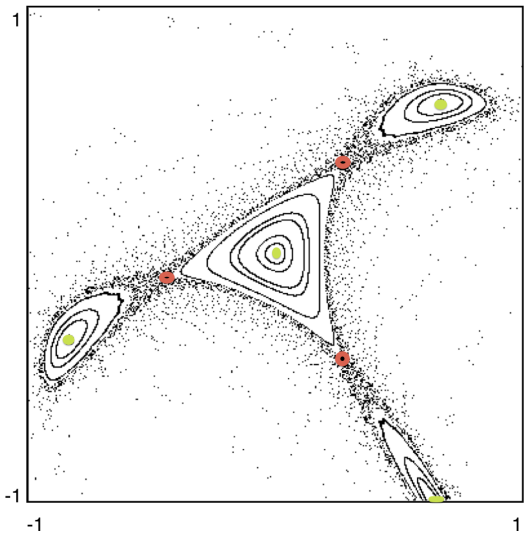

(b) $\nu = 0.32$. Islands of the third order resonance.

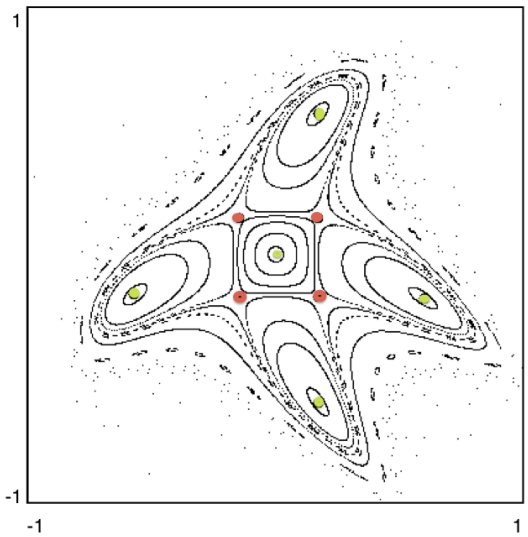

(c) $\nu = 0.252$.

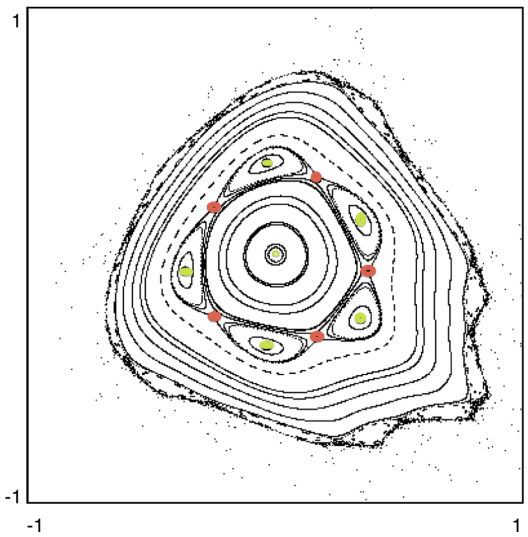

(d) $\nu = 0.205$.

Figure 3.10: Phase space topology of the quadratic Hénon mapping. Green dots are the elliptic fixed points and red dots are the hyperbolic ones (obtained with GIOTTO [13].)

Definition 4. "A fixed is stable if there are closed invariant curves in any neighborhood of it" [27].

It follows that in the linear case, elliptic fixed points will be stable while hyperbolic fixed points will be unstable. On the other hand, the nonlinear term might not preserve the topological structure of the linear orbits in the vicinity of the fixed pint. One can thus have unstable elliptic fixed points [27]. Such an analysis can be done using the normal form approach.

We now introduce a theorem that is of major importance regarding our analysis of the Hénon mapping: indeed it explains the breaking mechanism of the orbits around the elliptic fixed points into islands. This is the Poincaré-Birkhoff theorem [27]. Following that theorem, if $\boldsymbol{\mathcal{F}}$ is a mapping in the form of an amplitude dependant rotation, and if we add a perturbation to obtain a map $\boldsymbol{\mathcal{F}}_\epsilon$, then $\boldsymbol{\mathcal{F}}_\epsilon^{(\circ q)}$ will possess q elliptic fixed points and q hyperbolic fixed points due to the deformation of the invariant curves. In addition, the topology of the phase space close to the elliptic fixed points is modified and islands are created by the breaking of the invariant curves.

This theorem applies directly to the Hénon mapping as it is possible to conjugate the mapping to an amplitude dependant rotation to which a perturbation is added (see chapter 4).

3.3.3 Overview of the trapping process

We can now understand the trapping process of the MTE method.

We view the mapping as an amplitude dependant rotation plus a perturbation term. For amplitudes where the frequency is resonant we know that the invariant curves will break and will give elliptic and hyperbolic fixed points. Around the stable elliptic fixed points we then have stable islands. If we vary the linear tune of the mapping we change the position of these fixed points and islands. Depending on the value of κ, the sign of the amplitude dependence can be different.

We consider in this explanation that κ is set such that the frequency increases with the amplitude. Our goal is to trap the particles in the islands created by the fourth-order resonance. Therefore if we start with a tune above the resonant frequency, no island will be present. The process thus consists in a variation of the tune, lowering its value to cross the resonant frequency. At that point the fixed points and the islands appear and they start to grow as the tune decreases. In addition, as the tune goes further from the resonant frequency, the islands move to higher amplitude [9].

Figure 3.11 displays this process using phase space plots obtained with GIOTTO [**?**] and the resulting trapping obtained from numerical simulations (see chapter 5). These 2D simulations were performed using a Gaussian beam distribution and the parameter κ was set to -1.1. The tune evolved linearly from 0.252 to 0.245 and three steps are displayed. The first one is at resonant tune, the islands are not present but we observe the effect of the mapping in the peculiar topology of the phase space. The second step is displayed at $\nu_x = 0.249$ and we observe the islands and the beginning of the trapping. The final step at $\nu_x = 0.245$ shows the phase space situation at the end of the trapping; the islands are well separated from the core.

[9] Indeed, for a given detuning with amplitude, the amplitude where the tune reach its resonant value has to be higher.

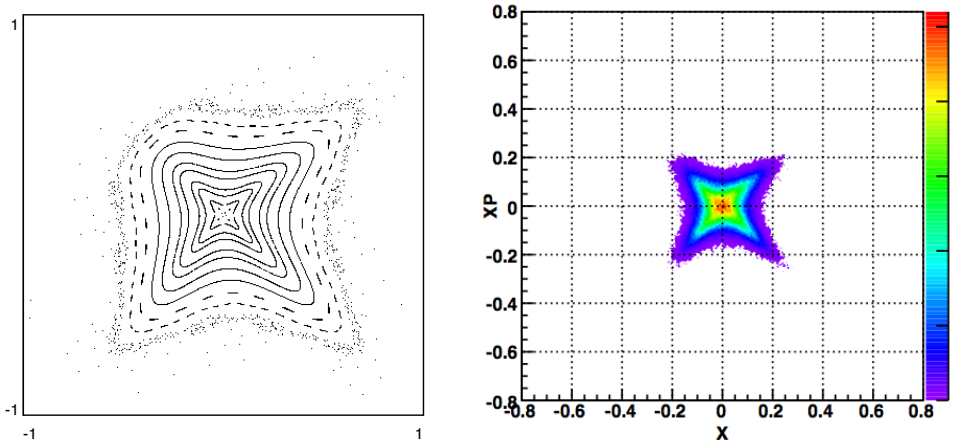

(a) $\nu = 0.250$. (b) $\nu = 0.250$.

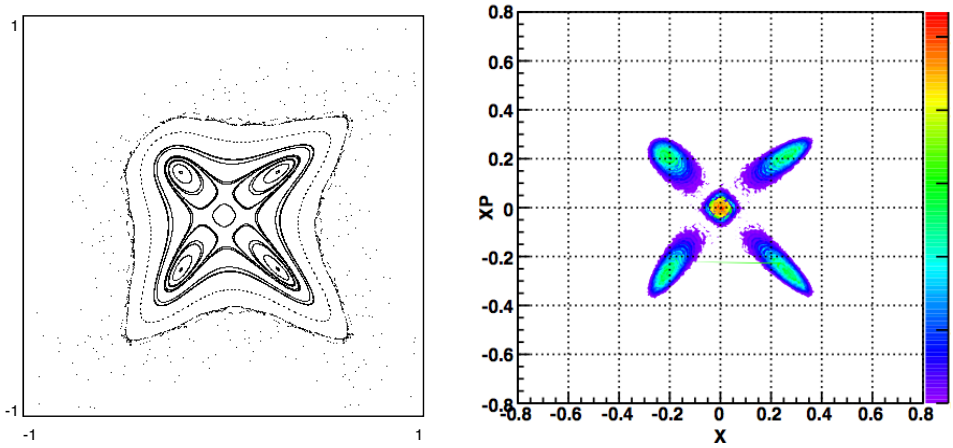

(c) $\nu = 0.249$. (d) $\nu = 0.249$.

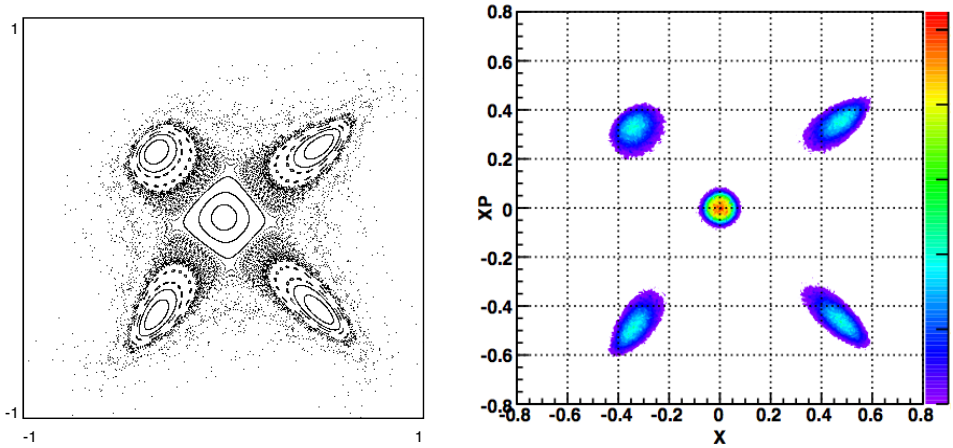

(e) $\nu = 0.245$. (f) $\nu = 0.245$.

Figure 3.11: Phase space evolution during the trapping process. (left) Topology obtained with GIOTTO. (right) Numerical trapping simulation performed with Manzoni (see chapter 5).

Chapter 4

Analytical study of MTE: a Normal Form approach

This chapter uses the Normal Form approach to analyze the properties of the Hénon mapping describing the MTE process. First we define the Normal Forms in section 4.1 and then, in section 4.2, we construct explicitly the quasi-resonant normal form for the fourth order resonance of the Hénon mapping. This first part allows to understand in more details the relations between the islands and the resonant or nonresonant properties of the mapping. Next, in section 4.3, we construct a Hamiltonian interpolating the normal form map. It allows a more quantitative analysis of the properties of the islands. Nevertheless, we show that at the lowest perturbation order this approach fails to provide quantitative results in the fourth order case. In section 4.4 we conclude with a first attempt to use a model providing analytical estimates of the trapping probabilities.

4.1 Normal forms: definition and construction . . . 52
4.1.1 Definition of the normal forms . . . 53
4.1.2 Construction of normal forms for 2D maps . . . 55
4.2 The quasi-resonant normal form of the Hénon map . . . 56
4.2.1 Explicit construction . . . 56
4.2.2 The quasi-resonant Normal Form . . . 58
4.3 Interpolating Hamiltonian of the Hénon map from normal form analysis . . . 58
4.3.1 Definition of the interpolating Hamiltonian . . . 58
4.3.2 Analysis of the fourth order resonance . . . 61
4.4 Analytical model of the trapping probability for MTE . . . 63

4.1 Normal forms: definition and construction

The normal forms method allows to analyze the properties of nonlinear maps. We first discuss the definition and formal construction of the normal forms in the two-dimensional case and

then in the next section we shall apply this method to the analysis of the generalized Hénon mapping (equation (3.7)) modeling the MTE process. Our main reference is [27] written by the *Bologna group* which worked on the theory of normal forms for nonlinear transfer maps applied to problems related to nonlinear beam dynamics in a collaboration with CERN.

Normal forms are analytical tools providing theoretical understanding of the dynamics in addition to quantitative results [27] it is thus a very good complement to the analysis of a map done through numerical simulations with a tracking code. Moreover, it is proved [27] that normal forms are reliable when the motion is not highly perturbed, as it is the case for accelerator applications.

The description of an accelerator can be done either using Hamiltonian flow or using the discrete formalism of the transfer maps. In that view, the normal forms are the generalization of the classical Hamiltonian perturbative theory to nonlinear transfer maps [27]. The goal of the method is to make the symmetry properties explicit through a change of coordinates; in particular the symmetries of the linear part of the transfer map. This method is in our case preferred to the perturbation theory working directly on the Hamiltonian as we work in a model with discrete nonlinear elements thus nicely described in the transfer map formalism under the kick approximation.

We have already discussed in section 2.3.3 the Courant-Snyder theory, where the linear transfer matrix is conjugated to a pure rotation matrix. This rotation matrix is said to be the linear transfer map put in its linear normal form representation. This transformation exhibit clearly the symmetry of the linear motion (rotations) and the invariants of the motion: the radii of the circles are simply the invariants [27].

In the nonlinear case the problem is more striking due to the presence of resonant frequencies. In the nonresonant case, the normal form transformation allow to find new coordinates where the map is again a simple rotation but where the tune depends on the amplitude (rotation with amplitude dependent frequency). The effect is thus similar to the linear one: the orbit in phase space are transformed from a closed curve (ellipses in the linear case) into a family of circles [27]. The problem is that not all the orbits of the nonlinear map are closed-curve, as we discussed in section 3.3.2. If one gets closer to a resonance then these closed-curve will be closer to the origin and will be a problem as we are mainly interested in the dynamics in a region surrounding the origin. However we shall se that it is possible to include these resonances into the normal form. This feature is unique to the nonlinear case.

In the following we restrict our discussion to the theory for 2D transfer maps. Generalizations to the four-dimensional case can be found in [27].

4.1.1 Definition of the normal forms

We consider a general nonlinear transfer map $\boldsymbol{\mathcal{F}}$ expressed in the complex Courant-Snyder coordinates (see section 2.3.4). The transfer map is conjugated to its normal form $\boldsymbol{\mathcal{U}}$ using the conjugating functions $\boldsymbol{\Phi}$. The conjugation equation can be represented by the commutation diagram of equation (4.1).

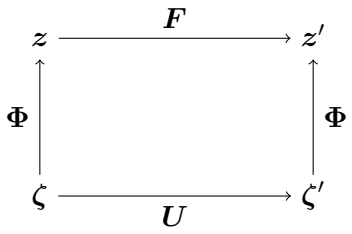

(4.1)

This is equivalent to the transformation of the linear transfer matrix into its diagonal form but in the nonlinear case, $\boldsymbol{\mathcal{F}}$, $\boldsymbol{\mathcal{U}}$ and $\boldsymbol{\Phi}$ are nonlinear maps.

The normal form and the conjugating function thus satisfy the functional equation [27]

$$\boldsymbol{\Phi}^{-1} \circ \boldsymbol{\mathcal{F}} \circ \boldsymbol{\Phi}\left(\boldsymbol{\zeta}\right) = \boldsymbol{\mathcal{U}}\left(\boldsymbol{\zeta}\right). \tag{4.2}$$

The new coordinates are $\boldsymbol{\zeta} = (\zeta, \zeta^*)$.

As the linear part $*$ of the map $\boldsymbol{\mathcal{F}}$ is already diagonalized by the Courant-Snyder transformation, the conjugating function is tangent to the identity and is written as

$$\boldsymbol{z} = \boldsymbol{\Phi}(\boldsymbol{\zeta}) = \boldsymbol{\zeta} + \sum_{n\geq 2} \left[\Phi\right]_n (\boldsymbol{\zeta}), \tag{4.3}$$

where $\left[\Phi\right]_n$ is an homogenous polynomial of order n, a polynomial containing only monomials of order n:

$$\left[\Phi\right]_n = \sum_{n_1+m_1=n} \phi_{n_1,m_1} \zeta^{n_1} \zeta^{*n_1}, \tag{4.4}$$

with ϕ_{n_1,m_1} being a vector of $\mathcal{C}^2$.

The map $\boldsymbol{\mathcal{U}}$ has the same linear part as $\boldsymbol{\mathcal{F}}$ and by definition is invariant under a group of transformations. Quoting Ref. [27], we have the important property: "This symmetry condition implies that the polynomial expansion of $\boldsymbol{\mathcal{U}}$ contains only some monomials". We thus write

$$\boldsymbol{\zeta}' = \boldsymbol{\mathcal{U}}(\boldsymbol{\zeta}) = \Lambda\boldsymbol{\zeta} + \sum_{n\geq 2} \left[\boldsymbol{\mathcal{U}}\right]_n (\boldsymbol{\zeta}), \tag{4.5}$$

$$\left[\boldsymbol{\mathcal{U}}\right]_n = \sum_{n_1+m_1=n}^{*} \boldsymbol{u}_{n_1,m_1} \zeta^{n_1} \zeta^{*m_1}, \tag{4.6}$$

where $\boldsymbol{u}_{n_1,m_1}$ is a vector of $\mathcal{C}^4$ and the * denotes the fact that the sum only contains some monomials.

In the next section we shall detail what are these monomials, in function of the symmetry group upon which the normal form is built. In addition, normal forms can be built for maps whose linear part is hyperbolic or elliptic. We are only concerned with the elliptic case, details regarding the hyperbolic case can be found in [27].

The problems of the existence of a formal solution and analytic solutions are discussed in [27]. Here we use the fact, proved in [27], that "it is always possible to formally build a normal form $\boldsymbol{\mathcal{U}}$ with respect to the symmetry group generated by the linear part of the map Λ, or with respect to a subgroup of it".

4.1.2 Construction of normal forms for 2D maps

Now we construct the polynomial expansion of the normal form according to its symmetry group. A map $\boldsymbol{\mathcal{U}}$ is said to be in normal form with respect to $\mathcal{G}_\omega$ if it commutes with it. Equivalently, it has to commute with the generator of the group. As we consider the rotation group of the linear part of $\boldsymbol{\mathcal{F}}$, we write

$$\boldsymbol{\mathcal{U}}(e^{i\omega}\zeta, e^{-i\omega}\zeta^*) = e^{i\omega}\boldsymbol{\mathcal{U}}(\zeta,\zeta^*), \tag{4.7}$$

where we omit the complex conjugate equation.

As we build the map by expanding it in Taylor serie, the condition has to be valid for each monomials present in the expansion. The condition is then written as

$$e^{i\omega(n-m)}\zeta^n\zeta^{*m} = e^{i\omega}\zeta^n\zeta^{*m}, \tag{4.8}$$

or, if we use the vector notation of section 3.3.2, it can be written as

$$\tilde{\boldsymbol{\omega}}\cdot\boldsymbol{k} = 0, \text{ with } \boldsymbol{k} = (n-m-1,-j). \tag{4.9}$$

We now have to distinguish two cases, depending on the frequency of the rotation symmetry group. In section 3.3.2, we classified the frequencies as either *resonant* or *nonresonant*. The resonant or nonresonant conditions have an impact on the condition (4.9) and we thus define the *nonresonant elliptic normal form* and the *resonant elliptic normal form*. As we shall see one can also define a *quasi-resonant elliptic normal form* [1].

Nonresonant elliptic normal forms

If $\omega/2\pi$ is irrational, then the nonresonance condition is satisfied and thus given that $\boldsymbol{k} = 0$, the only monomials present in the Taylor expansion of the normal form must have $n = m+1$. Therefore we write the nonresonant elliptic normal form as

$$U(\zeta,\zeta^*) = u(\zeta\zeta^*)\zeta. \tag{4.10}$$

Due to the symplectic condition it can be proved that this can be cast into the following form [27]:

$$U(\zeta,\zeta^*) = e^{i\Omega(\zeta,\zeta^*)}\zeta, \tag{4.11}$$

where Ω is a real function of $\zeta\zeta^* = \rho = |\zeta|^2$.

The nonresonant normal form is thus an amplitude dependent rotation symmetric under all rotations. The nonlinear frequency is given by Ω.

Resonant elliptic normal form

If $\omega/2\pi$ is rational then the resonance condition (3.13) is satisfied and the monomials must have $n = m+1+lq$ where l can be positive or negative [27].

Choosing l positive we obtain the conditions $n = m+1+lq$ for $l \geq 0$ and $m = n+lq-1$ for $l \geq 1$. Therefore the resonant normal form reads

$$U(\zeta,\zeta^*) = \sum_{n=0}^{\infty}(\zeta,\zeta^*)^n\left[\sum_{l=0}^{\infty}u_{n,l}^{(+)}\zeta^{ql+1} + \sum_{l=1}^{\infty}u_{n,l}^{(-)}\zeta^{*ql-1}\right], \tag{4.12}$$

where $u_{n,l}^{(+)}$ and $u_{n,l}^{(-)}$ are complex coefficients.

The normal form $\boldsymbol{\mathcal{U}}$ commutes with the subgroup of rotations by an angle $2\pi/q$.

[1] To simplify the notations we now use plain capitals to refer to the maps U, F and Φ.

Quasi-resonant elliptic normal form

So far we built the normal form with respect to the group generated by the linear part of the map, the normal form thus having the same symmetries as the linear part [27].

It is also possible to build a normal form with respect to a group having less symmetries than the linear part of the mapping. This is interesting if it allows to obtain *in fine* a map $\boldsymbol{\mathcal{U}}$ which exhibit more symmetries of the map $\boldsymbol{\mathcal{F}}$ than if it was constructed using the symmetries of the linear part. We shall make this statement more explicit in section 4.2.

A quasiresonant normal form is therefore constructed when ω is nonresonant but is close to a resonance, *i.e.* $\omega = \alpha + \epsilon$, where $\alpha = 2\pi p/q$ and $|\epsilon| \ll |\omega|$. To do so we compute the normal form with respect to the group $\mathcal{G}_\alpha$.

In the next section we shall construct the quasiresonant normal form of the generalized Hénon mapping.

4.2 The quasi-resonant normal form of the Hénon map

4.2.1 Explicit construction

Using the transformation of equation (2.114), the generalized 2D Hénon mapping can be cast into the complex form

$$z' = \boldsymbol{\mathcal{F}}(z, z^*) = e^{i\omega}\left(z - \frac{i}{4}(z+z^*)^2 - \kappa\frac{i}{8}(z+z^*)^3\right) \equiv e^{i\omega}z + \hat{F}(z, z^*). \tag{4.13}$$

$\boldsymbol{\mathcal{F}}$ is written in serie as

$$z' = e^{i\omega}z + \sum_{n\geq 2}\sum_{k=0}^{n} f_{k,n-k} z^k z^{*n-k}, \tag{4.14}$$

where the non zero coefficients of order greater than one are $f_{2,0} = f_{0,2} = -\frac{i}{4}e^{i\omega}$, $f_{1,1} = 2f_{2,0}$, $f_{3,0} = f_{0,3} = -\kappa\frac{i}{8}e^{i\omega}$, and $f_{2,1} = f_{1,2} = -\kappa\frac{3i}{8}e^{i\omega}$.

We compute here the normal form of this mapping in the quasi-resonant case, *i.e.* for a frequency $\omega/2\pi$ close to the fourth order resonance ($p/q = 1/4$).

According to the conditions of equation (4.12), the Taylor expansion of the normal form takes the form

$$U(\zeta, \zeta^*) = e^{i\omega}\zeta + u_{2,1}\zeta^2\zeta^* + u_{0,3}\zeta^{*3} \tag{4.15}$$

where $u_{2,1}$ is the coefficient of the nonresonant term and $u_{0,3}$ is the coefficient of the resonant term. We truncated the serie to the third order, as it is the lowest order that comprises the resonant term.

The conjugating function is given be

$$z = \Phi(\zeta, \zeta^*) = \sum_{n\geq 1}[\Phi]_n(\zeta, \zeta^*) = \zeta + \sum_{n\geq 2}\sum_{k=0}^{n}\phi_{k,n-k}\zeta^k\zeta^{*n-k}. \tag{4.16}$$

To compute the coefficients, we use the functional equation

$$F \circ \Phi = \Phi \circ U \tag{4.17}$$

that we project at order 2 and 3.

Computation of the second order

We have

$$[F \circ \Phi]_2 (\zeta, \zeta^*) = e^{i\omega} \left(\phi_{2,0}\zeta^2 + \phi_{1,1}\zeta\zeta^* + \phi_{0,2}\zeta^{*2} \right) + f_{2,0}\zeta^2 + f_{1,1}\zeta\zeta^* + f_{0,2}\zeta^{*2} \tag{4.18}$$

and

$$[\Phi \circ U]_2 (\zeta, \zeta^*) = e^{2i\omega}\phi_{2,0}\zeta^2 + \phi_{1,1}\zeta\zeta^* + e^{-2i\omega}\phi_{0,2}\zeta^{*2}, \tag{4.19}$$

because the second order coefficients of the normal form are zero (from equation (4.15)).

Extracting the coefficients and using the relation $\left(e^{ik\omega} - 1\right)^{-1} = -\frac{1}{2} - \frac{i}{2}\cot\frac{k\omega}{2}$, we obtain

$$\begin{cases} \phi_{2,0} = \frac{1}{8}\left[-\cot\frac{\omega}{2} + i\right] \\ \phi_{1,1} = \frac{1}{4}\left[\cot\frac{\omega}{2} + i\right] \\ \phi_{0,2} = \frac{1}{8}\left[\cot\frac{3\omega}{2} + i\right]. \end{cases} \tag{4.20}$$

Computation of the third order

We first compute the left hand side of equation (4.17) and we extract each coefficients:

$$\begin{cases} \zeta^3 & : & \phi^*_{2,0}f_{1,1} + f_{3,0} + 2f_{2,0}\phi_{2,0} + e^{i\omega}\phi_{3,0} \\ \zeta^2\zeta^* & : & 2\phi^*_{0,2}f_{0,2} + \phi^*_{1,1}f_{1,1} + f_{2,1} + 2f_{2,0}\phi_{1,1} + f_{1,1}\phi_{2,0} + e^{i\omega}\phi_{2,1} \\ \zeta\zeta^{*2} & : & 2\phi^*_{1,1}f_{0,2} + \phi 2,0^* f_{1,1} + f_{1,2} + 2f_{2,0}\phi_{0,2} + f_{1,1}\phi_{1,1} + e^{i\omega}\phi_{1,2} \\ \zeta^{*3} & : & 2\phi^*_{2,0}f_{0,2} + f_{0,3} + f_{1,1}\phi_{0,2} + e^{i\omega}\phi_{0,3}. \end{cases} \tag{4.21}$$

We proceed the same way for the right hand side of (4.17)

$$\begin{cases} \zeta^3 & : & e^{3i\omega}\phi_{3,0} \\ \zeta^2\zeta^* & : & e^{-2i\omega}\left(e^{2i\omega u_{2,1}+e^{3i\omega}\phi_{2,1}}\right) \\ \zeta\zeta^{*2} & : & e^{-i\omega}\phi_{1,2} \\ \zeta^{*3} & : & u_{0,3} + e^{-3i\omega}\phi_{0,3}. \end{cases} \tag{4.22}$$

At this point both $\phi_{2,1}$ and $\phi_{0,3}$ are still undetermined and we need an additional equation to be able to determine them.

It can be proved that in the resonant case (or quasi-resonant), one must force Φ to be symplectic in order to have a symplectic normal form [27]. Therefore we use the symplectic condition applied to the conjugating function Φ:

$$\frac{\partial\Phi}{\partial\zeta}\frac{\partial\Phi^*}{\partial\zeta^*} - \frac{\partial\Phi^*}{\partial\zeta}\frac{\partial\Phi}{\partial\zeta^*} = 1. \tag{4.23}$$

Separating the nonlinear part $\hat{\Phi}$ we obtain

$$\frac{\partial\hat{\Phi}}{\partial\zeta} + \frac{\partial\hat{\Phi}^*}{\partial\zeta^*} = \frac{\partial\hat{\Phi}^*}{\partial\zeta}\frac{\partial\hat{\Phi}}{\partial\zeta^*} - \frac{\partial\hat{\Phi}}{\partial\zeta}\frac{\partial\hat{\Phi}^*}{\partial\zeta^*}. \tag{4.24}$$

We apply that constraint on the Taylor expansion of Φ and solving the subsequent system we obtain finally

$$\begin{cases} \phi_{3,0} = \frac{i\left(-2\kappa+\cot\frac{\omega}{2}-\cot\frac{3\omega}{2}\right)}{16(-1+e^{2i\omega})} \\ \phi_{2,1} = \frac{1}{64}\left(-\cot^2\frac{\omega}{2} + \cot^2\frac{3\omega}{2}\right) \\ \phi_{1,2} = -\frac{i\left(6\kappa+3\cot\frac{\omega}{2}+\cot\frac{3\omega}{2}\right)}{16(-1+e^{-2i\omega})} \\ \phi_{0,3} = 0. \end{cases} \tag{4.25}$$

Simplifying the expressions and reordering them, we also obtain the coefficients of the normal form:

$$\begin{cases} u_{0,3} = \frac{i}{16} e^{i\omega} \left(\cot \frac{\omega}{2} - \cot \frac{3\omega}{2} - 2\kappa \right) \\ u_{2,1} = -\frac{1}{16} i e^{i\omega} \left(6\kappa + 3 \cot \frac{\omega}{2} + \cot \frac{3\omega}{2} \right). \end{cases} \tag{4.26}$$

We therefore obtained all the coefficients of the normal form U and of the conjugating function Φ, up to the third order.

These coefficients were checked numerically using the code GIOTTO; we verified their validity using the module of GIOTTO allowing to numerically computed the coefficients of the normal form and of the conjugating function.

4.2.2 The quasi-resonant Normal Form

We introduced the normal forms explaining that they exhibit the symmetry properties of the mapping. In our case, we build the quasi-resonant normal form for the fourth order resonance. We therefore expect the normal form to displays clearly the peculiarities of the fourth order resonance.

Indeed, the normal form that we obtained contains a nonresonant part (an amplitude dependent rotation) and a resonant part that allows the representation in the normal form of the breaking of invariant curves into islands [2].

Figures 4.1 and 4.2 show the phase space topology of the Hénon mapping and of the associated normal form. They are generated with GIOTTO using the expansion of the Taylor series up to the fifth order.

Figures 4.1 (a) and 4.2 (a) are the original Hénon mapping (with no cubic term) for frequencies close to the resonant value 0.25. We observe the presence of the islands. We then clearly observe on figures Figures 4.1 (b) and 4.2 (b) that the phase space topology of the Normal Form exhibit the symmetries of fourth order resonance of the mapping. The invariant curves not affected by the resonance (away from the islands) become circles (the frequency being dependent on the amplitude) and the resonant term of the Normal Form allows to reproduce the islands. Figures 4.1 (c) and 4.2 (c) display the Normal Form conjugated back into the origin mapping ($F = \Phi^{-1} U \Phi$).

4.3 Interpolating Hamiltonian of the Hénon map from normal form analysis

4.3.1 Definition of the interpolating Hamiltonian

The truncated normal form of the symplectic mapping is a symplectic truncation: therefore it is not exactly symplectic and it is not suited for tracking [27]. Indeed, from a 2D point a view, this means that the normal form mapping is not area preserving.

Nevertheless, it is possible ton construct an interpolating Hamiltonian to recover the symplecticity [27]. This Hamiltonian interpolates the normal form mapping. Complete derivations can be found in Ref. [27]. Here we use these developments to write the Hamiltonian interpolating the quasi-resonant normal form. As we are in a quasi-resonant case, we denote the distance

[2] To allow a comparison between the quasi-resonant case and the nonresonant case, we provide the coefficients obtained in the nonresonant case in section A.2.

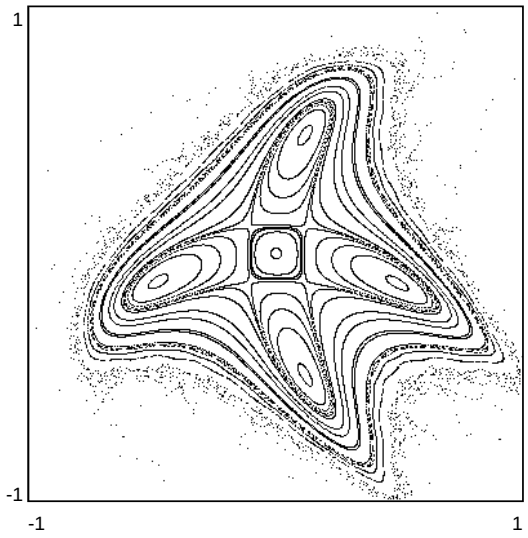

(a) Hénon mapping F

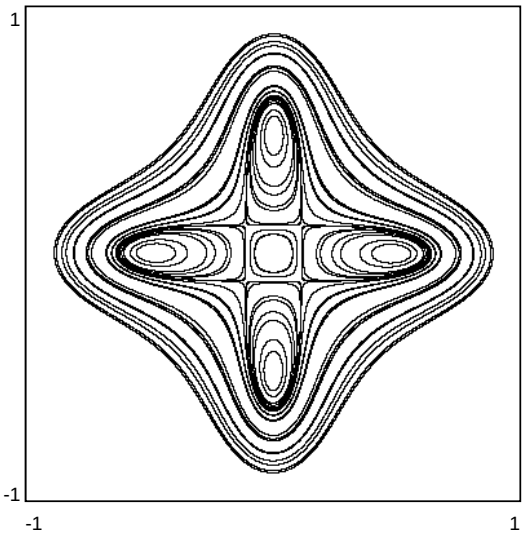

(b) Normal form U

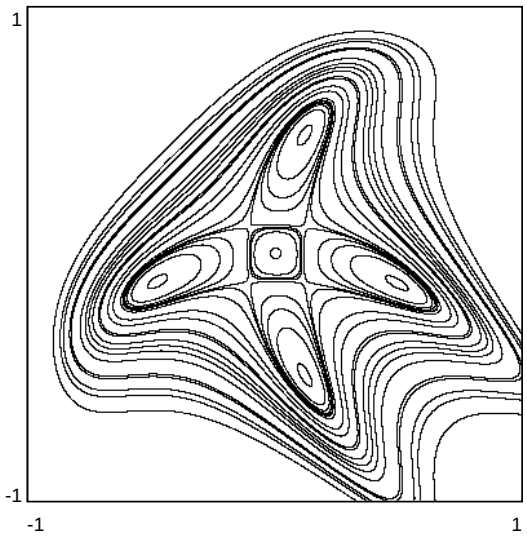

(c) Mapping $\Phi^{-1}U\Phi$

Figure 4.1: Phase space topology of the quadratic 2D Hénon mapping with $\omega/2\pi = 0.251$ and of the associated quasi-resonant normal form for the fourth order resonance.

from the resonance by ϵ, *i.e.* $\omega = 2\pi\frac{p}{q} + \epsilon$. The resulting Hamiltonian reads

$$\begin{aligned} h(\theta,\rho) =& \epsilon\rho + \sum_{n=1}^{(q-1)/2} \frac{\Omega_{2n}}{n+1}\rho^{n+1} \\ &+ \frac{\epsilon e^{-i\omega}}{e^{-i\epsilon q}-1} u_{0,q-1}\rho^{q/2}e^{iq\theta} \\ &+ \frac{\epsilon e^{i\omega}}{e^{i\epsilon q}-1} u^*_{0,q-1}\rho^{q/2}e^{-iq\theta}, \end{aligned} \tag{4.27}$$

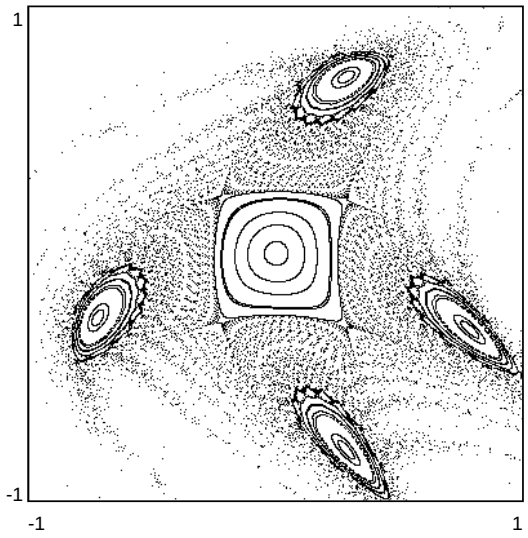

(a) Hénon mapping F

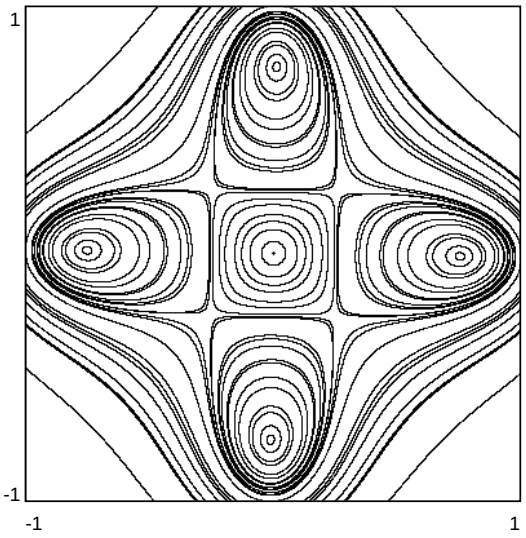

(b) Normal form U

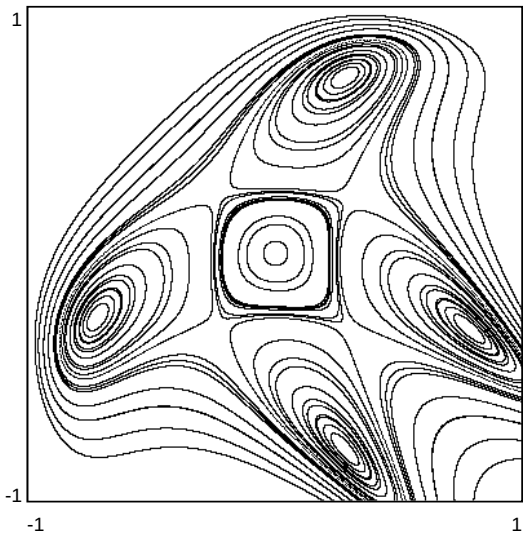

(c) Mapping $\Phi^{-1}U\Phi$

Figure 4.2: Phase space topology of the quadratic 2D Hénon mapping with $\omega/2\pi = 0.255$ and of the associated quasi-resonant normal form for the fourth order resonance.

where Ω_{2n} are the coefficients of the amplitude dependent frequency coming from the normal form where the nonresonant part is written as an amplitude dependent rotation:

$$U(\zeta, \zeta^*) = e^{i\Omega(\zeta,\zeta^*)}\zeta. \tag{4.28}$$

The coordinates of this Hamiltonian are defined by

$$\zeta = \sqrt{\rho} e^{i\theta} \tag{4.29}$$

$$\zeta^* = \sqrt{\rho} e^{-i\theta}. \tag{4.30}$$

In this section we construct the explicit Hamiltonian interpolating the quasi-resonant normal form of the Hénon mapping for the fourth order resonance and we analyze this mapping using the Hamiltonian.

4.3.2 Analysis of the fourth order resonance

We recall the main coefficients of the normal form:

$$\Omega_2 = -\frac{1}{16}\left(3\cot\frac{\omega}{2} + \cot\frac{3\omega}{2}\right) - \frac{3}{8}\kappa \tag{4.31}$$

$$u_{0,3} = \frac{i}{16} e^{i\omega}\left(\cot\frac{\omega}{2} - \cot\frac{3\omega}{2} - 2\kappa\right), \tag{4.32}$$

where Ω_2 was obtained from $u_{2,1}$ *via* the relation $u_{2,1} = e^{i\omega} i\Omega_2$.

In the case of the fourth order resonance, and truncating at the lowest order, the Hamiltonian (4.27) can be cast into the form

$$h(\theta, \rho) = \epsilon\rho + \frac{\Omega_2}{2}\rho^2 + \epsilon\,|u_{0,3}|\,\rho^2\cos(4\theta + \psi - \omega), \tag{4.33}$$

where $\omega = \frac{\pi}{2} + \epsilon$ and where ψ is defined as

$$\text{Arctan}\left(\frac{Im(u_{0,3})}{Re(u_{0,3})}\right). \tag{4.34}$$

We can translate the coordinate θ to set the phase of the cosine to zero in (4.33), we obtain:

$$h(\theta, \rho) = \epsilon\rho + \frac{\Omega_2}{2}\rho^2 + \epsilon\,|u_{0,3}|\,\rho^2\cos(4\theta), \tag{4.35}$$

We successfully verified this Hamiltonian and its coefficients using the numerical coefficients given by the code GIOTTO.

The phase space topology of this Hamiltonian is plotted in figure 4.3, for a distance from the distance equal to $\epsilon = 2\pi \times 0.005$.

From this Hamiltonian we can extract quantitative information about the topology of the phase space. In our case we are mainly interested in the positions of the fixed points and in the surface of the islands.

The position of the fixed points of the normal form mapping can be estimated by the computation of the fixed points of the truncated Hamiltonian [27]. We obtain

$$\theta^{fp} = \frac{k\pi}{4} \tag{4.36}$$

$$\rho_{\pm}^{fp} = \frac{-\epsilon}{\Omega_2 + 2\epsilon\,|u_{0,3}|} \tag{4.37}$$

where k takes the integer values from 1 to 8. In the expression of ρ_{fp} we made the approximations of [27]. We also define an average ρ for the fixed points: $\rho_0 = \frac{-\epsilon}{\Omega_2}$.

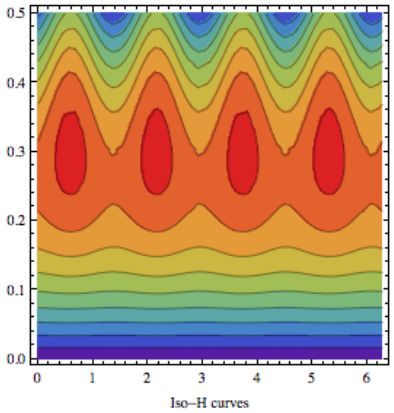

Figure 4.3: Phase space topology of the Hamiltonian (4.33) for $\omega = 2\pi \times 0.255$ and $\kappa = 0$.

The existence of the fixed points is given by the condition $\epsilon\Omega_2 < 0$. From that condition we state here an important comment: given the expression of Ω_2, we observe that its sign depends on the sign and value of κ. Therefore for a given value of κ that condition tells us in which direction we have to cross the resonant value of the tune. In our numerical studies we shall use values of κ ranging from $\kappa = -1.1$ to $\kappa = -1.9$. Numerically estimating the condition for the existence of the fixed points, we conclude that, for that value of κ, we have to cross the resonance from above, *i.e.* the fixed points exist for values of the tune below 0.25.

We can also link these results to the Poincaré-Birkhoff theorem discussed in section 3.3.2. We estimate the stability of the fixed points using the Hessian matrix of h,

$$\begin{pmatrix} \frac{\partial^2 h}{\partial^2 \rho} & \frac{\partial^2 h}{\partial \rho \partial \theta} \\ \frac{\partial^2 h}{\partial \rho \partial \theta} & \frac{\partial^2 h}{\partial^2 \theta} \end{pmatrix} \tag{4.38}$$

computed in the coordinate of the fixed points, *i.e.* (ρ_+, θ_{2k}) and (ρ_-, θ_{2k+1}) [27]. Its determinant reads $-\Omega_2\epsilon\,|u_{0,3}|\,4^2\rho_0^2(-1)^k$.

In consequence, if $-\Omega_2\epsilon\,|u_{0,3}| > 0$, the points with k even are elliptic and the others are hyperbolic [27]. This is then in agreement with the Poincaré-Birkhoff theorem.

Validity of the fixed points formulas for the fourth order resonance: We tested that approach numerically using GIOTTO to find the position of the fixed points. We performed tests for different values of the tune and for different values of κ. We concluded that if we limit our formulas to the lowest order as done above, the analytical expressions for the position of the fixed points are unable to reproduce the correct behavior.

Indeed, as also mentioned in [27], the approach described below is limited due to the peculiar behavior of the fourth order resonance: in the Hénon mapping, for the fourth order resonance, the amplitude of the elliptic fixed points and the amplitude of the hyperbolic fixed points behave differently with respect to ϵ. However in our approach, using the Hamiltonian (4.35), we do not reproduce the correct behavior, and therefore the expressions for $\rho_\pm$ are not valid.

To validate these conclusions we tested the same approach in the case of the fifth order resonance. We did the same normal form analysis to compute the interpolating Hamiltonian. The results for the coefficients of the normal form and the conjugating function are reproduced in section A.1. These coefficients we validated numerically using GIOTTO.

Using the interpolating Hamiltonian for the fifth order resonance we were able to test the validity of the formulas giving the position of the fixed points using the numerical estimates given by GIOTTO.

The phase space topology given by the interpolating Hamiltonian of the fifth order resonance is displayed in figure 4.4.

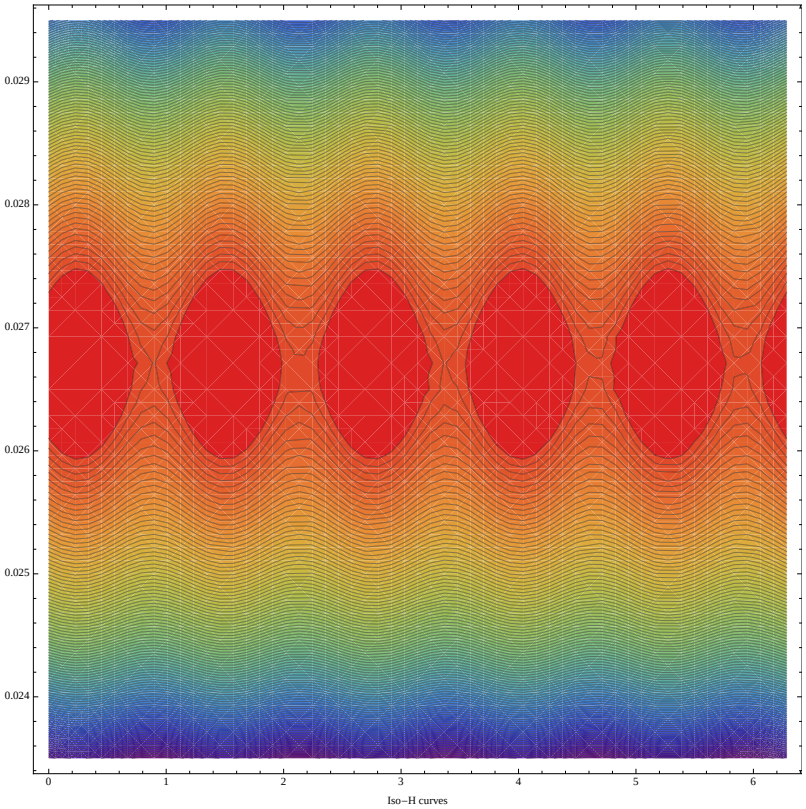

Figure 4.4: Phase space topology of the Hamiltonian of the fifth order resonance for $\omega = 2\pi \times 0.201$ and $\kappa = 0$.

4.4 Analytical model of the trapping probability for MTE

We sketch here the main ideas of a new approach allowing the obtain an analytical estimation of the trapping probability of particles inside the islands when they cross the separatrix.

Following Ref. [39], the probability of capture at the separatrix crossing is given by

$$\frac{\dot{\Sigma}_1}{\dot{\Sigma}_1 + \dot{\Sigma}_2} \tag{4.39}$$

where the dot denotes the time derivative, and where $\Sigma_{1,2}$ are the surfaces of the phase space regions where the capture occurs. In our case, Σ_1 is the surface of the island, while Σ_2 is the surface of the inner region. We can explain the process looking at figure 4.4: as the tune varies, the islands move for the origin and their separatrix will cross the orbit of a particle. At that

point, the particle can either jump inside the island or be scattered in the inner region. In the first case the particle will be trapped inside the island.

If we want to apply that approach, the first step is to obtain an analytical expression for the size of the islands. This is possible if one translates the Hamiltonian (4.35) according to $\tilde{\rho} = \rho - \rho_0$. The new Hamiltonian becomes

$$h(\theta, \tilde{\rho}) = \Omega_2 \frac{\tilde{\rho}^2}{2} + \epsilon \left| u_{0,3} \right| \rho_0^{q/2} \cos(q\theta). \tag{4.40}$$

From that Hamiltonian the equation of the separatrix is readily obtained as it is already translated to ρ_0. Integrating the equation of the separatrix [27], we obtain an analytical expression for the surface of the islands:

$$\Sigma_1 = 16 \sqrt{\rho_0^2 \left| \frac{1}{\Omega_2} \epsilon u_{0,q-1} \right|}, \tag{4.41}$$

where q is the order of the resonance.

Using these expression we can thus define the probability of capture of a particle undergoing the separatrix crossing at the tune $\nu = 1/q + \epsilon/2\pi$:

$$P(\epsilon, \kappa) = \frac{2\dot{\Sigma}_1}{4\pi\dot{\rho}_0 + \dot{\Sigma}_1}. \tag{4.42}$$

At that point we concentrated our efforts on that approach in the fifth order case (to avoid the peculiarities of the fourth order resonance) but we were not able to obtain definitive results.

Nevertheless we computed all the quantities needed to test that formula and we verified them numerically using GIOTTO. We now want to investigate in more details the impact of our approximations to be able to compare the results given by this approach with our simulations.

CHAPTER 5

Manzoni: a numerical tool to study the MTE dynamics

In this chapter we describe the numerical code we wrote to perform the numerical simulations related to the MTE dynamics. This code allows the tracking of a particle distribution through a linear machine containing nonlinearities described in the kick approximation. We first review the requirements for such a code in section 5.1 and we thus describe in section 5.2 its main features and properties. The simulations setup and outputs are discussed in sections 5.3 and 5.4.

5.1 Numerical tools for the study of beam dynamics . . . 65
5.2 Manzoni: a code for the tracking of symplectic mappings . . . 66
5.2.1 Comparison with the MTE Fortran code . . . 67
5.2.2 Implementation of the physical aspects of the beam tracking . . . 67
5.3 Setup of the simulations . . . 69
5.3.1 Initial beam distribution . . . 69
5.3.2 Parameters of the mapping . . . 69
5.4 Output of the simulations . . . 71
5.4.1 Histograms and plots . . . 71
5.4.2 Moments and population of the beamlets . . . 71
5.4.3 FFT analysis . . . 72

5.1 Numerical tools for the study of beam dynamics

Nowadays computer codes play an important role in accelerator physics. Indeed the equations governing the motion of particles in a magnetic lattice are in general not analytically solvable, if one abandon the linear approximation, the equations of motion become non-linear and generally no closed-form analytical solution exists.

Therefore computer codes related to the understanding of the motion of the particles were first created to numerically solve the linear Hill's equations (usually in the transfer matrix formalism) to obtain the Twiss' parameters describing the linear lattice of the machine. This allowed understanding and computing the beam orbit of the ideal linear machine.

However in order to include the effect of nonlinear elements on the beam, one has to rely on tracking simulations. A wide variety of tracking code exists serving different purposes. Here we only mention one of them: Polymorphic Tracking Code (PTC) [40] as it is widely used at CERN.

PTC is largely used for the MTE design and optimization. PTC is a symplectic tracking module used in combination with Methodological Accelerator Design (version X) (MAD-X)[1].

The tracking code MAD-X/PTC was used to "completely" simulate the beam behavior in the PS machine in view of the design of the MTE method. Such results are able to take into account a very complete and precise description of the real machine, *e.g.* including the precise positioning of each elements and their misalignment. A script code was developed [41] to run MAD-X/PTC in a way that one is allowed to simulate tune variation required for the MTE beam splitting.

Although such results are of high quality and can in general be sufficient to characterize the whole beam manipulation processes involved in the MTE method, they are not suited for the goal pursued in this work. Indeed, our goal is slightly different: we want to understand the basic physical properties and mechanisms occurring during the beam splitting, *i.e.* the dynamics of the models of the MTE beam splitting: the generalized Hénon mapping with, in some cases, some additions, for example a second kick modeling the effect of a fast kicker. Thus in order to understand the underlying physical principles, one has to be able to isolate the effects of the different elements and to perform simulation able to be directly interpretable in term of the parameters of the model.

In addition, one of our goals is to perform an exploration of the parametric space of the generalized Hénon mapping and we should be able to perform a large number of simulations, each for a different set of parameters. This requires a fast tracking code whose running time is in order of hours instead of days as it is the case for the MAD-X/PTC code simulating the MTE process in the PS. Moreover the existing codes do not allow easily changing the parameters during the tracking, *e.g.* the one we are required to do for the tune variation used for the splitting.

These are the reasons why we developed a special code for these studies.

5.2 Manzoni: a code for the tracking of symplectic mappings

Manzoni can be defined as a tracking code for the parametric study of symplectic mappings. In addition it features an important flexibility in the definition of time varying parameters of the mappings.

Manzoni is implemented using the C++ programming language. During the design phase we tried to focus on two main design requirements: the modularity and thus openness of the

[1] MAD-X [4], the latest version of MAD is a "general purpose accelerator and lattice design program" [20]. The magnetic elements of the machines are described as input and MAD allows the user to obtain and match the linear lattice parameters (mainly the Twiss' parameters and the tunes) and some first order non linear parameters such as the chromaticities. In addition MAD-X can be used in conjunction with libraries such as PTC to perform tracking simulations including the non linear elements up to any order.

code and the speed of the tracking process. The first allowed various extensions of the code to cope with the simulations requirements at hand while the second allowed running a large number of simulations in a limited amount of time, allowing to correct and refine many aspects of the simulations.

Manzoni follows an object-oriented modular design and uses several C and C++ libraries in addition to the C++ Standard Library: the GSL library (GNU Scientific Library, see [42]) for random number generation and FFT analysis, the Blitz++ library (see [43]) for efficient mathematical manipulation of large data structures, the Xerces-C++ library (see [44] for XML manipulations of input files and the ROOT library (see [45]) for graphical output.

The cores libraries used are the Standard C Library, the Standard C++ Library and the GNU Scientific Library, mainly for random number generation. For the graphical output and to produce various plots it uses the CERN ROOT framework. In its current state the source code reaches almost 6000 lines of code divided in 19 C++ classes [2].

5.2.1 Comparison with the MTE Fortran code

At the start of the MTE design, a Fortran code was developed to simulate the generalized Hénon mapping and the beam splitting process [48]. At the start of this work, that code was used for the numerical studies. Various required features for our simulations were not present in this code: multi-kick mappings, time variation of parameters other than the tune, special kind of polynomial time variation of the tune, tracking data suitable for FFT analysis, etc.

We thus decided to implement these features in a new code, allowing to follow our goals of increased modularity and it also appeared interesting to note that we obtained a large gain in performance, especially for the 4D simulations. Tests made on CERN computer center machines (*lxplus* and *lxbatch*) showed computing time from five up to ten times faster using Manzoni.

5.2.2 Implementation of the physical aspects of the beam tracking

We now discuss the link between the physical concepts of the tracking and the way they are implemented in Manzoni. The tracking is performed in the kick approximation by assuming that a nonlinear element will act on the particle at a single point by modifying only the angle. The core of the implementation of the physics is of course the concepts of the transfer maps formalism (described in section 2.3).

The mappings modeling the MTE method are analytically manipulated expressed in the normalized Courant-Snyder coordinates (see chapter 3). When Manzoni uses these mappings it also manipulate these normalized coordinates in the subsequent computations (tracking, output data and plots). We recall here how these coordinates are obtained from the physical ones [3] [28]:

[2] In addition to the main code, a small utility script has been written in the Ruby programming language [46] to allow an easy manipulation of Manzoni. For example it allows to run a parametric simulation campaign on the CERN batch computing facilities [47] generating the parametric simulation input files and launching automatically the required number of instances of Manzoni.

[3] These are the coordinates (position, angle), *i.e.* the canonical coordinates under the approximation of constant energy, as discussed in section 2.2.3.

1. Physical coordinates:

$$(x, x'), \text{ and} \tag{5.1}$$
$$(y, y'); \tag{5.2}$$

2. Courant-Snyder coordinates:

$$(\hat{\boldsymbol{x}}, \hat{\boldsymbol{x}}') = (\frac{x}{\sqrt{\beta_x}}, \frac{\alpha_x}{\sqrt{\beta_x}}x + \sqrt{\beta_x}x'), \text{ and} \tag{5.3}$$
$$(\hat{\boldsymbol{y}}, \hat{\boldsymbol{y}}') = (\frac{y}{\sqrt{\beta_y}}, \frac{\alpha_y}{\sqrt{\beta_y}}y + \sqrt{\beta_y}y'); \tag{5.4}$$

3. Normalized (adimensional) Courant-Snyder coordinates:

$$(\hat{\boldsymbol{X}}, \hat{\boldsymbol{X}}') = \lambda(\hat{\boldsymbol{x}}, \hat{\boldsymbol{x}}') \text{ with } \lambda = \frac{1}{2}K_2\beta_x^{3/2}, \text{ and} \tag{5.5}$$
$$(\hat{\boldsymbol{Y}}, \hat{\boldsymbol{Y}}') = \lambda(\hat{\boldsymbol{y}}, \hat{\boldsymbol{y}}') \text{ with } \lambda = \frac{1}{2}K_2\beta_y^{3/2}. \tag{5.6}$$

To implement the tracking method, the first step is to generate a particle distribution corresponding to the desired beam emittances. A real beam can often be considered as a bi-Gaussian distribution and therefore, Gaussian beam distribution are often considered by tracking codes [6]. Another model is to consider the distribution to be uniform in polar transverse coordinates beam.

In Manzoni these two options are implemented. In the Gaussian case the emittance is related to the sigma of the Gaussian distribution by

$$\rho(\hat{\boldsymbol{X}}, \hat{\boldsymbol{X}}') = \frac{1}{2\pi\sigma^2}e^{-(\hat{\boldsymbol{X}}^2+\hat{\boldsymbol{X}}'^2)/(2\sigma^2)}, \tag{5.7}$$

with $\sigma^2 = \epsilon$ (the definition is valid for both the horizontal and the vertical emittances). And in the uniform case, one just specifies maximum radii in each planes.

Manzoni is able to perform 2D and 4D simulations [4]. The user selects the option for a 2D or a 4D simulation and a corresponding beam is generated. Different distribution options can be provided for the horizontal and the vertical planes.

The different mappings discussed bellow are provided for both cases, the 4D mappings reducing to 2D mappings as the coupling parameter χ goes to 0.

As we already discussed the ideal model of the MTE dynamics is given by the following Hénon-like 4D polynomial map, or its 2D counterpart [33]:

$$\begin{pmatrix} \hat{\boldsymbol{X}} \\ \hat{\boldsymbol{X}}' \\ \hat{\boldsymbol{Y}} \\ \hat{\boldsymbol{Y}}' \end{pmatrix}_{n+1} = R(\omega_x, \omega_y) \begin{pmatrix} \hat{\boldsymbol{X}} \\ \hat{\boldsymbol{X}}' + \hat{\boldsymbol{X}}^2 - \chi\hat{\boldsymbol{Y}}^2 + \kappa\left(\hat{\boldsymbol{X}}^3 - 3\chi\hat{\boldsymbol{X}}\hat{\boldsymbol{Y}}^2\right) \\ \hat{\boldsymbol{Y}} \\ \hat{\boldsymbol{Y}}' - 2\chi\hat{\boldsymbol{X}}\hat{\boldsymbol{Y}} - \kappa\left(\chi^2\hat{\boldsymbol{Y}}^3 - 3\chi\hat{\boldsymbol{X}}^2\hat{\boldsymbol{Y}}\right) \end{pmatrix}_n . \tag{5.8}$$

This is the main mapping implemented by Manzoni and it can be configured using the options detailed in sections 5.3.1 and 5.3.2.

[4] A basic implementation of 5D simulations is also provided. Including a very crude model of transverse-longitudinal coupling *i.e.* only the first order chromaticity and a fixed longitudinal tune.

Nevertheless other mappings are also implemented: a simple rotation with a constant kick, corresponding to a kicker magnet located at the end of a linear section of the machine and a octupolar mapping, similar to the mapping 5.8 but without sextupole.

It should also be noted that due to the modular architecture of the code, other similar mappings can easily be implemented and included in the nonlinear lattice description.

An important feature of the code is the ability to specify a given time dependence to almost any relevant parameters of the mappings. This variation with the turn number can be linear, polynomial or sinusoidal with a fixed or evolving frequency. In addition, the turn-by-turn dependence of the parameter can be read from a file, allowing to easily provide any desired dependence. dependence Once the beam distribution has been generated, the code starts the tracking. The particles are transported (a rotation in phase space) to the next kick, the kick parameters (which are time dependent) are computed and the kick is applied to the whole beam. This process is repeated turn after turn. Efforts have been made to provide an implementation of this (simple) algorithm as efficient as possible to speed up the simulations.

5.3 Setup of the simulations

In this section we provide details about the actual setup common to the various simulations we performed. As each simulation features a particular aspect of the physics of the problem we try to describe here the parameters in a generic way, of course the specificities of the simulations discussed in the next chapter shall be highlighted in due course.

As the setups used for the 2D simulations are similar to the ones used for the 4D simulations we discuss only the setup used for the 4D simulations as they involve a more complete set of parameters.

5.3.1 Initial beam distribution

Two different beam distributions have been used: a Gaussian beam distribution and a uniform one [5]. They are described by the location of their centroids and by a size parameter: the sigma of the distribution in the Gaussian case and the radius in the uniform case. In all the simulations, the centroids of the initial beam are set to zero.

The number of tracked particles was in all cases of the order of 1×10^6 for the 2D simulations and of 4×10^6 for the 4D simulations. Assuming that the numerical errors on the computed quantities (such as the population of each islands or the emittances) goes as $\frac{1}{N}$ where N is the number of tracked particles, this allows to have a numerical error much lower than the differences on these quantities observed as we vary other tracking parameters.

5.3.2 Parameters of the mapping

The main parameters of the simulation are related to the mapping itself and are located in the *iterator* section of the input file. We describe here the main parameters used to perform the simulations.

[5] As described in chapter 5.2.2, these distributions refer to the normalized Courant-Snyder coordinates.

Number of turns

This is a very global parameters defining the number of iteration of the mappings on the initial tracked particles' distribution. For example, for a given variation of the tune, increasing this parameter will give a slower variation of the tune.

At every turn the values of the time dependent parameters are updated.

Number of kicks

In the simulations using the generalized Hénon mapping there is of course a single kick containing a sextupolar and an octupolar component is applied each turn. However Manzoni gives the possibility to define multiple kicks per turn to perform other beam manipulations. For example it is possible to simulate the effect of a fast kicker (damper) acting with a defined phase advance with respect to the Hénon kick. In that case one need to define two kicks and to specify the phase advance between the two.

Another case where the ability to defines two different kicks concerns the non-linear coupling correction performed with a second family of octupoles.

It is possible to define the order of the kick (*i.e.* linear, sextupolar or octupolar) and the phase advance between each kick. In addition, each of these phase advance can vary independently with the turn number.

Tune variation

In case of multiple kicks, this is actually the phase advance between kicks. We describe here its effect in the case of a single kick, *i.e.* this is the tune variation of the machine. The tune (as the other parameters) can vary on a turn-by-turn basis. In most of the cases a linear tune variation is used. In that case one has to specify the initial and the final tune values.

Another possibility is to have a polynomial tune variation. In this case, in addition to the initial and final value of the tune, one can specify a choose value of the tune at a given turn. Two polynomial variations of a chosen order are then build before and after this intermediate turn. The slope of the polynomial function at that point can also be specified.

Nonlinearities

Apart from the normalization used by Manzoni, the parameter governing the strength of the nonlinear elements in the generalized Hénon mapping is κ, *i.e.* the strength of the octupole compared to the strength of the sextupole.

In most of the simulations, unless explicitly noted, this parameter is constant during the simulation. In some simulations we varied the value of κ in a linear way, or using a polynomial variation identical to the polynomial tune variation discussed in the previous section.

Coupling between the horizontal and the vertical motion

This is the χ parameter of the generalized 4D Hénon mapping (equation 5.8). It is mandatory to specify this parameter in case of a 4D simulation. Although we did not use this possibility, Manzoni also gives the possibility to vary this parameter.

In the 4D simulations, we set this parameter as $\chi = 0.5$ unless otherwise specified. This correspond to the actual case of the PS where the ratio of the horizontal and vertical beta functions is one half.

5.4 Output of the simulations

Different *data processing* modules of Manzoni can be called before the iterations, at a specified turn of the iterations and after the completion of the process. The code allow to compute different quantities at these times: the moments of the distribution or of some subparts of it, the losses, the coherent orbit of the beam and their frequencies through a FFT analysis. In addition the code allows the user to obtain various histograms of the distribution.

To obtain the results of our simulations, we call these modules at the beginning to check that the simulation parameters are correct and we call them at the end of the iterations to generate the actual results.

5.4.1 Histograms and plots

We usually generate histograms of the distribution in different projections of the complete phase space. In the 2D simulations this is of course the beam distribution in the xx' plane. In 4D simulations histograms for other projections can be generated.

Figure 5.1 shows such histograms for a 4D simulation at the end of the trapping process.

Plots of the distribution projected on a single coordinate axis can also be requested to highlight specific aspects. Figure 5.2 shows the results of a typical 2D simulation where the beam is spitted at the end of the process. One can observe the link between the phase space plot and the beam projection on the horizontal coordinate. These plots and histograms allow a qualitative analysis of the simulations.

5.4.2 Moments and population of the beamlets

This is the key of the MTE process and indeed the core of the quantitative results of the simulations. The approach used to compute the number of particles in each beamlets and their moments is rather simple. Usually the beam is split in the XX' planes. First, the phase space is projected onto this 2D space; second we define a box surrounding the origin and we divide this box in a number of sub-boxes. Given the specificities of the splitting, the beamlets are located at a given location. Therefore we just have to put the boxes around the beamlets. Simply counting the particles in the box we can then estimate the population of the beamlets.

Another important output of the code is the emittance of the beamlets. The emittances can be defined from the statistical estimation of the second order moments of the beam:

$$\epsilon = \sqrt{\langle X^2 \rangle \langle X'^2 \rangle - \langle XX' \rangle} \tag{5.9}$$

where $\langle \cdot \rangle$ represents the average over the beam distribution [11]. This definition is valid for both the horizontal (xx') and the vertical emittances (yy').

This gives the emittances in the coordinates used by Manzoni, *i.e.* the normalized Courant-Snyder coordinates. To obtain the emittance in the physical coordinates, one first has to transform in the Courant-Snyder coordinates using the scaling factor

$$\lambda = \frac{1}{2} K_2 \beta_x^{3/2}. \tag{5.10}$$

The transformation between the Courant-Snyder and the physical coordinates being symplectic, this actually gives the physical emittance of the beam.

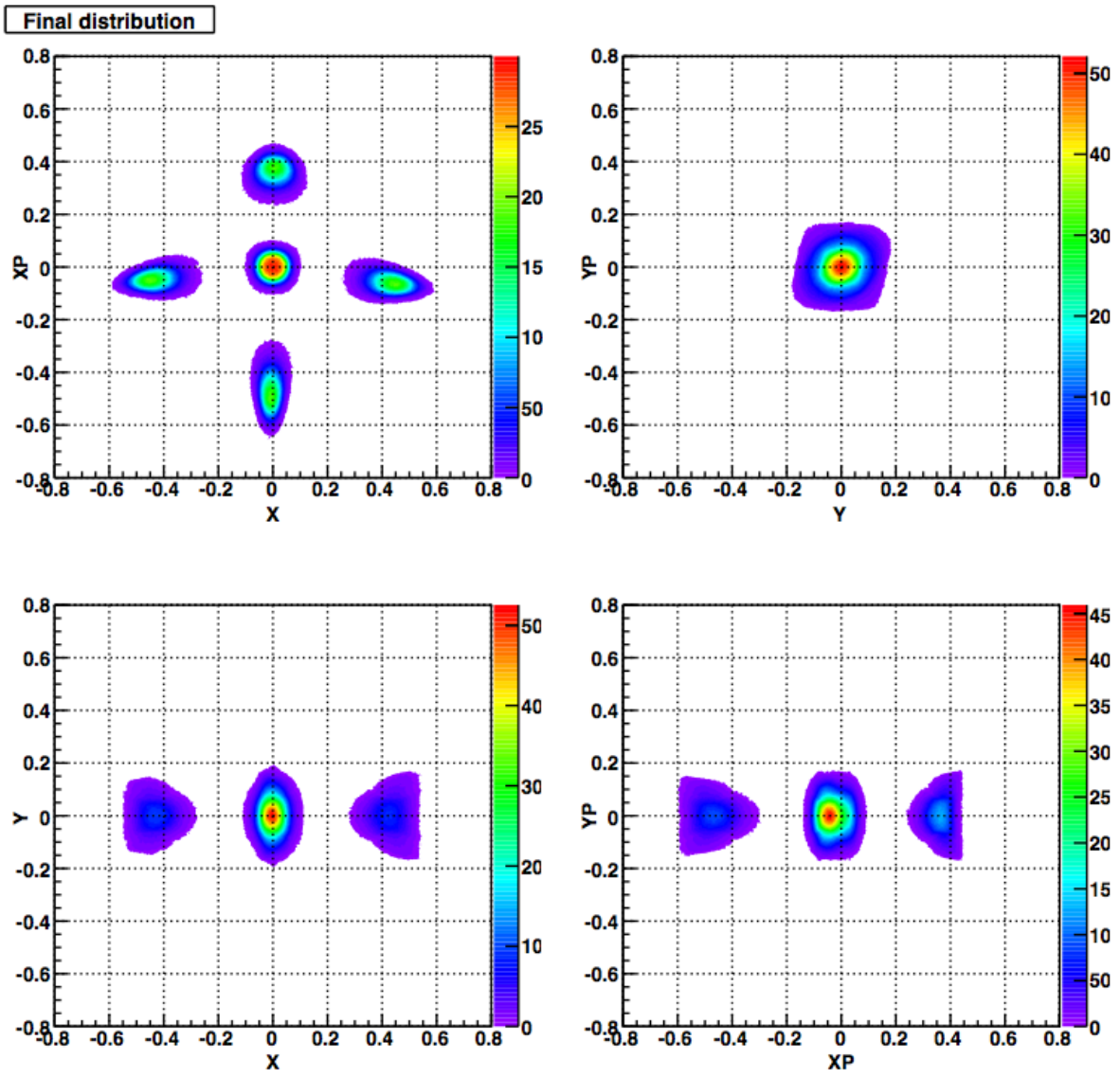

Figure 5.1: Typical histograms of the beam distribution in the subspaces of the 4D phase space at the end of the trapping process.

In addition to the emittance calculated from the second order moments, Manzoni also output the third and fourth order moments of the beam. This allows to compute the *halo parameter* [49] of the beam:

$$h = \frac{\langle x^4 \rangle}{\langle x^2 \rangle^2} - 2. \tag{5.11}$$

5.4.3 FFT analysis

Another important feature of the tracking codes is the ability to extract tracking data of the centroids of the beam in order to perform a frequency analysis.

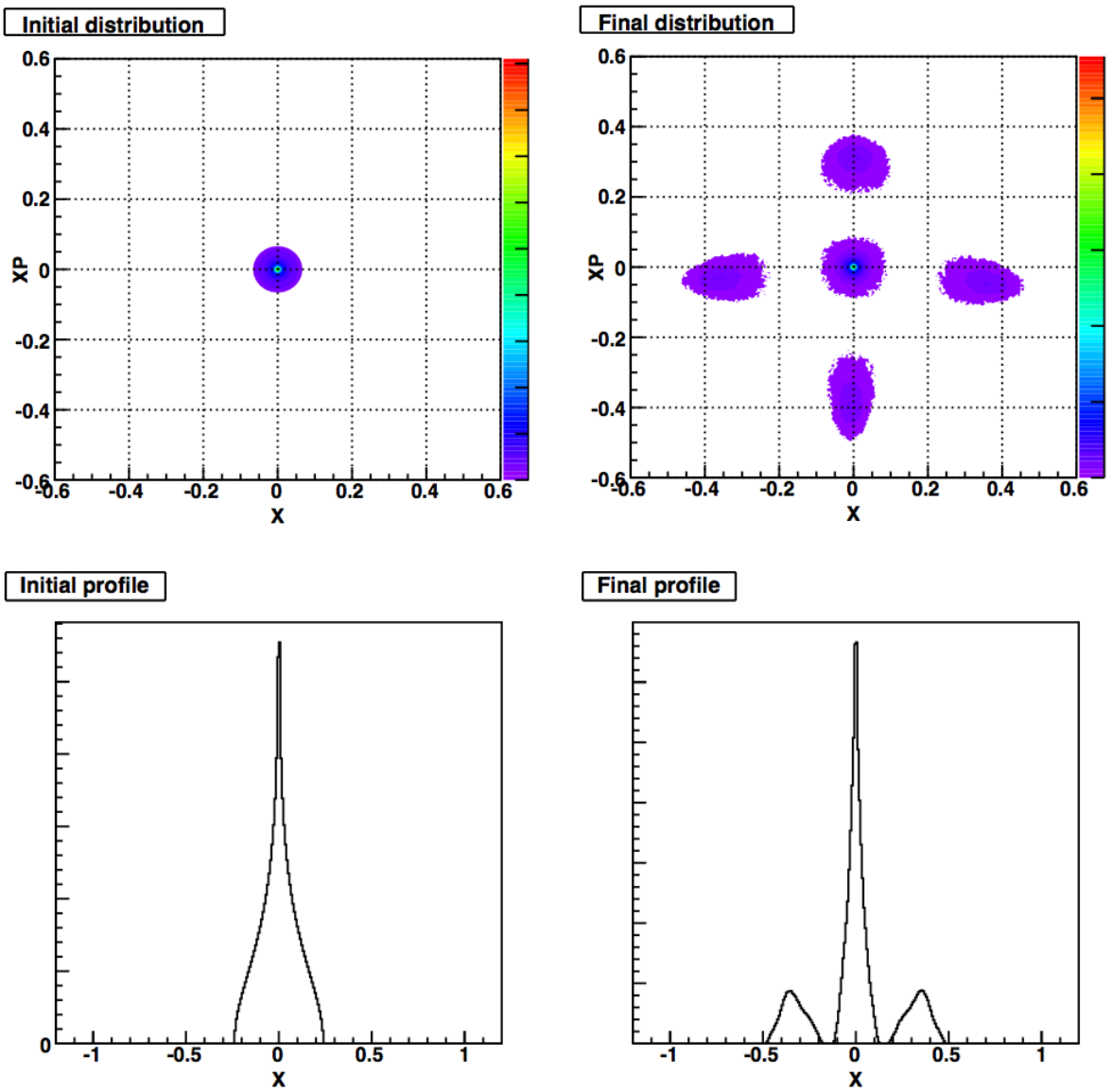

Figure 5.2: Phase space plots (initial (top left) and final (top right)) and profiles of the projection on the horizontal coordinate (initial (bottom left) and final (bottom right)) of a typical simulation where the MTE beam splitting is performed. The initial beam distribution is uniform in the horizontal and vertical planes.

The centroid of the beam, *i.e.* the first order moments in each plane are computed at each turn and can be used by other codes, such as Sussix [50] to perform a FFT analysis to obtain the tunes, but also the other driving terms.

To do that, Manzoni can save the tracking data in a file, but a FFT analysis giving the tunes and its time evolution has also be implemented directly in Manzoni.

In addition, it is also possible to obtain the tracking data of single particles of chosen initial coordinates. This allows for example to compute easily the detuning with amplitude.

CHAPTER 6

2D numerical studies of the MTE dynamics

In this chapter we analyze the results of the numerical two-dimensional simulations performed with Manzoni. Two main results are obtained from these simulations: the trapping fraction, which is discussed in section 6.2 and the emittance sharing between the core and the islands, analyzed in section 6.5. These results are compared and analyzed for a large set of parameters: the type of the initial beam distribution, the beam emittance, the strength of the sextupoles and octupoles, and the functional dependence of the tune variation. We also obtain a global fitted model of the trapping fraction that we discuss in section 6.3. Moreover these simulations allowed us to obtain a numerical estimate of the minimal trapping amplitude; we discuss that result in section 6.4. To sum up, our main conclusions about these 2D simulations are discussed in section 6.6.

6.1 Numerical study of the 2D generalized Hénon mapping . . . 75
6.2 Parametric dependence of the trapping fraction . . . 75
6.2.1 Comparison of methods used to compute the trapping fraction . . . 75
6.2.2 Effect of the initial beam emittance . . . 76
6.2.3 Comparison between a Gaussian and a uniform beam distribution . . . 78
6.2.4 Effect of the slope of the tune variation . . . 80
6.2.5 Effect of the functional form of the tune variation . . . 82
6.2.6 Effect of the value of κ . . . 82
6.3 Global fitted model of the trapping fraction . . . 87
6.4 Minimal trapping amplitude . . . 89
6.5 Parametric dependence of the emittance sharing between the beamlets . . . 90
6.5.1 Islands and core emittances ratio . . . 90
6.5.2 Tune curve slope effect on the emittance sharing . . . 92
6.5.3 Effect of the variation of κ on the emittances ratio . . . 93
6.6 Conclusions on the 2D numerical studies . . . 94

6.1 Numerical study of the 2D generalized Hénon mapping

The first step to understand the effects of the various parameters on the trapping probability and emittance sharing is to analyze the generalized 2D Hénon mapping, *i.e.* the most simple and ideal model of the MTE extraction process, as described in section 3.3.

All these results are then based on the tracking of the 2D Hénon model as described in chapter 5 where the trapping process is performed using a linear or polynomial tune variation. Unless otherwise specified, the tune variation in the majority of the simulations is linear starting from the non-resonant value $\nu = 0.252$, crossing the resonance at $\nu = 0.25$ and then trapping and moving the islands to $\nu = 0.245$.

The simulation campaign thus tries to analyze the effects of the initial beam emittance, the number of turn over which the splitting is performed, the value and evolution of the non linear gradients (*i.e.* the value of the parameter κ) during the capture process and the functional dependence of the tune variation on the trapping fraction and on the emittance sharing between the beamlets. The core of this part of the work thus consists in simulations scanning over a wide range of values for these parameters. In addition, the results were compared between two types of initial distributions, Gaussian and uniform.

6.2 Parametric dependence of the trapping fraction

This first output of our simulations that we analyze is the trapping fraction, *i.e.* the fraction of the particles trapped in the islands. This result is analyzed in the next sections for different values of the parameters and for variations of these parameters during the trapping process

6.2.1 Comparison of methods used to compute the trapping fraction

This first step is about the methodology used in all our simulations. As explained in chapter 5, the trapping fraction is computed from the population of the islands, which is obtained by counting the particles in a box surrounding an island. To obtain the trapping fraction one can choose between two methods: counting the particles in one island or counting the particles in the core and making the subtraction, *i.e.*

$$N_{core} = N_{total} - N_{islands}, \tag{6.1}$$

provided there is no loss, which is the case in all the results discussed here, except otherwise mentioned.

It can then be argued that fluctuation will influence the result obtained from one method compared to the other. Nevertheless an optimization has been done on the choice of the parameters of the boxes in other to actually reflect the number of particles in the islands without miscounting between the core and the islands [1]. The results of the two methods are extremely close as shown in the example of figure 6.1.

This provides a good level of confidence in the real significance of the results discussed in this chapter.

[1] At the beginning of our work we took some time to set these parameters properly to gain more confidence in the results.

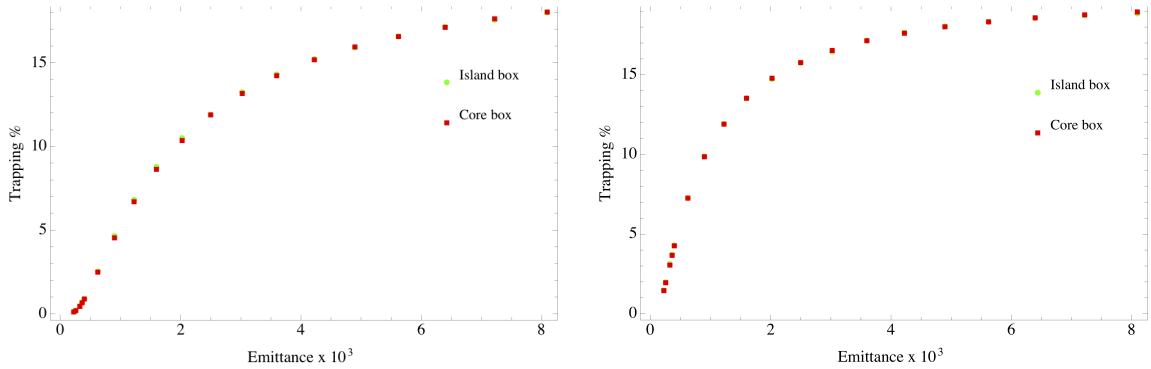

(a) $\kappa = -1.3$, 5000 turns. (b) $\kappa = -1.8$, 15000 turns.

Figure 6.1: Comparison between the results obtained from the two computation methods using a Gaussian distribution for a particular choice of the number of turns and of κ for different emittances. Results from the islands boxes are in purple and those from the core box are in brown.

6.2.2 Effect of the initial beam emittance

Compared to the other parameters, the initial beam emittance plays a particular role in the resulting trapping fraction. Indeed it is not an intrinsic parameter of the mapping but rather an external parameter, a parameter of the beam. One can then expect a behavior of the trapping fraction depending on the emittance but globally independent on the other parameters; *e.g.* if one optimize the trapping with parameters like the number of turns or the variation of κ, the effect could be expected to be similar for different beam emittances. This allows discussing in this section the global behavior of the trapping fraction as a function of the initial beam emittance, such as its asymptotic behavior and the way we can fit the results. Then in the next sections we can reuse this analysis and these fits to observe more precisely the effect of the other parameters.

Figure 6.2 shows the trapping fraction obtained for different emittances and for four different couples of the number of turns and values of κ (whose effects shall be analyzed later), scanning from $\epsilon_h = 0.22 \times 10^{-3}$ to $\epsilon_h = 8.1 \times 10^{-3}$ for a Gaussian distribution [2].

The first observation is that the trapping has globally the same aspect for each combination of the parameters: above a certain threshold (around $\epsilon_H \approx 0.25 \times 10^{-3}$, see section 6.4 for more details) the trapping fraction start to rise to attain an almost asymptotic behavior around 20%.

Indeed, for small emittances the beam is very concentrated close to the origin where the islands start to grow. But close to the origin, when we cross the resonance with $\nu = .25$, even if we have a very slow tune variation, the fixed points motion (and then the motion of the islands) cannot be slow enough compared to the motion of the particles which is locked due to the resonance. Therefore we have a non-adiabatic motion and the trapping probability of the particles is reduced compared to the trapping probability further from the origin. This explains why the trapping is close to zero for small emittances. For larger emittances this explains why the trapping fraction increases.

[2] These emittances refer to phase space area in the normalized Courant-Snyder coordinates and are thus adimensional.

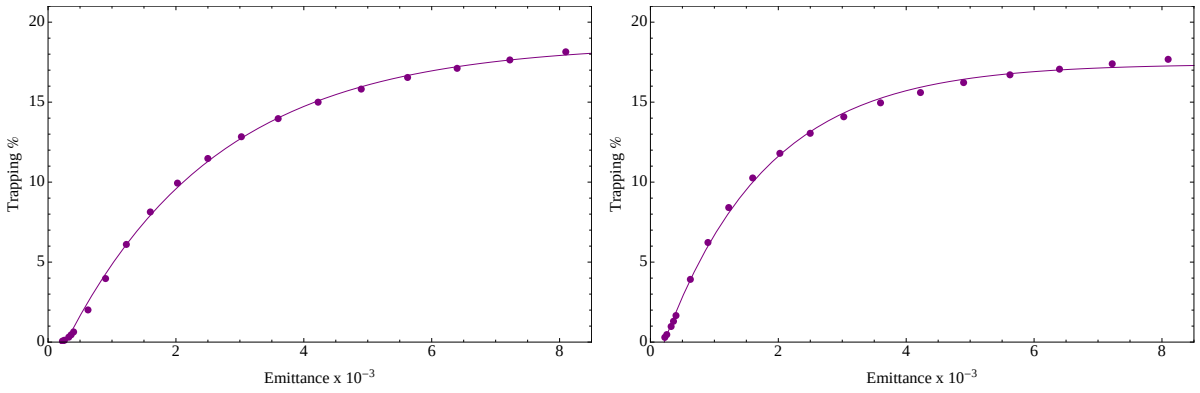

(a) $\kappa = -1.1$, 5000 turns.

(b) $\kappa = -1.9$, 5000 turns.

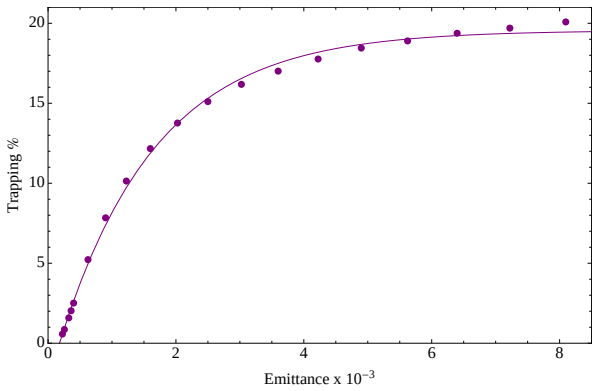

(c) $\kappa = -1.1$, 15000 turns.

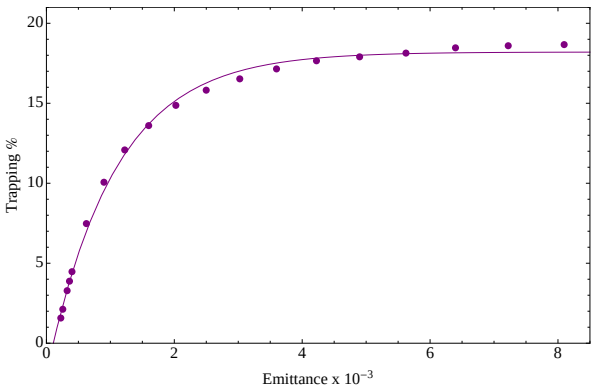

(d) $\kappa = -1.9$, 15000 turns.

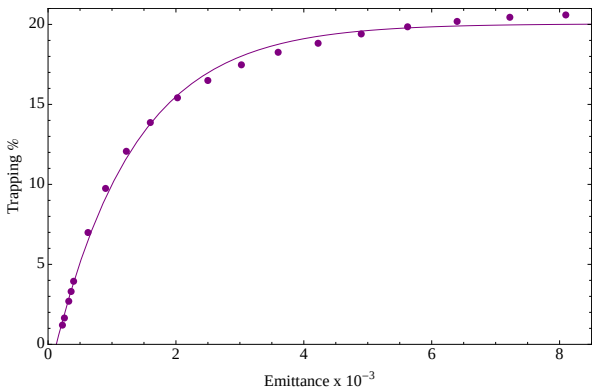

(e) $\kappa = -1.1$, 25000 turns.

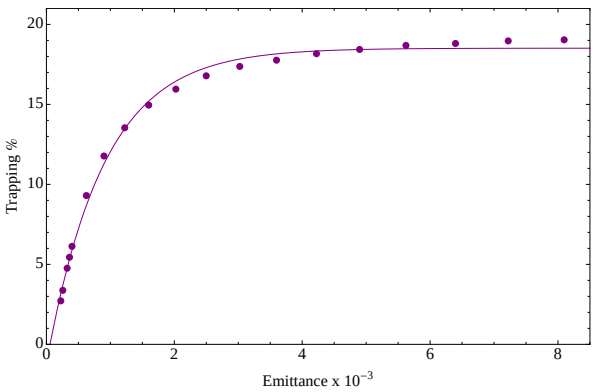

(f) $\kappa = -1.9$, 25000 turns.

Figure 6.2: Trapping fraction of a Gaussian beam distribution for different values of the number of turns and values κ. The points represent the simulated results.

We conclude that the trapping can be improved if more particles cross the separatrix when they are further away from the origin as it is the case when the emittance is increased. However a "saturation" for emittances around 6×10^{-3} is observed. This can be explained if one consider the fact that for a given number of turns the adiabaticity is restored at some distance from the origin, and when the process is adiabatic the trapping is improved but it has to stay around

20% because the resonance is stable and so one cannot completely deplete the core. This lead to the conclusion that there exists an area around the origin where there is no trapping. We investigate this phenomena in more details in section 6.4.

Fits of the trapping fraction as a function of the emittance

Based on these observations we tried to find an analytical form able to fit the data. An exponential-like form such as $A\left(1-e^{-B\epsilon_H}\right)+C$ would be able to model the observed behavior except in certain cases. In some cases a polynomial behavior would be more suited to describe the results for small emittances due to the very small derivative of the curve near the origin. Our strategy was then to try the following form:

$$A\left(1-e^{-B\epsilon_H^n}\right)+C, \tag{6.2}$$

where n should be obtained from a polynomial fit of the data for small emittances. In order to obtain the value of n we fitted the first few points with Ax^n+B. This would allow having a good polynomial fit near the origin coming from the Taylor expansion of the exponential and also a good modeling of the asymptotic behavior. But it should also be noted that this procedure is expected to be very sensitive to the number of points considered in the polynomial fit.

The results for the fits obtained with this technique are shown in figure 6.3 and compared to fits where we set $n=1$ (dashed fit, referred to as "simple exponential fit") for four different combinations of κ and of the number of turns. As expected, when the slope close to the origin is non-zero, the parameter n is equal to 1 and the two fits are the same. In the cases where the slope is small close to the origin, we see that neither of these fits reproduce correctly the behavior, even if the fit with $n \neq 1$ is slightly better. In addition when we applied this to the complete set of our simulation results we found that the fit with the polynomial leads to the case $n \neq 1$ only in a very few cases [3]. Finally looking at figure 6.4, where the whole range of emittances is shown, we observe that the fits with $\neq 1$ are worse for large emittances.

We therefore conclude that the most reasonable global analytical form to fit the data is given by the ("simple exponential fit")

$$A\left(1-e^{-B\epsilon_H}\right)+C. \tag{6.3}$$

This form allows reproducing globally the aspect of the trapping fraction in the vast majority of the explored cases. Of course if one wants to concentrate on one region (*e.g.* small emittances) or the other (*e.g.* large emittances) it is possible to use a polynomial fit close to the origin and the exponential one for larger emittance values. An example using a polynomial fit of order 2 for the small emittances data points is shown in figure 6.5, in comparison with the fit from equation 6.3.

6.2.3 Comparison between a Gaussian and a uniform beam distribution

Similar results can be obtained for the case of a uniform beam distribution. Figure 6.6 compare the behavior of Gaussian and uniform beam distributions. We fitted the data for the uniform distribution with the same analytical form as for the Gaussian case (equation 6.3).

[3] Trying different number of points for the fit used to find the parameter n did not allow to find a real optimal value

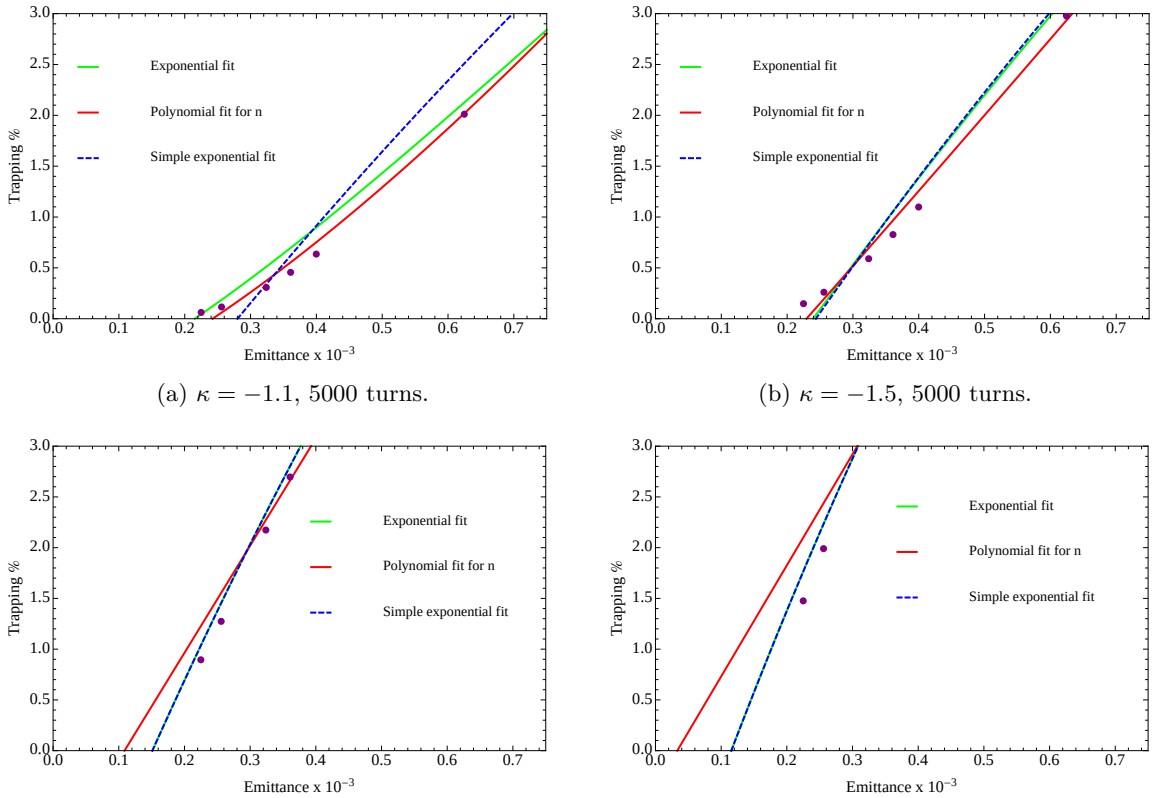

(a) $\kappa = -1.1$, 5000 turns.

(b) $\kappa = -1.5$, 5000 turns.

(c) $\kappa = -1.1$, 20000 turns.

(d) $\kappa = -1.5$, 20000 turns.

Figure 6.3: Zoom of the trapping fraction for small emittances and comparison of the different fits.

The behavior for low emittances is similar in both cases although in the uniform case we observe that the slope of the trapping fraction for low emittances is always non-zero. Indeed, the main difference between the two distributions if the presence of sharp edges in the uniform case and tails of particles in the Gaussian case. Therefore if the uniform beam is located inside the no-trapping region no trapping at all can occur but for a Gaussian beam we can have a very small trapping due to the tails of the distribution.

For larger emittances we observe the same "saturation" but the trapping fraction is lower. This can be explained with the same argument about the sharp edges of the distribution.

It is interesting to conclude that the two distributions behave similarly and to observe the effects of the edges of the distribution. Indeed, we want to find general conclusions that can be applied to a general beam, whose distribution can be approximated to be Gaussian or uniform depending on the cases. Therefore we are confident that the results analyzed bellows are rather general. In addition the use of a uniform beam distribution in the simulation allows to get rid of the effects of the tails of the distribution as we shall do in section 6.4 to determine the no-trapping area surrounding the origin.

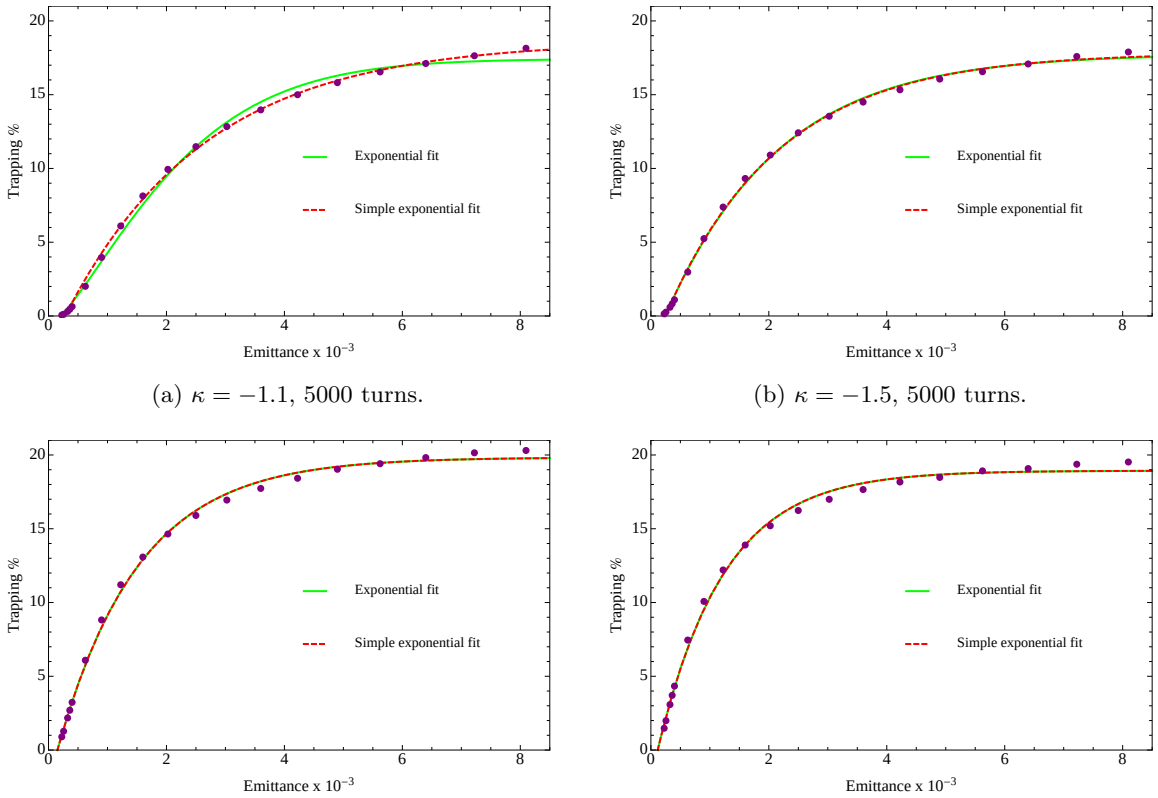

(a) $\kappa = -1.1$, 5000 turns.

(b) $\kappa = -1.5$, 5000 turns.

(c) $\kappa = -1.1$, 20000 turns.

(d) $\kappa = -1.5$, 20000 turns.

Figure 6.4: Comparison of the fits from equation 6.2 (purple) and 6.3 (green).

6.2.4 Effect of the slope of the tune variation

As already shown in the previous section, the number of turns defining the duration of the resonance crossing influence the trapping fraction. We analyze here the results obtained for different number of turns, scanning over the initial emittance and for different values of κ. The tune varies from 0.25 to 0.245 over 5000 to 25000 turns.

A variation of the number of turns is then equivalent to a reduction of the slope of the tune variation. Figure 6.7 shows various tune curve used in these simulation, keeping the variation linear and varying the number of turns. Figure 6.8 summarize the results obtained for κ equal to -1.2, -1.5 and -1.9 for both Gaussian and uniform distributions.

The first observation is the increase of the trapping fraction with the number of turns that we can observe for any value of the emittance or κ. A second important observation is the reduction of this gain for increasing emittance; and consequently that the difference in the asymptotic-like behavior is rather small. Both of these can be explained by the argument of the increase of adiabaticity: indeed, for a higher number of turns or equivalently a small slope of the tune variation, the motion of the fixed points and separatrices is slowed down and it appear slower compared to the motion of the particles therefore increasing the adiabaticity of the process. This explanation is also compatible with the second observation: indeed, for larger emittances the trapping occurs for more particles when they are away from the origin, *i.e.* in a situation where the adiabaticity is already increased. The gain is thus lower.

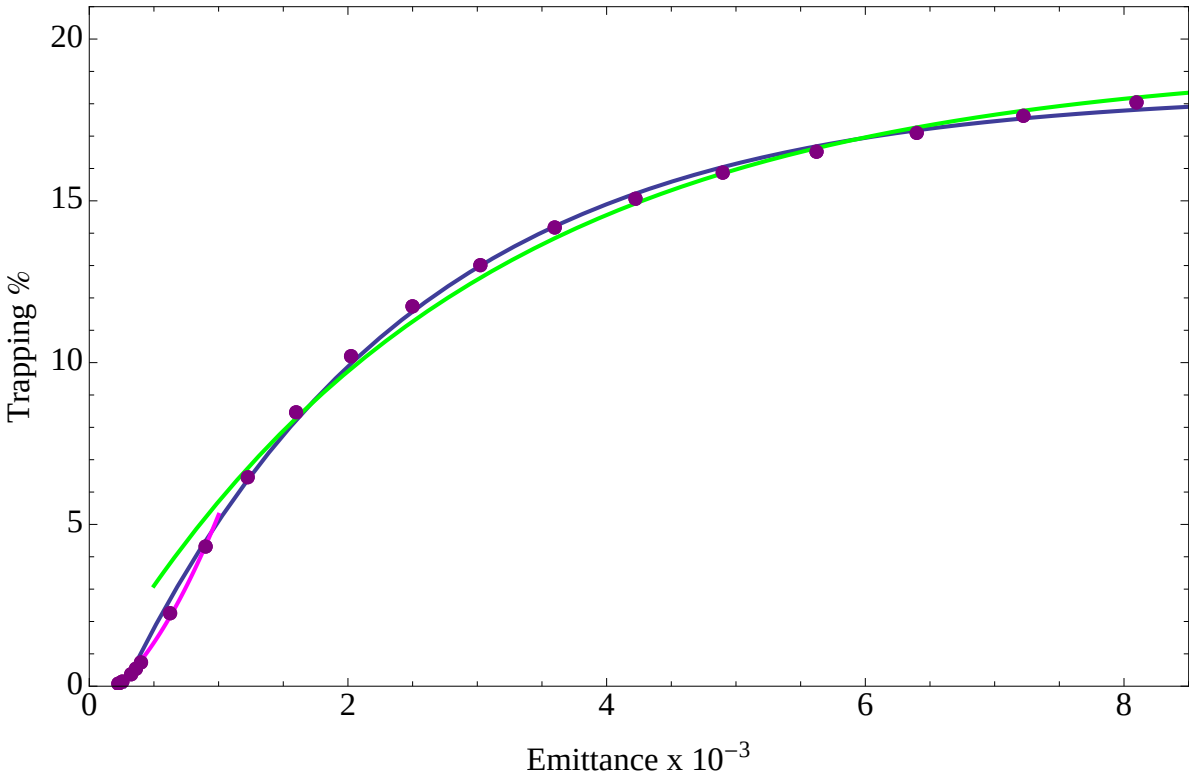

Figure 6.5: Purple is the global fit from equation 6.3, pink is a polynomial fit of the first points and green is a fit from equation 6.3 but excluding the points concerned by the polynomial fit.

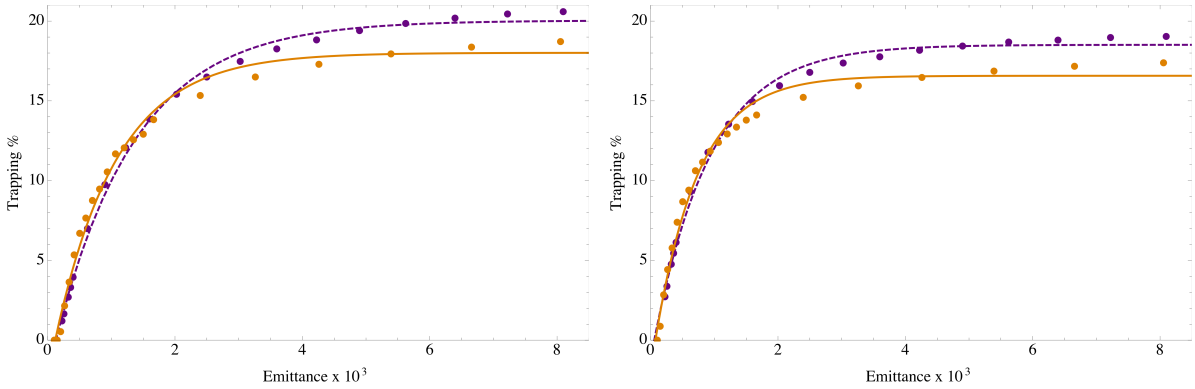

(a) $\kappa = -1.1$, 25000 turns.

(b) $\kappa = -1.9$, 25000 turns.

Figure 6.6: Trapping fraction for different values of the initial emittances for a Gaussian distribution (purple) and for a uniform distribution (orange).

The gain in the trapping fraction with respect to the increase of the number of turns becomes lower for larger number of turns also confirming this hypothesis. In addition this behavior seems to be globally independent on the value of κ.

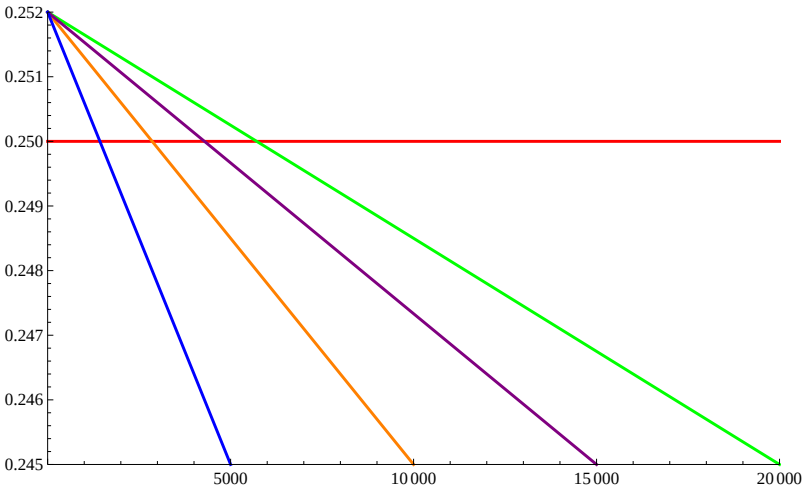

Figure 6.7: Tune variation for simulations with different number of turns.

6.2.5 Effect of the functional form of the tune variation

According to the argument of adiabaticity we can also try to improve the trapping using a small slope for the tune curve where we are far from an adiabatic process, *i.e.* for a tune close to the resonant value, and then to increase the slope when the adiabaticity is better, thus keeping the total number of turns constant, allowing to move the islands to the desired location in the same number of turns. To do that we performed simulations with a polynomial tune variation.

In these simulations, we first approached the resonant tune with a linear variation over a fixed number of turns, then after the resonant value we used a second order polynomial having a zero slope close to the resonant tune to reach the final tune value. We performed these simulations keeping the total number of turns constant and the final tune value constant. This allows comparing the trapping fraction in the same conditions, as the topology is the same at the end of the process.

Figure 6.9 compare the results obtained with such a tune curve with the linear case, for equal total number of turns. We observe a clear gain that confirms the argument of increased adiabaticity. In addition the gain is higher for small (in absolute value) values of κ and this also confirm our argument, as the islands move further from the origin for weak nonlinearities (see section 6.2.6).

6.2.6 Effect of the value of κ

We analyze in this section the effect of the value of κ during the trapping process. Figure 6.10 shows the results obtained as a function of the initial emittance, for four different number of turns.

A general result can be seen, independently on the number of turns: small values of κ (in absolute value) improve the trapping fraction for large emittances but reduce it for smaller emittances. In addition, the value of the emittance for which the trapping is independent on κ becomes smaller for increasing number of turns.

To understand this we have to consider the phase space topology for different tunes and value of κ. Figure 6.11 displays the phase space topology for $\kappa = -1.1$ and $\kappa = -1.9$ for the

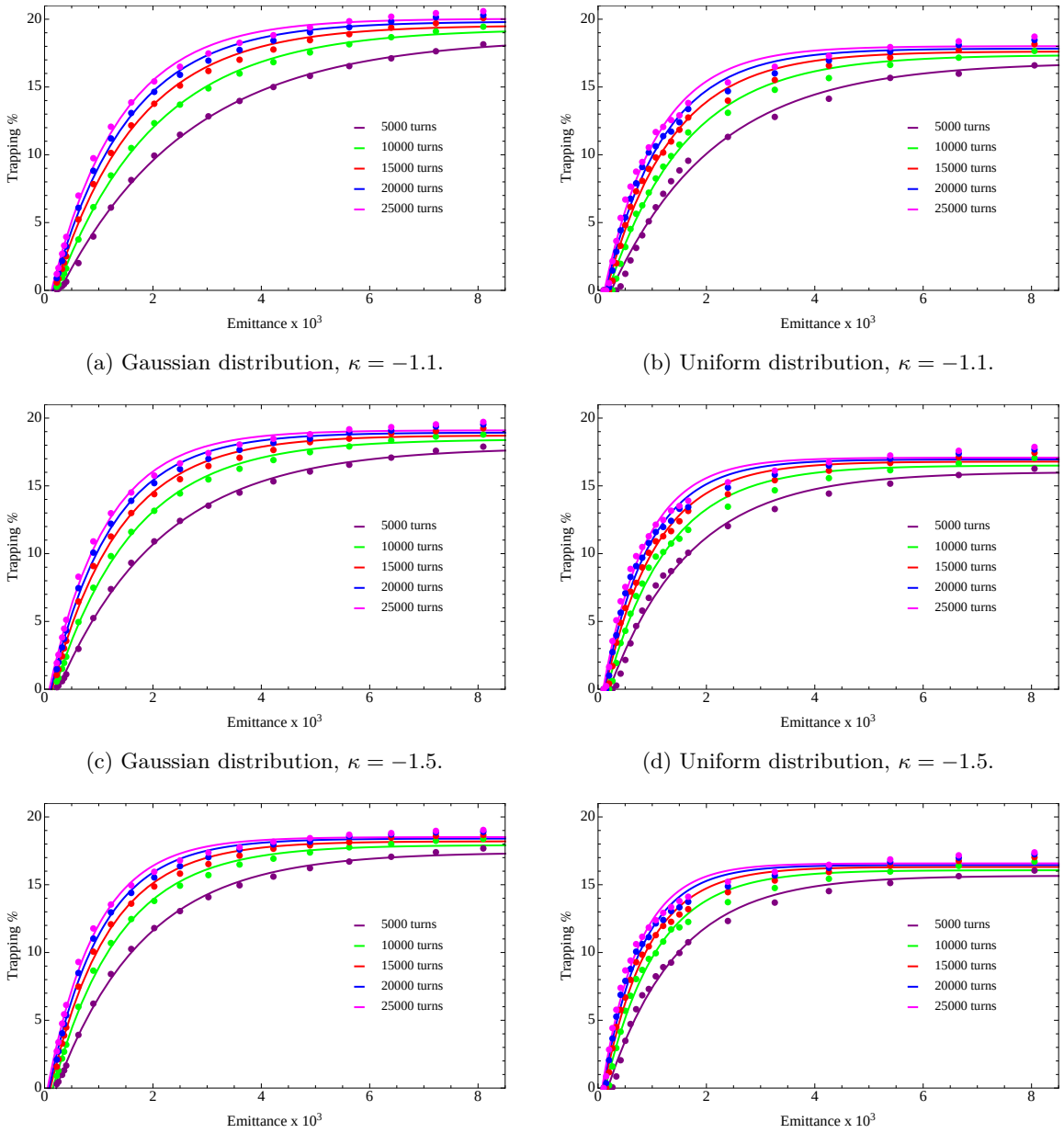

(a) Gaussian distribution, $\kappa = -1.1$.

(b) Uniform distribution, $\kappa = -1.1$.

(c) Gaussian distribution, $\kappa = -1.5$.

(d) Uniform distribution, $\kappa = -1.5$.

(e) Gaussian distribution, $\kappa = -1.9$.

(f) Uniform distribution, $\kappa = -1.9$.

Figure 6.8: The plots show the results obtained for different number of turns, scanning over the values of κ. The trapping fraction systematically increase with the number of turns.

tunes 0.249 and 0.245 corresponding respectively to the very start of the capture process and to the end of the trapping and islands' displacement.

We observe that, for a given tune, for $\kappa = -1.9$ the islands are closer to the origin than for $\kappa = -1.1$. This first fact can explain why the trapping of a small emittance beam is reduced for small values of κ: the emittances are moving faster from the origin and therefore the adiabaticity of the process is worse than for higher values of κ, especially close to the origin

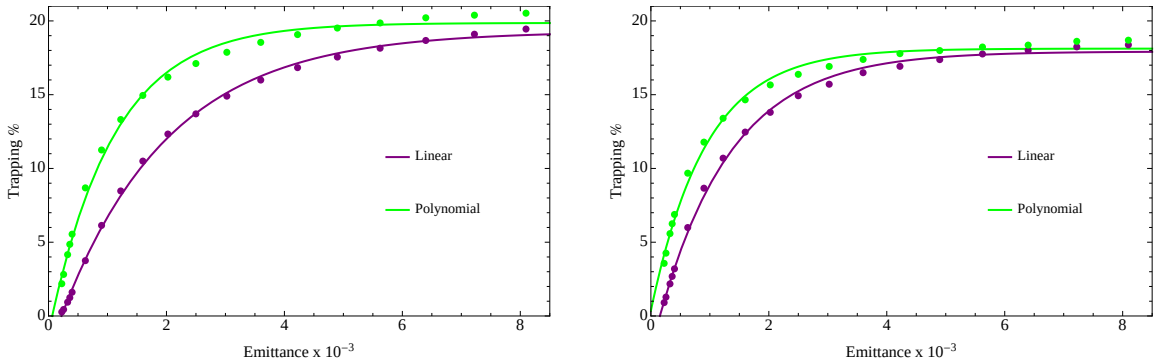

(a) $\kappa = -1.1$. (b) $\kappa = -1.9$.

Figure 6.9: Gain in the trapping fraction using a tune curve where the slope is equal to zero at the resonance crossing (for two values of κ).

where the beam is located. But at the same time, for a small value of κ, the islands will go completely through a large emittance beam. This is not the case for a large value of κ because the islands stay close to the origin. Let us consider a large beam [4] whose Gaussian distribution has a mean deviation $\sigma = 0.09$, corresponding to an emittance of $\epsilon = 8.1 \times 10^{-3}$. If $\kappa = -1.9$, this beam will have a size of the same order as the outer separatrix of the bottom right plot of figure 6.11. Therefore even if this value of κ will increase the trapping for particles close to the origin due to the good adiabaticity, the density of the beam at that location is lower compared to a smaller beam. More importantly, the particles with large amplitudes may not see the separatrix crossing, as even for the final tune the islands are located at smaller amplitudes. These particles can therefore not be trapped but they are still inside the separatrix linked to the origin so they are not lost.

We thus identified to competing mechanisms: large values of κ increase the adiabaticity and thus enhance the trapping for beams with a large density at small amplitudes and small values of κ allow the islands and their separatrices to move far from the origin thus trapping more efficiently beams with large emittance. These two mechanisms explain why some emittances have a trapping independent from the value of κ: for these emittances the two mechanisms are cancelling each other.

As the first argument concerns the adiabaticity we can also understand why the special emittance value is reduced with the number of turns: for large number of turns the adiabaticity is increased thus lowering the benefit of the effect of large κ on the adiabaticity close to the origin.

We do not detail simulations obtained for a uniform beam distribution as the results and conclusions are the same.

Effect of a variation of κ during the trapping process

In addition to the results obtained for a constant value of κ it is also interesting to consider a variation of κ during the trapping process. In the next simulations, we considered specific variations of the parameter κ. We start the variation of κ at the resonance crossing and we let

[4] This is the largest beam considered in the above discussed results.

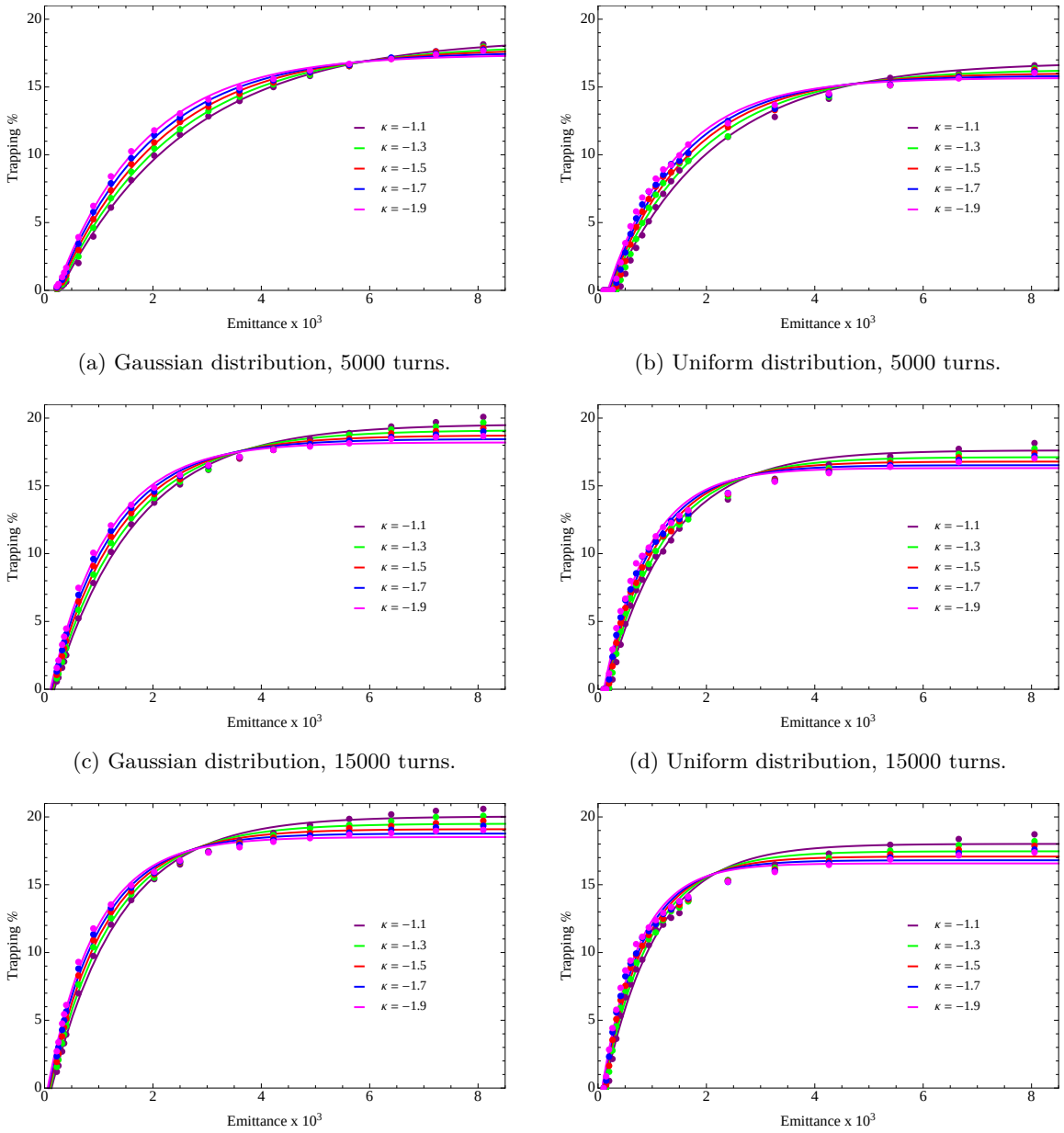

(a) Gaussian distribution, 5000 turns.

(b) Uniform distribution, 5000 turns.

(c) Gaussian distribution, 15000 turns.

(d) Uniform distribution, 15000 turns.

(e) Gaussian distribution, 25000 turns.

(f) Uniform distribution, 25000 turns.

Figure 6.10: Results obtained for five different values of κ. The number of turns is different for each plots, we also compare Gaussian and uniform distributions.

it evolve so that it reaches its final value at the end of the process. For this study we considered only a Gaussian beam distribution.

We considered a polynomial evolution with a polynomial of order 2 and a linear variation but no notable differences were found. Therefore in the following we consider only a linear evolution of κ.

Figure 6.12 presents the results. Figure 6.12 (a) is a case where $\kappa = -1.5$ at the resonance

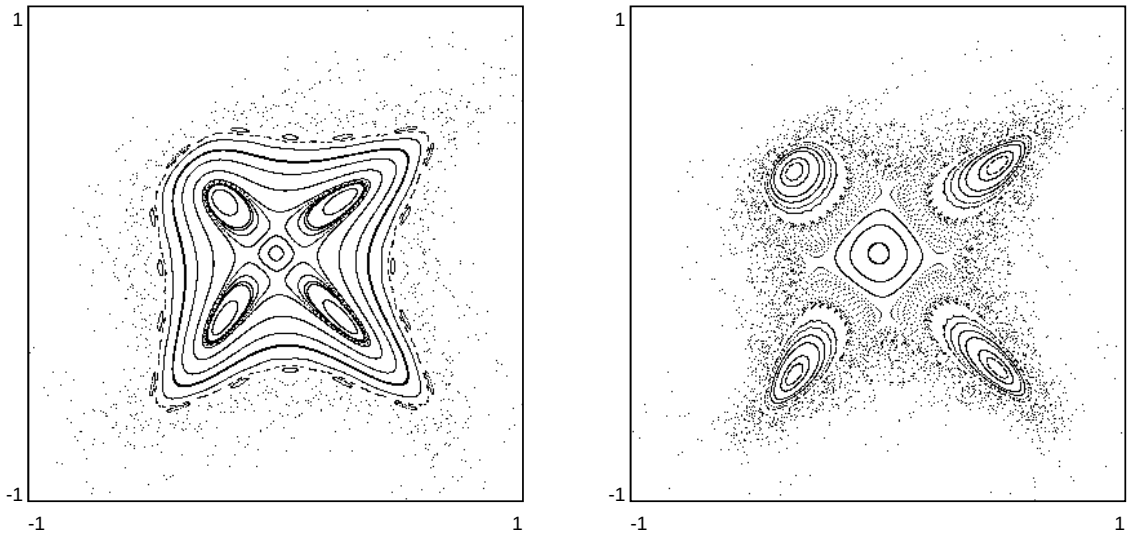

(a) $\kappa = -1.1$ and $\nu = 0.249$.

(b) $\kappa = -1.1$ and $\nu = 0.245$.

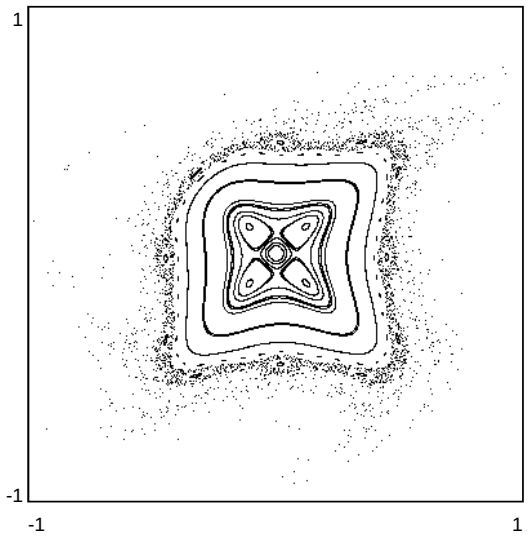

(c) $\kappa = -1.9$ and $\nu = 0.249$.

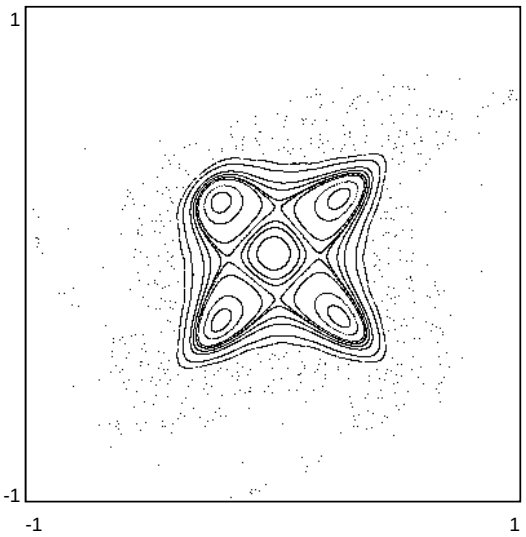

(d) $\kappa = -1.9$ and $\nu = 0.245$.

Figure 6.11: Phase space topology of the generalized Hénon mapping obtained with GIOTTO [**?**].

crossing and we compare variations where it stays constant, goes to -1.1 or to -1.9. We observe no noticeable differences and the same for figure 6.12 (b) where the variations are such that $\kappa = -1.9$ at the resonance crossing with κ going to -1.1 at the end of the process.

We conclude that the value of κ only influences the trapping close to the resonance, *i.e.* when the islands are close to the origin and when the adiabaticity is not well preserved. As the islands move from the origin, the trapping "per turn" becomes lower and the effect of κ only affect the topology of the phase space and the position and size of the islands at the end

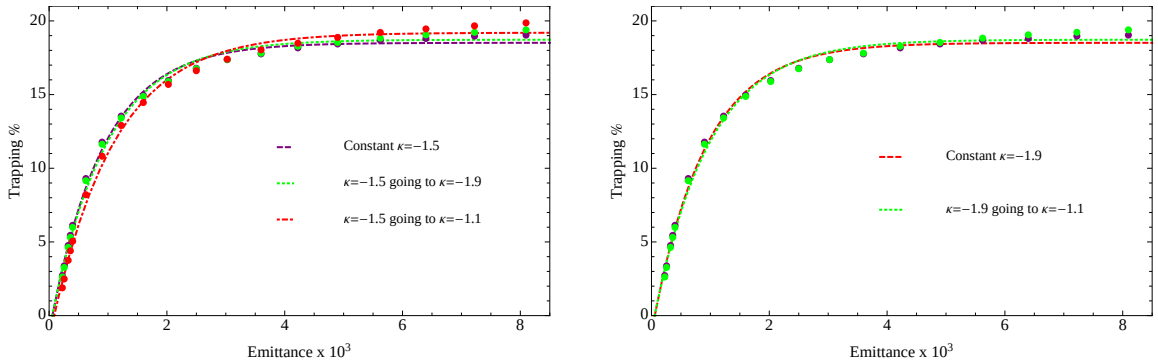

(a) $\kappa = -1.5$ at resonance crossing.

(b) $\kappa = -1.9$ at resonance crossing.

Figure 6.12: Trapping fraction for different variations of κ during the process.

of the process.

This opens the way for an optimization where κ could be set at the resonance crossing to a value maximizing the trapping and where it could evolve to a final value maximizing the separation of the islands.

6.3 Global fitted model of the trapping fraction

Now that we investigated the effects of the major parameters we can try to obtain a global model of the trapping fraction as a function of the parameters based on the fits obtained for each cases. We try here to obtain a model of the trapping fraction that is valid for the large emittance region, thus neglecting the small region where the slope can be close to zero in some cases. As we shall see, this allows obtaining a correct and simple model of the process.

We built this model for a Gaussian beam distribution where the splitting is done using a linear tune variation.

We try to obtain the following function:

$$T\left(\epsilon, \kappa, \frac{\Delta\nu}{\nu}\right) = A\left(\kappa, \frac{\Delta\nu}{\nu}\right)\left[1 - e^{-B\left(\kappa, \frac{\Delta\nu}{\nu}\right)\left(x - C\left(\kappa, \frac{\Delta\nu}{\nu}\right)\right)}\right]. \tag{6.4}$$

The functional form of the parameters A, B and C can of course be chosen such that the model perfectly reproduces the results. Nevertheless we show that the following simple parametric form is able to reproduce the results with a good accuracy:

$$A(\kappa, N) = \left(a\sqrt{N} + b\right)(\alpha + \beta\kappa); \tag{6.5}$$

$$B(\kappa, N) = (aN + b)(\alpha\kappa + \beta); \tag{6.6}$$

$$C(\kappa, N) = (aN + b)(\alpha\kappa + \beta), \tag{6.7}$$

i.e. the parameters A, B and C are linear in the number of turns and κ, except for the square root dependency of A in the number of turns.

Fitting this model with our complete set of results [5] allowed to build the model [6].

[5] The fit was done with simulation data for κ going from -1.1 to -1.9 by steps of 0.1 and for the number of turns going from 5000 to 25000 by steps of 5000 turns.

[6] The complete results and the general model are available as Mathematica functions.

Figure 6.13 compares the fits obtained with the global model with the results and their individual fits.

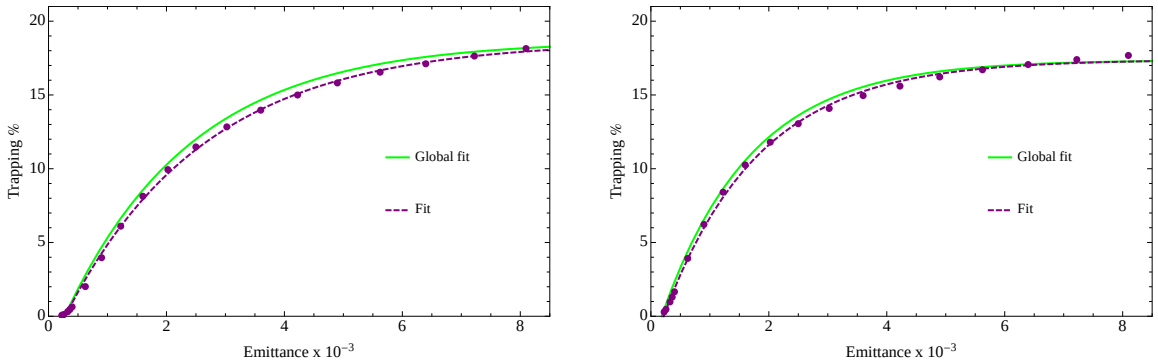

(a) 5000 turns, $\kappa = -1.1$.

(b) 5000 turns, $\kappa = -1.9$.

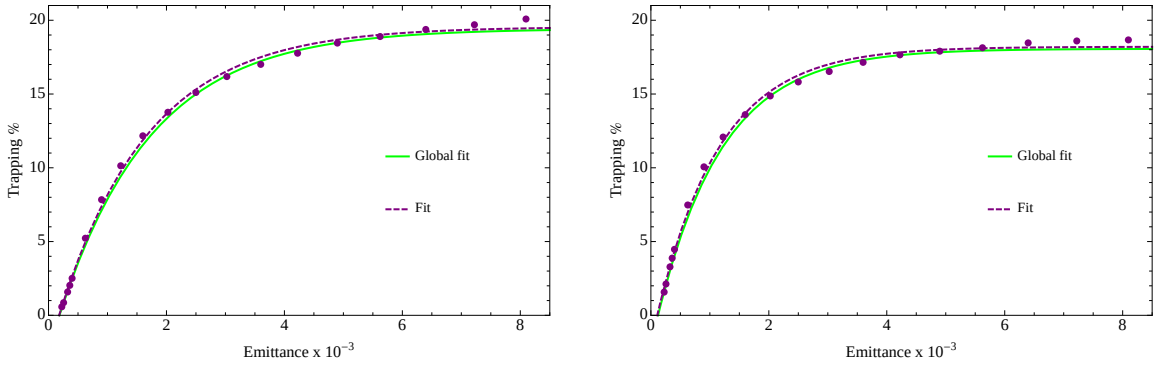

(c) 15000 turns, $\kappa = -1.1$.

(d) 15000 turns, $\kappa = -1.9$.

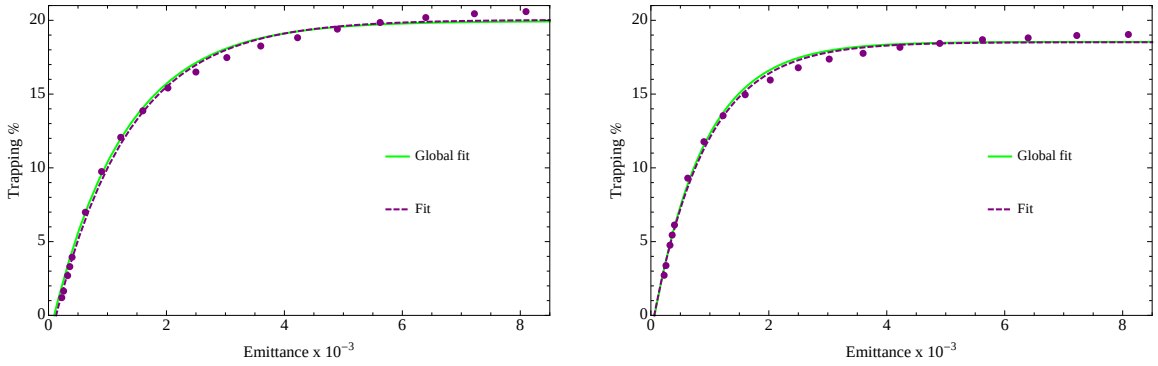

(e) 25000 turns, $\kappa = -1.1$.

(f) 25000 turns, $\kappa = -1.9$.

Figure 6.13: Comparison between the global fit of equation 6.4 and the individual fit for different values of κ and the number of turns.

We observe a good agreement even for the almost linear model that we used; the results being slightly worse for a small number of turns.

6.4 Minimal trapping amplitude

As mentioned above, it is possible to define a minimal amplitude below which no trapping will occur. Again this can be understood as a zone in phase space where the growth of the islands is too fast (thus very close to the origin) and where the trapping probability for individual particles is close to zero.

To investigate this region and its dependence on the other parameters we use a uniform beam distribution and we use a fit of the results to find the zero of the trapping fraction. We tried different fits to correctly obtain this amplitude and we finally also choose to use an exponential fit (equation 6.3) which, for uniform beam distribution correctly model the behavior for low emittances (thus at low amplitudes). We observed on a large set of results that this fit correctly interpolates the behavior of the trapping fraction for the smallest simulated emittances to zero.

The minimal trapping amplitude obtained as a function of the number of turns and for different values of κ are presented in figure 6.14. We fitted the results as a function of the number of turns with an exponential $A\left(e^{-Bx}\right) + C$.

This fit allows extracting an asymptote that represents the absolute limitation for the minimal trapping amplitude: even for a very large number of turns (thus trying to restore the adiabaticity close to the origin) no trapping will occur for smaller amplitudes. This asymptote is shown in figure 6.14 for three values of κ.

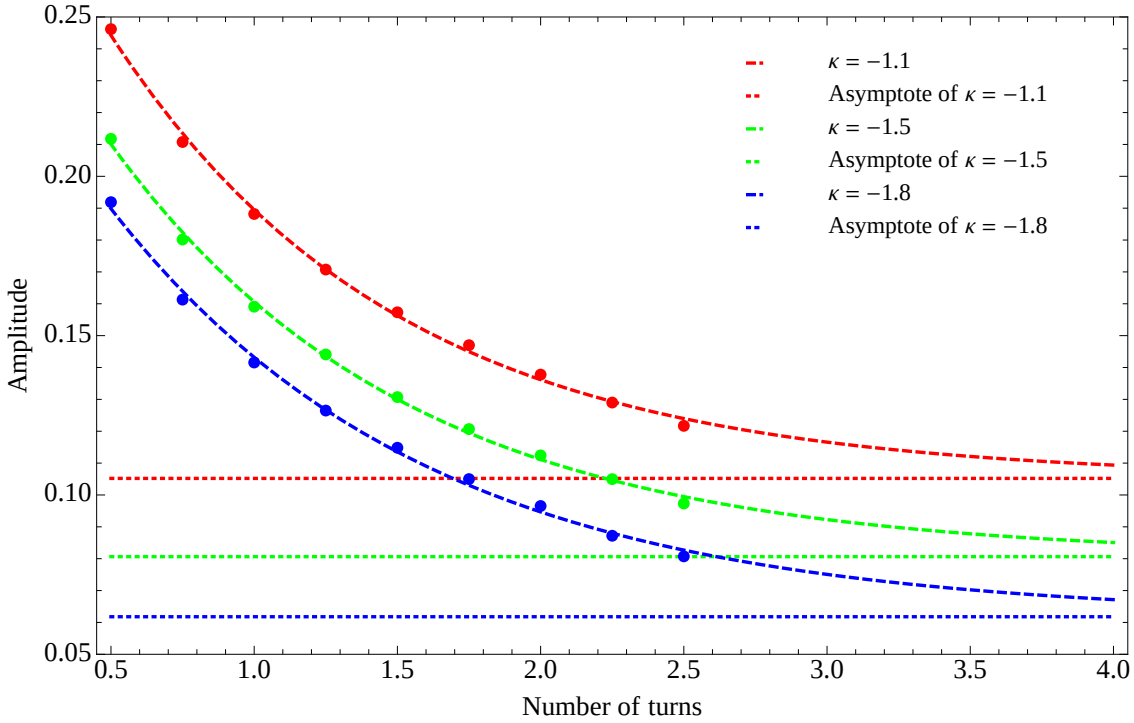

Figure 6.14: Zero of the trapping as a function of the number of turns and exponential fit. The figure also displays the asymptote of the exponential fit. Three values of κ are compared

6.5 Parametric dependence of the emittance sharing between the beamlets

Apart from the trapping fraction, another important output of our simulations is the emittance sharing between the islands and the core. Indeed, after the splitting, the emittances of each beamlets have to be considered: the beam is split into different parts and the initial emittance will be shared between the core and the islands.

6.5.1 Islands and core emittances ratio

First we define two quantities: the *core emittance ratio* and the *island emittance ratio*. The core emittance ratio is the ratio of the emittance of the core at the end of the process by the initial emittance of the beam. The island emittance ratio is defined in the same way: it is the ratio of the emittance of one island at the end of the process by the emittance of the initial beam.

As the beam is divided in five parts, one could hope to obtain a perfect sharing of the emittance leading to a core and island emittance ratio of 20% each. We shall see that this is not what we obtain in all cases.

Figure 6.15 shows the emittance ratio for the core and the islands for different values of the number of turns and κ. We also included the trapping fraction to put in relation the trapping and the emittance sharing.

The results show that asymptotes seem to be present for the emittance ratio and we therefore tried to fit the results with an appropriate analytical function. We found that good results are obtained with a fit for the core emittance ratio of the form

$$Ae^{-Bx} + C, \tag{6.8}$$

and of the form

$$\frac{A}{x^C} + B \tag{6.9}$$

for the island emittance ratio. These fits are also displayed in figure 6.15.

If we analyze the results and the asymptotes of the fits, we observe similar behaviors for the different number of turns and we can observe that an increase of the number of turns tends to reduce the emittances. This can be understood as an effect of the crossing of the separatrices: if the motion of the separatrices is slower, the motion of the particles close will be less perturbed by the crossing and therefore no emittance increase will occur (for example for the particles with low amplitudes in the core).

Furthermore, important conclusions come from the comparison of the different values of κ. For the island emittance ratio we clearly observe a large difference between the two extreme values of κ: for $\kappa = -1.1$, it is observed that the ratio is around 40%, even for the large emittances where the asymptote of the trapping fraction is already obtained. In addition, for that value of κ, the core emittance ratio is below 20 % for large emittances. In contrast, for $\kappa = -1.9$, the island emittance ratio and the core emittance ratio tend to be almost equal and close to the "perfect" value of 20 %.

These behavior can be understood from the phase space topology of figure 6.11 (6.11 (b) displays the phase space topology for $\kappa = -1.1$ while 6.11 (d) is for $\kappa = -1.9$). This topology will be reproduced by the beam distribution at the end of the simulation. Figure 6.16 shows this

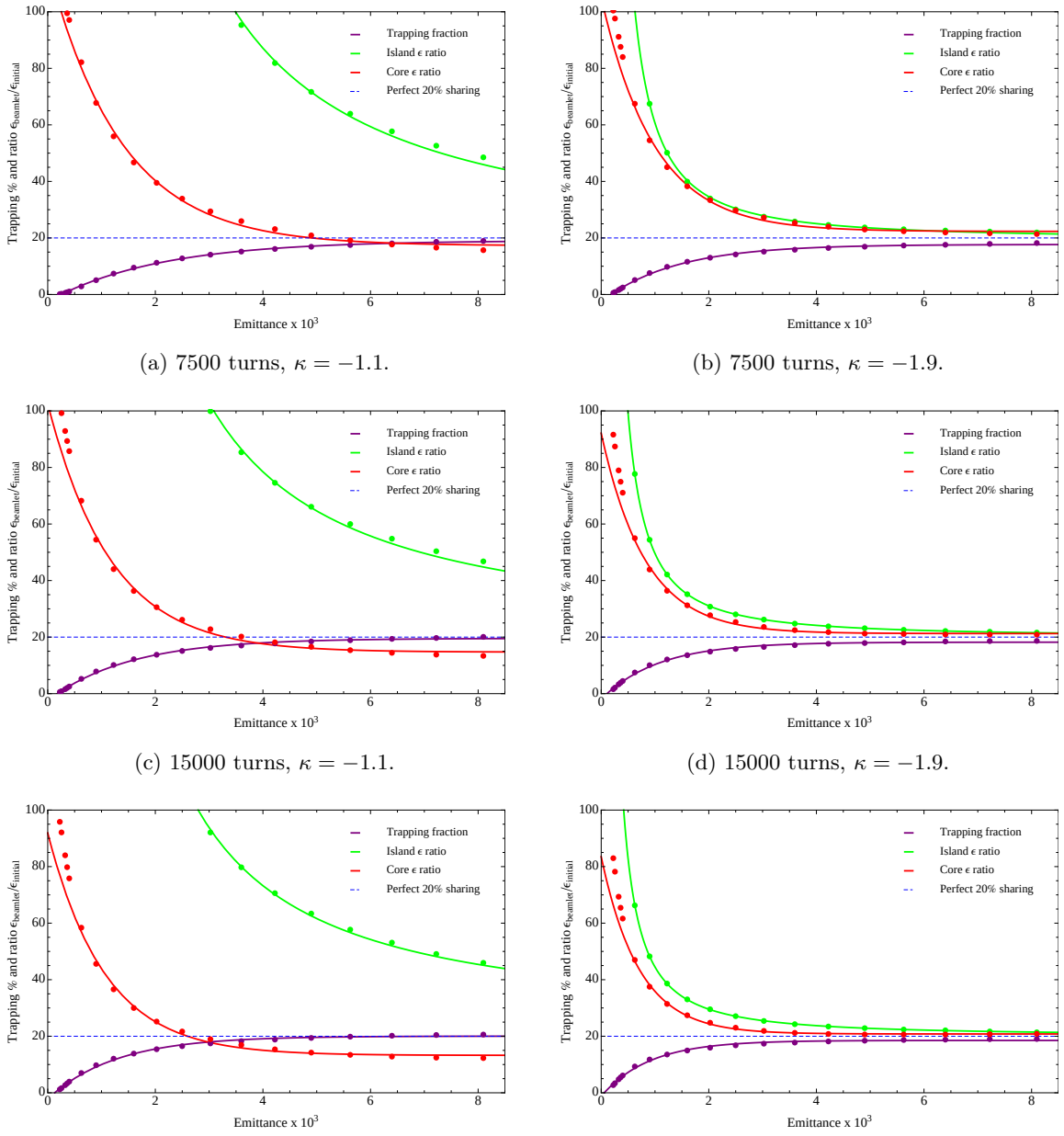

(a) 7500 turns, $\kappa = -1.1$.

(b) 7500 turns, $\kappa = -1.9$.

(c) 15000 turns, $\kappa = -1.1$.

(d) 15000 turns, $\kappa = -1.9$.

(e) 25000 turns, $\kappa = -1.1$.

(f) 25000 turns, $\kappa = -1.9$.

Figure 6.15: Emittance ratio for the core and one island for different values of the number of turns and κ. The trapping fraction is also shown.

beam distribution (the histogram 6.16 (a) displays the case $\kappa = -1.1$ while 6.16 (b) displays the histogram for $\kappa = -1.9$).

We observe in these figures that the beam distribution is more concentrated near the center of the islands for $\kappa = -1.9$ than for $\kappa = -1.1$ thus leading to a smaller emittance for $\kappa = -1.9$. On the other hand the core distribution is closer from the origin for $\kappa = -1.1$.

We conclude that κ, even if it also affects the trapping fraction, has an effect mainly on the

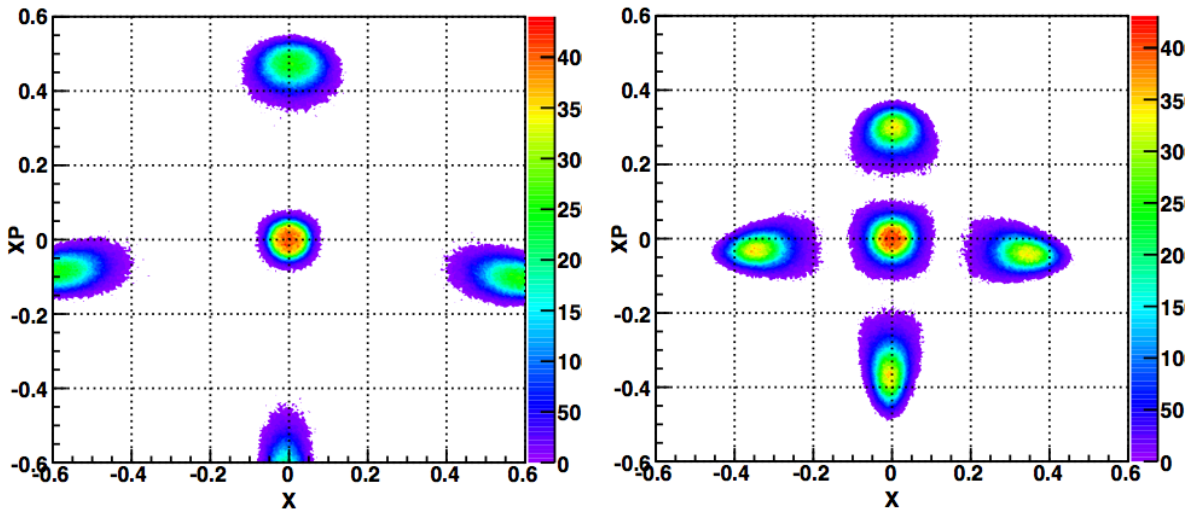

(a) 25000 turns, $\kappa = -1.1$.

(b) 25000 turns, $\kappa = -1.9$.

Figure 6.16: Histograms of the final beam distributions obtained for two different values of κ.

core and islands emittances. With a larger number of turns (*e.g.* 25000) and $\kappa = -1.9$, it is possible to obtain an emittance sharing nearly equal to 20%.

Despite this interesting conclusion, it should be noted that such a value for κ leads to a smaller separation between the islands and the core for equal final tunes (see figure 6.11 (b) and (d)). A smaller separation is less favorable for the extraction itself because it leaves less space for the septum blade.

Another important comment about figure 6.15 concerns the behavior of the emittance ratio for small initial beam emittances. We observe rather large values and even in some cases (mainly for small values of κ) the ratio is bigger than 100%. However this has to be put in relation with the trapping fraction obtained for these emittances: the trapped particles are scattered randomly inside the islands leading to a large statistical emittance which in case of small initial beam emittance can give an emittance ratio larger than 100%.

6.5.2 Tune curve slope effect on the emittance sharing

We already discussed the impact of the functional form of the tune variation on the trapping fraction in section 6.2.5. In this section we shall analyze the effect on the emittance sharing: we compare results obtained with a linear resonance crossing and results where the crossing is done with a polynomial tune curve with a slope equal to zero at the resonant tune ($\nu_x = .25$).

Figure 6.17 shows the results obtained, for two values of the number of turns and for two different values of κ, the dotted lines are the fits of the linear case and the plain lines are obtained in the polynomial case.

We observe globally that in the polynomial case the emittance ratios of the core and of the islands are smaller than in the linear case. For $\kappa = -1.1$, this allows to obtain a very small core emittance while have a trapping fraction almost equal to 20% for large initial emittances.

Indeed, when the slope of the tune curve is zero at the resonance crossing, the adiabaticity is increased and this improves the trapping. Therefore at the same time it will reduce the number of particles crossing the separatrix and being scattered back in the core without trapping, thus

inducing emittance blow-up. As the number of particles in that case is reduced for in case of a higher trapping probability, the emittance of the core is reduced.

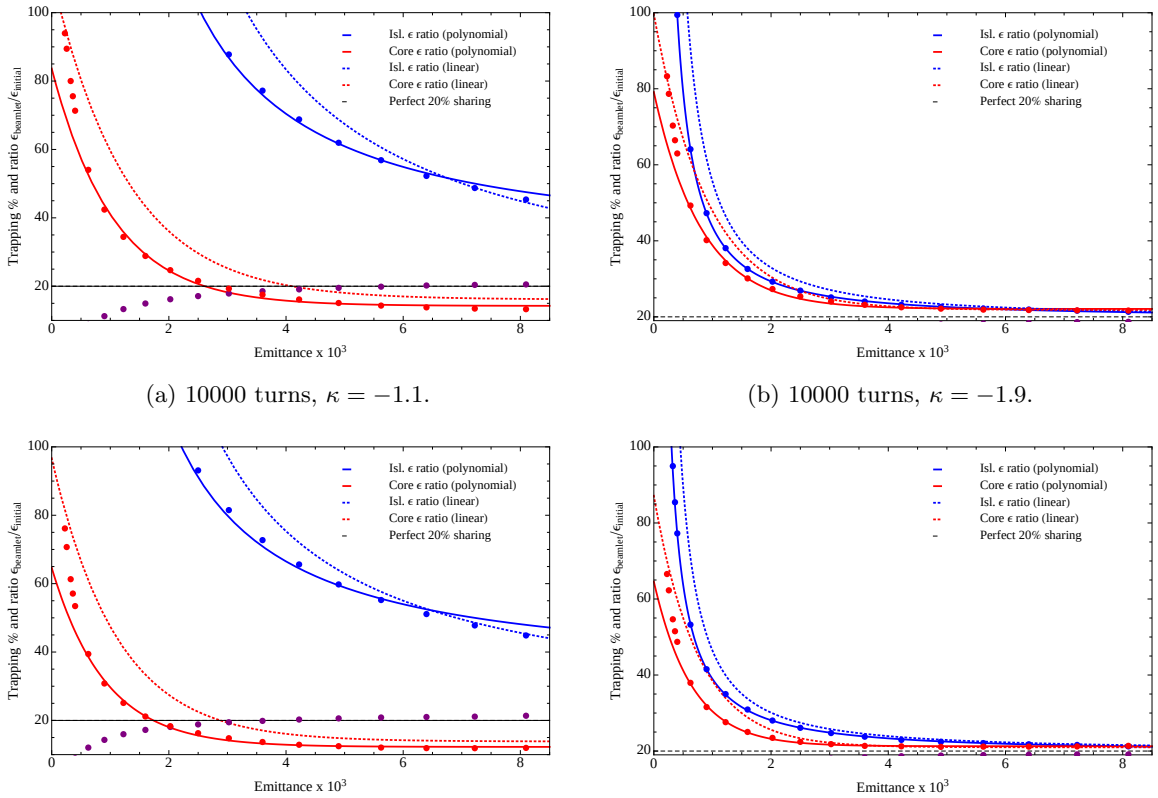

(a) 10000 turns, $\kappa = -1.1$.

(b) 10000 turns, $\kappa = -1.9$.

(c) 20000 turns, $\kappa = -1.1$.

(d) 20000 turns, $\kappa = -1.9$.

Figure 6.17: Emittance ratios comparing a polynomial tune curve with a linear tune curve.

6.5.3 Effect of the variation of κ on the emittances ratio

In this section we perform a manipulation that could allow to combine two interesting effects: on the one hand the trapping fraction is increased if one choose a small κ (in absolute value) at the resonance crossing (see section 6.2.6) while on the other hand we have seen in section 6.5.1 that a value of κ close to -1.9 reduces the emittance ratio of the islands to a value close to 20% and allows to obtain a core emittance ratio also close to 20%.

In addition in section 6.2.6 we analyzed the impact on the trapping fraction of a variation of κ during the splitting process. We concluded that the trapping depends on the value of κ at the resonance crossing, the evolution of κ to another value following the resonance crossing having almost no impact on the trapping fraction.

Based on these conclusions we performed simulations where κ evolves linearly from an initial value (at the resonance crossing) to a final value (as in section 6.2.6) so has to obtain a good value for the trapping fraction and at the same time an emittance sharing close to 20%.

Figure 6.18 displays the results in the favorable case where κ evolves from -1.1 to -1.9. The dotted lines represent the cases where κ is kept constant at values equal to -1.1 and -1.9.

We observe that our conclusions seem to be valid as we obtained the expected result: compared to the case where κ has a constant value equal to -1.1, the island emittance ratio is reduced even if it does not reach the value obtained for $\kappa = -1.9$.

The same conclusion applies to the core emittance ratio: we obtain a ratio that is between the values obtained when κ is kept constant.

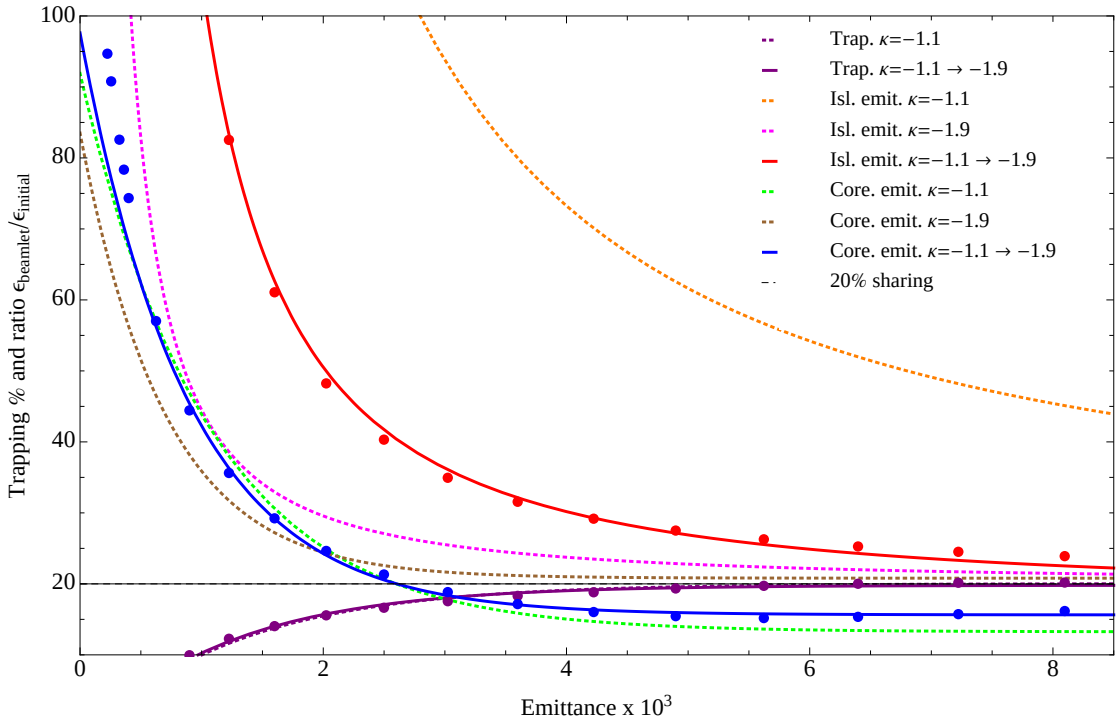

Figure 6.18: 25000 turns, variation $\kappa = -1.1 \rightarrow -1.9$.

We conclude that these results suggest that benefits in the final beam properties can be obtained with a variation of κ during the trapping process.

6.6 Conclusions on the 2D numerical studies

We obtained interesting results regarding the behavior of the process. We found that the trapping fraction can be fitted using an exponential model that reproduces correctly the results and their main behaviors (zero and asymptote). Based on these individual fits, we were able to obtain a global fitted model of the trapping fraction as a function of κ and of the number of turns.

Analyzing the effect of the number of turns, we concluded that an increase of the number of turns improves the results in all cases, the trapping fraction is increased and the emittances are reduced. We were able to link that results with explanations based on the adiabaticity of the trapping process.

We found that it is possible to further improve the trapping process while keeping the number of turns constant if one chose a tune variation with a slope equal to zero at the resonance crossing. This possibility can be exploited in parallel with other improvement methods.

The impact of κ has also been analyzed. On the one hand we found that a small value of κ (≈ -1.1) leads to an increase in the trapping fraction for large emittances but also to an increase in the emittance of the islands. On the other hand we found that a larger value of κ slightly reduces the trapping fraction for large emittances but it strongly decreases the resulting emittances.

As we observed that the effect of κ on the trapping fraction depends almost exclusively on its value at the resonance crossing, we concluded that one can optimize both the trapping fraction and the emittances using a variation of κ during the process. If one uses a small value of κ at the resonance crossing and then increases it values, it is possible to obtain a trapping fraction very close to 20% while obtaining a very good emittance sharing between the core and the islands.

Although these results are based on the simplest model of the MTE splitting we were able to find interesting conclusions, and, as we shall see, these conclusions are also valid if one use a more evolved model, such as the 4D model considered in the next chapter.

CHAPTER 7

4D numerical studies of the MTE dynamics

In this chapter we study the results obtained from 4D numerical simulations performed with Manzoni. These results concern the trapping fraction and the emittance sharing of the beamlets, but in this 4D case we also consider the impact of the vertical dimension on the beam splitting. We first review the parameters relevant to these effects in section 7.1 and then we discuss the results concerning the trapping fraction as a function of the vertical emittance in section 7.2. Then we discuss the parametric dependence of the islands' emittance in section 7.3. Finally section 7.4 analyze the vertical emittance blow-up. We conclude in section 7.6.

7.1 Numerical study of the 4D generalized Hénon mapping . . . 96
7.2 Effects of the vertical emittance on the trapping fraction . . . 97
7.3 Emittance sharing in 4D . . . 98
7.4 Evolution of the vertical emittance . . . 100
7.5 Digression: double resonance crossing . . . 100
7.6 Conclusions on the 4D numerical studies . . . 101

7.1 Numerical study of the 4D generalized Hénon mapping

These numerical studies are based on the four-dimensional generalized Hénon mapping (equation 3.5). As the beam manipulation performed during the MTE splitting concerns mainly the horizontal plane, it was natural to consider a flat beam in a first time. Nevertheless, the real process impacts both planes, as the nonlinear elements have an effect in both planes and couples the horizontal and vertical planes.

The goal of these simulations is to study the impact of the vertical emittance of the beam on the trapping process. Indeed, due to the coupling, particles with different vertical amplitudes will be subject to different horizontal dynamics.

In the PS machine the effects of the coupling are reduced as the nonlinear elements are located in straight sections where the horizontal beta-function is twice as large as the vertical beta-function. This results in a coupling parameter $\chi = 0.5$. One can see in the mapping 3.5

that this reduces the nonlinear coupling effects. For this reason we shall set χ to this value in our simulations.

The settings for these simulations are similar to the ones for the 2D simulations: the tune variation is linear (from $\nu_x = 0.252$ to $\nu_x = 0.245$), the value of κ is kept constant and we scan over a large range of horizontal emittances. Of course we also consider different values of the vertical emittance.

The vertical tune is chosen to avoid resonances in the vertical plane and to avoid coupling resonances. It is therefore set to the nonresonant value 0.29 for all the simulations.

The results regarding the trapping fraction were fitted using an exponential model, as in the 2D case. Indeed, we observed that this fit is able to correctly reproduce the results for a large set of the parameters (number of turns, value of κ, and emittances).

7.2 Effects of the vertical emittance on the trapping fraction

Here we consider the same outputs as in the 2D case: the trapping fraction and the emittance sharing of the beamlets, but now we consider them for different values of the initial vertical beam emittance.

Figure 7.1 presents the results obtained with our numerical simulations. Each plots display the trapping fraction (and its fitted model) for different values of the vertical emittance. In addition we also display the losses (medium dots). Indeed the nonlinear coupling induces observable losses for the larger values of the vertical emittances. The figure compares these results for three values of κ and for two number of turns: 25000 turns, as we have seen in the 2D simulations this allows a large trapping fraction and a smaller value, 10000 turns.

We observe the impact of the vertical emittance: the larger the vertical emittance, the lower the trapping fraction and the higher the losses. Indeed, the nonlinearities of the 4D model reduce the dynamical aperture, *i.e.* the region of phase space surrounding the origin where the motion is bounded is reduced.

We observe however that for small vertical emittances ($\sigma_v = 0.01$ and $\sigma_v = 0.02$) the losses are limited and are below one percent, even for large horizontal emittances. On the other hand there is a steep increase in the losses when one go from $\sigma_v = 0.04$ to $\sigma_v = 0.06$.

We also observe an increase of the losses while we go from 10000 turns to 25000. At first this may seem strange, as we expect the process to be more adiabatic and to increase the trapping. This is due to the fact that particles with large vertical emittances can be located in chaotic regions during the process. These regions are unstable, as the orbits are not bounded, but the rate of divergence can be slow, therefore an increase in the number of turns can increase the losses, as it leaves more time for these particles to escape. This effect is directly linked to the more complex dynamics induced by the higher number of dimensions of the phase space.

This argument seem to be confirmed as we observe that the trapping fraction for small vertical emittances increase with the number of turns (as we concluded in the 2D simulations), but for larger vertical emittances, this higher trapping is counteracted by the increase in the losses.

The dependence on the value of κ is coherent with our conclusions for the 2D simulations but we also observe an additional effect: the losses are increased for small values of κ. In particular, if we compare the losses for $\kappa = -1.1$ and $\kappa = -1.9$, we observe a huger difference for the larger vertical emittance ($\sigma_v = 0.06$).

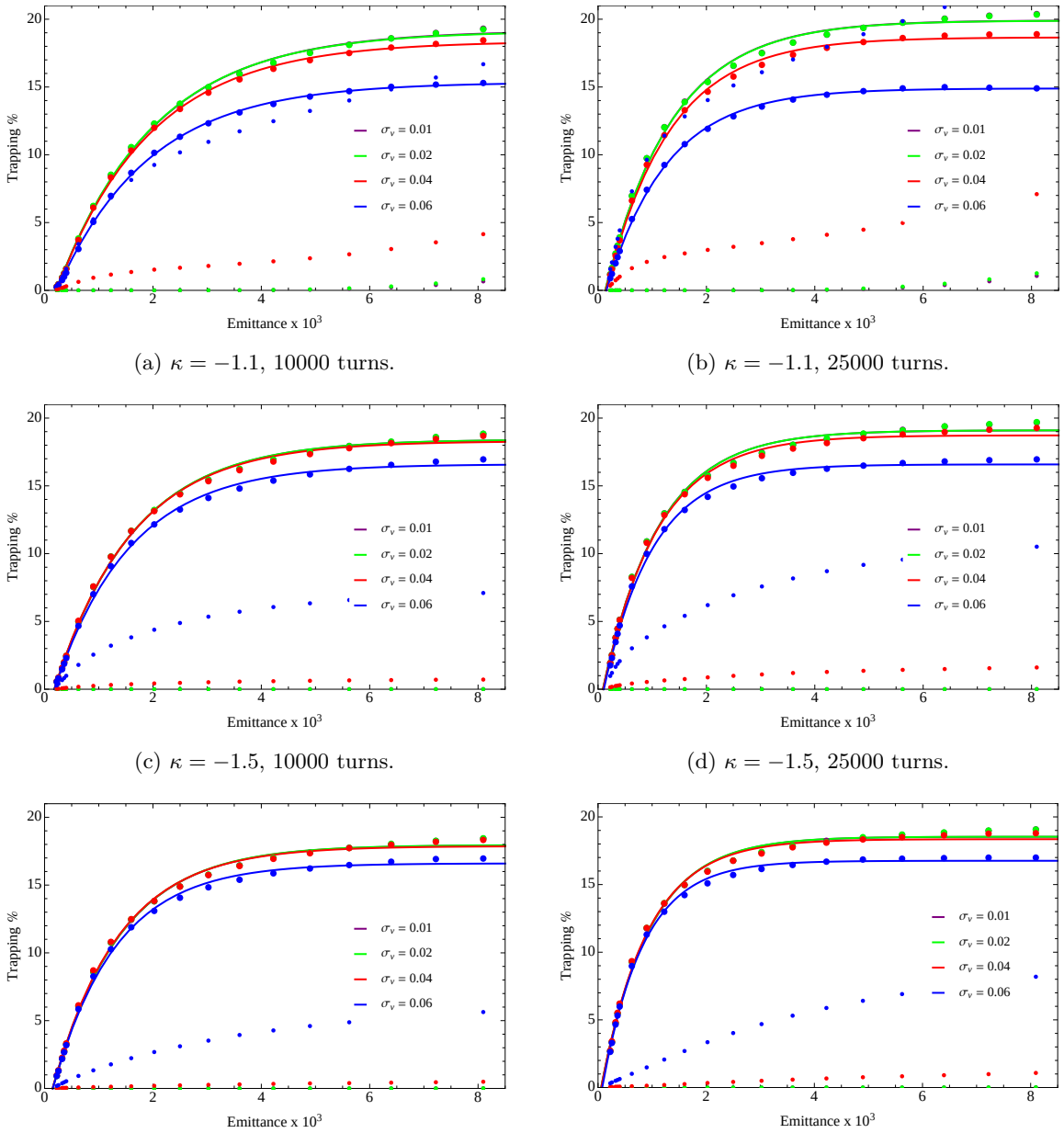

(a) $\kappa = -1.1$, 10000 turns.

(b) $\kappa = -1.1$, 25000 turns.

(c) $\kappa = -1.5$, 10000 turns.

(d) $\kappa = -1.5$, 25000 turns.

(e) $\kappa = -1.9$, 10000 turns.

(f) $\kappa = -1.9$, 25000 turns.

Figure 7.1: Trapping fraction (large dots and fits) and losses (small dots) for different values of κ and number of turns (Gaussian initial beam distribution).

7.3 Emittance sharing in 4D

As for the two-dimensional case, we consider here the emittance sharing between the core and the islands. Figure 7.2 displays the results obtained for different initial vertical beam emittances (and for various values of the parameter κ and of the number of turns). The emittances are expressed as the ratio of the emittance of the beamlet at the end of the process by the initial

horizontal beam emittance.

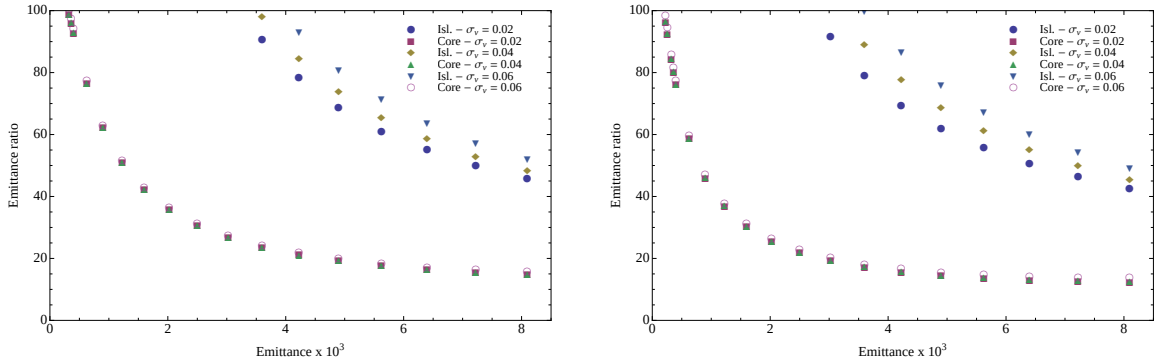

(a) $\kappa = -1.1$, 10000 turns.

(b) $\kappa = -1.1$, 25000 turns.

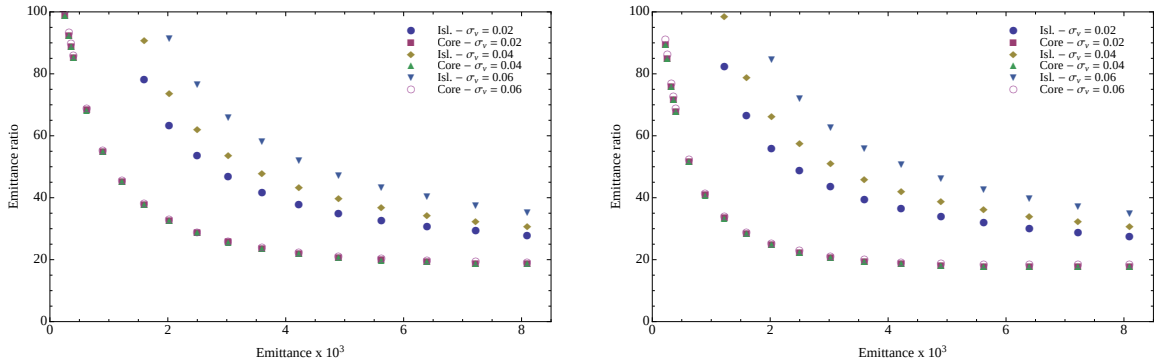

(c) $\kappa = -1.5$, 10000 turns.

(d) $\kappa = -1.5$, 25000 turns.

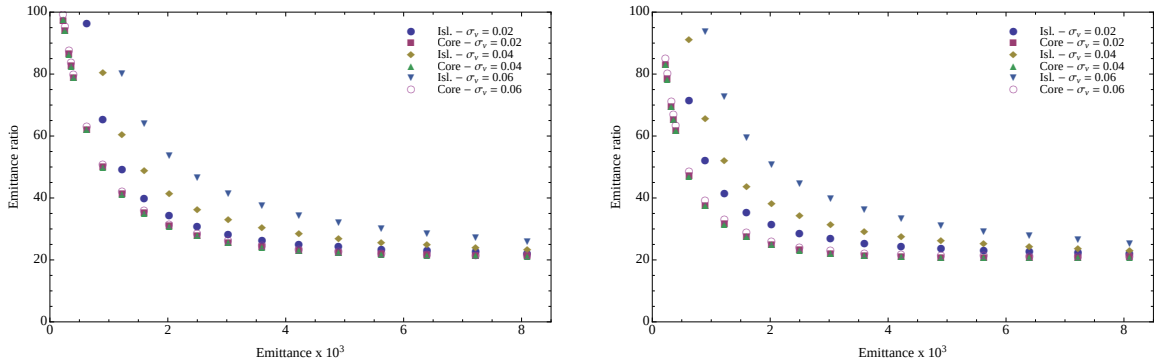

(e) $\kappa = -1.9$, 10000 turns.

(f) $\kappa = -1.9$, 25000 turns.

Figure 7.2: Horizontal emittance ratios of the core and of the islands.

Our first observation is that the emittance of the core is found to be almost independent on the initial vertical emittance. On the other hand, the emittance of the islands has a dependence on the vertical emittance: the higher the vertical emittance, the higher the resulting emittance of the island.

This increase can be interpreted if we consider that the nonlinear coupling between the horizontal and vertical planes depends on the amplitude in the vertical plane. Therefore a

particle with larger vertical amplitude will have a different horizontal tune than a particle with a smaller vertical amplitude.

The nonlinear coupling between the two planes leads to a coupling in the tunes [27]: the horizontal tune depends on the vertical amplitude (and on the horizontal amplitude) and vice versa. Therefore, in the horizontal phase space we do not have one set of islands at a given location but a superposition of islands whose fixed points are located at different horizontal amplitude, due to the fact that the beam is made of particles with different vertical amplitudes.

Following that argument we can understand why the emittance of the islands increases in case of beam of larger vertical emittance: this superposition lead to spread in the horizontal distribution of the particles of each beamlets.

We also observe that this effect is present for the different number of turns and for the different values of κ. The dependence on κ is found to be consistent with the analysis of the 2D case.

7.4 Evolution of the vertical emittance

A result that was not present in the 2D case is the final vertical beam emittance (of the "core", as the beam is not split in the vertical phase space). We found that the ratio of the final vertical emittance by the initial vertical emittance is greater than one; there is a blow-up of the vertical emittance. We analyze this effect and its dependence on the initial vertical emittance, initial horizontal emittance, value of κ and number of turns.

Figure 7.3 displays these results.

We observe a rather large blow-up for the small values of κ. Indeed, in the case $\kappa = -1.1$ it reaches 500% for 25000 turns. The blow-up for larger values of κ (in absolute value) is more limited.

An important feature of these results is the decrease of the blow-up with the initial vertical emittance and the reduction of the vertical emittance (ratio smaller than one) for the largest vertical emittance ($\sigma_v = 0.06$). We try to explain these results as follow:

- For a small initial vertical emittance, the initial beam does not fill the stable region of the phase space around the origin, in particular its projection in the YY' plane. Therefore, the process and the nonlinear coupling between the plane induce emittance blow-up as the beam is excited, resulting in a larger final vertical emittance. This effect is more limited for larger beams, as this excitation will quickly leads to losses, thus limiting the increase of the emittance;

- the decrease of the vertical emittance for the largest beam can be explained by the very large losses occurring in these cases (as discussed in section 7.2).

7.5 Digression: double resonance crossing

In 4D one also has the possibility to cross a resonance in both planes: crossing a resonant value for the horizontal tune, but also crossing a vertical resonant tune value using a variation of both tunes during the trapping process.

We performed simulations to show that this opens the possibility to create islands in the physical space (X, Y). To increase the effect of the nonlinearities on the vertical phase space, we set the coupling parameter χ to a higher value: $\chi = 0.7$. We also used a large value for κ:

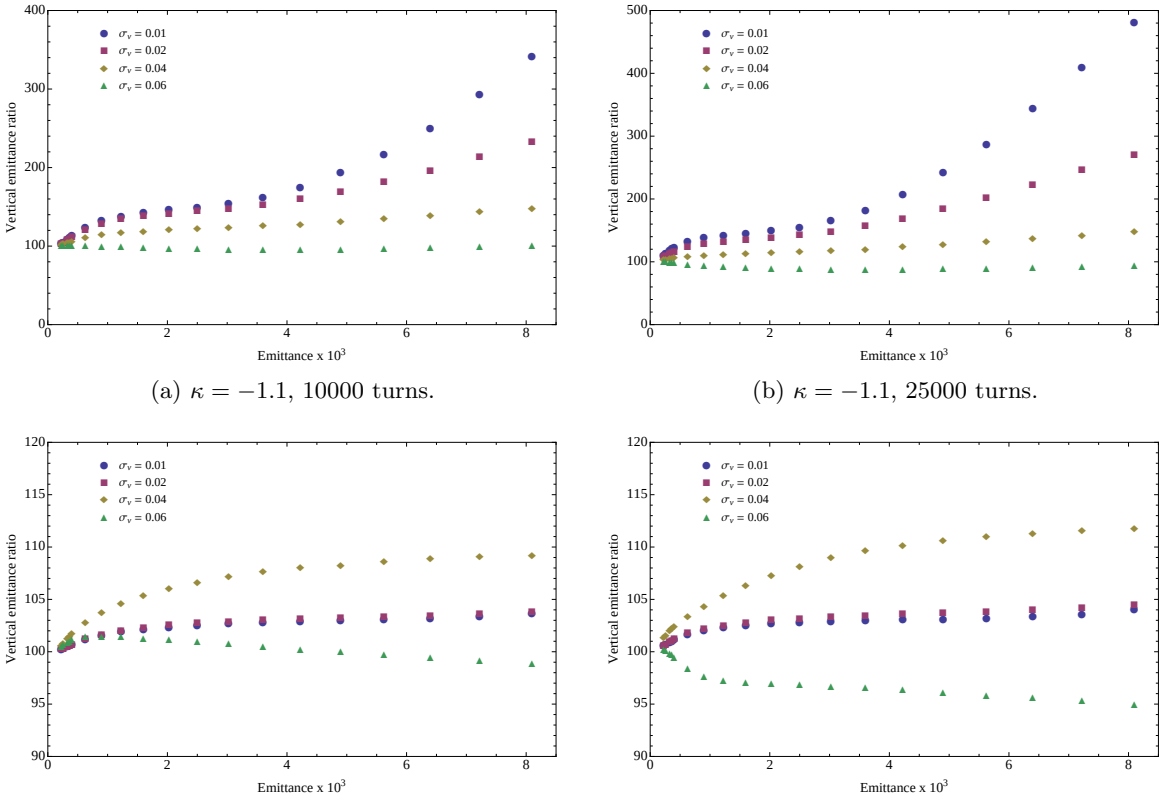

(a) $\kappa = -1.1$, 10000 turns.

(b) $\kappa = -1.1$, 25000 turns.

(c) $\kappa = -1.9$, 10000 turns.

(d) $\kappa = -1.9$, 25000 turns.

Figure 7.3: Vertical beam emittance as a function of the initial horizontal beam emittance. The plots compare the results obtained for different values of the initial vertical beam emittance (for different couples of the number of turns and value of κ).

$\kappa = -2.4$. These values of those two parameters allow the nonlinearities to have an important effect on the vertical dynamics in addition to the effect on the horizontal dynamics.

It should also be noted that due to opposite signs in the amplitude detuning for the two planes, we have to cross the vertical resonant tune from below if we cross the horizontal resonance from above (as we have to do for such a negative value of κ).

Figure 7.4 shows the results that we obtained for the final tunes $\nu_x = 0.245$ and $\nu_y = 0.256$.

One can observe the split beam in the different projections of the 4D phase space. In particular we note the presence of well separated islands in the physical space.

7.6 Conclusions on the 4D numerical studies

These four-dimensional results are coherent with our conclusions about the 2D cases. We analyzed the effect of the initial vertical beam emittance on the trapping fraction and on the emittances of the islands. We found that the nonlinear coupling has an impact on both the trapping fraction and the emittances: the larger the initial vertical emittance, the larger the resulting islands' emittances and the lower the trapping fraction.

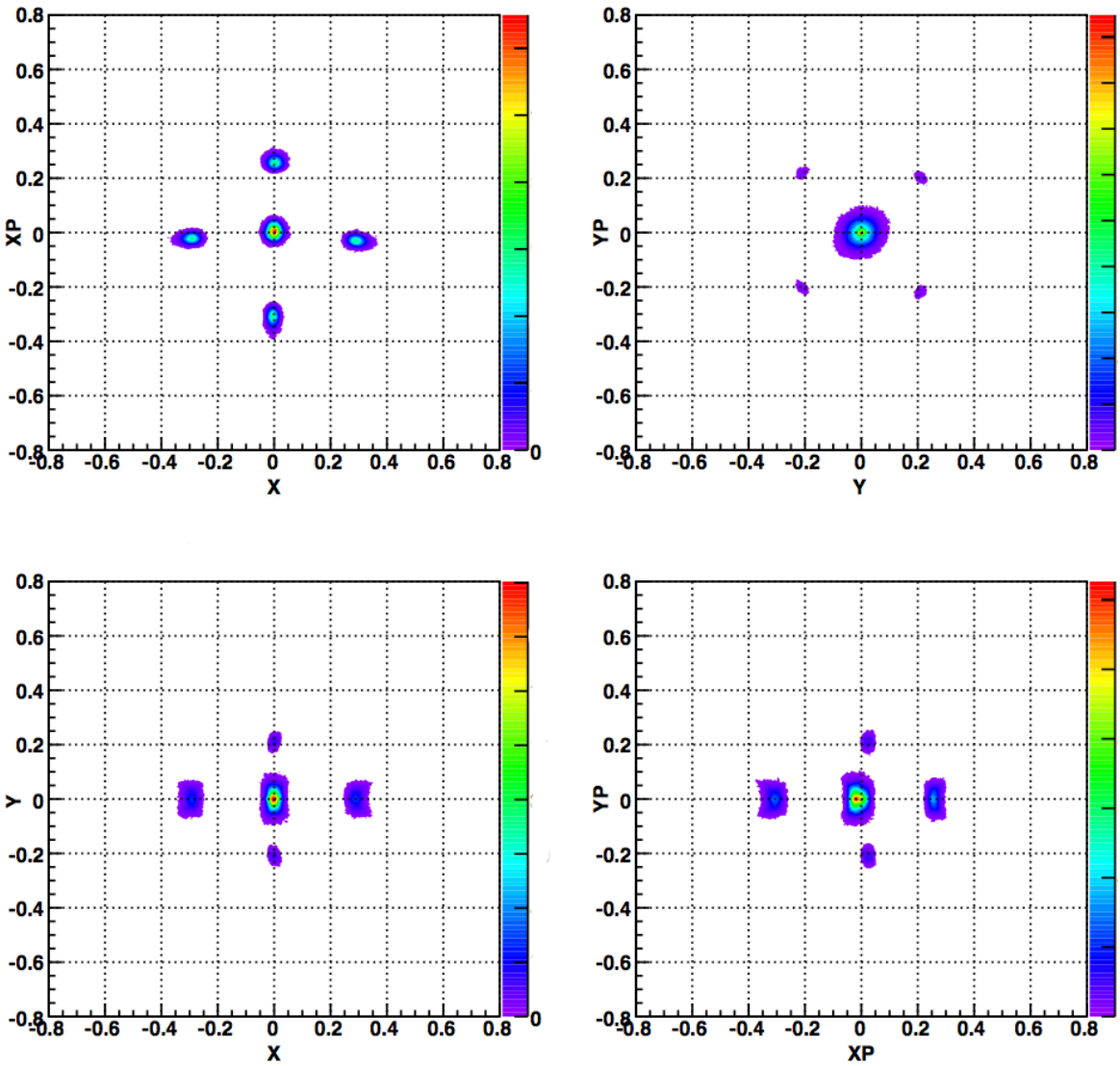

Figure 7.4: Split beam obtained with a double resonance crossing. We observe the islands in the physical space (bottom right histogram).

We were also able to conclude that the horizontal emittance of the core is practically independent on the initial vertical emittance.

In addition we also found an effect that was no present in the 2D simulations: the losses. Indeed we found that above a certain vertical emittance the losses become high and reduce the trapping in the islands.

Finally, we concluded on the vertical emittance blow-up as a function of the vertical emittance and we proposed an explanation based on the excitation of the beam due to the nonlinear coupling.

CHAPTER 8

Conclusion and perspectives

In this work we implemented analytical and numerical methods to study the trapping process at the heart of the MTE method. Our contributions in the developments presented in this thesis are threefold.

First we reviewed the Hamiltonian theory of the transverse beam dynamics and the transfer map formalism. The understanding of these results allowed considering the models used to describe the MTE method in a general context while also understanding the successive approximation that are involved. Such an analysis allows one to understand the limitations of the ideal model with respect to the actual dynamics of the PS beam.

In addition we were able to gain a better understanding of the trapping process using the Normal Form approach. We considered an analysis of the interpolating Hamiltonian of the Hénon map normal form. The validity of the computation of all the normal form coefficients that we used as been assessed using the numerical values given by the code GIOTTO. We compared the outputs of this analysis with numerical estimates of the properties of the Hénon map and we were able to conclude that the usual approach, at the lowest perturbation order is not valid for the fourth order resonance due to the peculiarities of this resonance. This conclusion was validated using a normal form model of the fifth order resonance and it was found that in that case the approach provides a better agreement regarding the position of the fixed points.

Efforts were also devoted to the numerical analysis of the properties of the trapping. For this purpose we developed and exploited a tracking code able to explore new settings of the parameters of the mapping. This code was successfully used to perform a large campaign of 2D and 4D simulations. From intense use of this code we concluded that the goals set during the design of the code, flexibility and performances, were met.

From the results obtained by our 2D simulations we were able to suggest a way to obtain a split beam with improved properties compared with the usual 2D beam splitting: efficient trapping and emittance sharing. Indeed it was found that the use a polynomial tune variation and a linear variation of the strength of the nonlinearities during the splitting allows to obtain optimized values of both the trapping and the emittances. The 4D simulations have validated this approach, as the results found in these simulations were coherent with our previous

conclusions. Furthermore we used these 4D simulations to put in evidence two mechanisms absent from the two-dimensional cases: the presence of beam losses and the vertical emittance blow-up.

APPENDIX A

Formal computation of Normal Form coefficients

In this appendix we give the coefficients of the Normal Forms and conjugating functions associated to the Hénon mapping. In section A.1 we compute the coefficients in the quasi-resonant case of the fifth order resonance. For information, in section A.2 we display the coefficients in the nonresonant case.

A.1 Quasi-resonant Normal Form (fifth order resonance)

Following the same derivations as for the fourth order case (section 4.2) we obtained the coefficients of the quasi-resonant normal form (and its conjugating function) for the fifth order resonance. Here we display our results.

The normal form expanded up to the first resonant term reads

$$U(\zeta,\zeta^*) = e^{i\omega}\zeta + u_{2,1}\zeta^2\zeta^* + u_{0,4}\zeta^{*4} \tag{A.1}$$

due to the condition (3.13). We observe that we need to go to the fourth order to make the resonant term appear.

A.1.1 Conjugating function

The coefficients of the conjugating function are given by

$$\begin{cases} \phi_{2,0} = \frac{1}{8}\left[-\cot\frac{\omega}{2} + i\right] \\ \phi_{1,1} = \frac{1}{4}\left[\cot\frac{\omega}{2} + i\right] \\ \phi_{0,2} = \frac{1}{8}\left[\cot\frac{3\omega}{2} + i\right]. \end{cases} \tag{A.2}$$

and

$$\begin{cases} \phi_{3,0} = \frac{i\left(-2\kappa+\cot\frac{\omega}{2}-\cot\frac{3\omega}{2}\right)}{16(-1+e^{2i\omega})} \\ \phi_{2,1} = \frac{1}{64}\left(-\cot^2\frac{\omega}{2}+\cot^2\frac{3\omega}{2}\right) \\ \phi_{1,2} = -\frac{i\left(6\kappa+3\cot\frac{\omega}{2}+\cot\frac{3\omega}{2}\right)}{16(-1+e^{-2i\omega})} \\ \phi_{0,3} = 0. \end{cases} \tag{A.3}$$

We do not report the fourth order coefficients here as they are particularly long. They are available as a Mathematica notebook [51].

A.1.2 Normal form

The nonresonant term is given by

$$u_{2,1} = -\frac{1}{16}ie^{i\omega}\left(6\kappa+3\cot\frac{\omega}{2}+\cot\frac{3\omega}{2}\right). \tag{A.4}$$

The resonant coefficient $u_{0,4}$ is obtained from the conjugation equation projected at the fourth order. It reads

$$\begin{aligned} u_{0,4} = \quad & \phi_{2,0}^{*2}f_{0,2} + 2\phi_{3,0}^{*}f_{0,2} \\ & +3\phi_{2,0}^{*}f_{0,3} + \phi_{2,0}^{*}f_{1,1}\phi_{0,2} + f_{1,2}\phi_{0,2} \\ & +f_{2,0}\phi_{0,2}^{2} + f_{1,1}\phi_{0,3} - e^{-4i\omega}\phi_{0,4} + e^{i\omega}\phi_{0,4}. \end{aligned} \tag{A.5}$$

A.2 Nonresonant Normal Form

We provide here the coefficients of the nonresonant normal form for the cubic Hénon mapping.

The nonresonant normal form reads

$$U(\zeta,\zeta^*) = e^{i\omega}\zeta + u_{2,1}\zeta^2\zeta^*. \tag{A.6}$$

A.2.1 Conjugating function

The coefficients of the conjugating function are given, up to order three, by

$$\begin{cases} \phi_{2,0} = \frac{1}{8}\left[-\cot\frac{\omega}{2}+i\right] \\ \phi_{1,1} = \frac{1}{4}\left[\cot\frac{\omega}{2}+i\right] \\ \phi_{0,2} = \frac{1}{8}\left[\cot\frac{3\omega}{2}+i\right]. \end{cases} \tag{A.7}$$

and

$$\begin{cases} \phi_{3,0} = \frac{i}{16}\frac{1}{e^{2i\omega}-1}\left(\cot\frac{\omega}{2}-\cot\frac{3\omega}{2}-2\kappa\right) \\ \phi_{2,1} = \frac{1}{64}\left(\cot^2\frac{3\omega}{2}-\cot^2\frac{\omega}{2}\right) \\ \phi_{1,2} = -\frac{i}{16}\frac{1}{e^{-2i\omega}-1}\left(3\cot\frac{\omega}{2}-\cot\frac{3\omega}{2}-2\kappa\right) \\ \phi_{0,3} = \frac{i}{16}\frac{1}{e^{-4i\omega}-1}\left(\cot\frac{\omega}{2}-\cot\frac{3\omega}{2}-2\kappa\right). \end{cases} \tag{A.8}$$

A.2.2 Normal Form

The nonlinear coefficient of the normal form $u_{2,1}$ is given by

$$u_{2,1} = -\frac{1}{16} i e^{i\omega} \left(6\kappa + 3\cot\frac{\omega}{2} + \cot\frac{3\omega}{2} \right). \tag{A.9}$$

From $u_{2,1}$ we write the first term of the amplitude dependent frequency:

$$\Omega_2 = \frac{1}{16} \left(-6\kappa - 3\cot\frac{\omega}{2} - \cot\frac{3\omega}{2} \right). \tag{A.10}$$

APPENDIX B

Typical simulation input file for Manzoni

This appendix reproduces a typical simulation input file that was used for the 4D studies of the Hénon mapping. Chapter 5 discuses the related concepts.

B.1 Input file

```
<?xml version='1.0'?>
<manzoniSimulation name='4d linear resonance crossing simulations'>
  <!-- Global configuration for Manzoni -->
  <manzoni>
    <global>
      <!-- Every output path is relative to this path -->
      <path>campaigns</path>
    </global>
    <simulation>
      <dates>
        <created>2010-08-26</created>
        <launched>2010-08-27</launched>
      </dates>
      <description>
        Basic 4D campaign with linear resonance crossing.
      </description>
    </simulation>
  </manzoni>
  <flows>
    <alessandroFlow>
    <!-- Important to kill lost particles -->
    <phaseSize>1</phaseSize>
    <!-- Independent of the previous one, used by the plots -->
    <windowSize>0.80</windowSize>
```

```
<dataProcessing>
  <!-- Data processing done before the tracking -->
  <initial>
    <!-- Moment of the initial beam distribution -->
    <islands file='islands_initial'>
      <analysis>
        <planes>XXP</planes>
        <boxes>
          <!-- Box size used for the recognition of the islands -->
          <size>1</size>
          <horizontal>1</horizontal>
          <vertical>1</vertical>
        </boxes>
        <islands>
          <i>1</i>
        </islands>
      </analysis>
      <analysis>
        <planes>YYP</planes>
        <boxes>
          <!-- Box size used for the recognition of the islands -->
          <size>1</size>
          <horizontal>1</horizontal>
          <vertical>1</vertical>
        </boxes>
        <islands>
          <i>1</i>
        </islands>
      </analysis>
      <moments/>
      <derived/>
    </islands>
    <!-- Histograms of the initial beam distribution -->
    <distrHist title='Initial distribution' file='hist1.pdf'>
      <projection>XXP</projection>
      <projection>YYP</projection>
      <projection>XY</projection>
    </distrHist>
  </initial>
  <!-- Data processing done at some point during the tracking -->
  <intermediate/>
  <!-- Data processing done at the end of the tracking -->
  <final>
    <!-- Beam distribution -->
    <distrHist title='Final distribution' file='hist3.pdf'>
      <projection>XXP</projection>
      <projection>YYP</projection>
      <projection>XY</projection>
      <projection>XPYP</projection>
    </distrHist>
    <!-- Population and moments of the islands -->
    <islands file='islands'>
      <analysis>
```

```
78              <planes>XXP</planes>
                <boxes>
                  <!-- This size depends on kappa -->
81                <size>0.42</size>
                  <horizontal>3</horizontal>
                  <vertical>3</vertical>
84              </boxes>
                <islands>
                  <i>1</i>
87                <i>2</i>
                  <i>3</i>
                  <i>4</i>
90                <i>5</i>
                  <i>6</i>
                  <i>7</i>
93                <i>8</i>
                  <i>9</i>
                </islands>
96            </analysis>
              <analysis>
                <planes>YYP</planes>
99              <boxes>
                  <size>1.0</size>
                  <horizontal>1</horizontal>
102               <vertical>1</vertical>
                </boxes>
                <islands>
105               <i>1</i>
                </islands>
              </analysis>
108           <moments/>
              <derived/>
            </islands>
111       </final>
        </dataProcessing>
        <!-- Parameters of the beam distribution -->
114     <initialDistribution dimensions='4' type='gaussian'>
          <horizontal>
            <centroid>
117           <X>0</X>
              <XP>0</XP>
            </centroid>
120         <sigmas>
              <X>0.08</X>
              <XP>0.08</XP>
123         </sigmas>
            <density>45</density>
          </horizontal>
126       <vertical>
            <centroid>
              <Y>0</Y>
129           <YP>0</YP>
            </centroid>
```

```
        <sigmas>
132       <Y>0.04</Y>
          <YP>0.04</YP>
        </sigmas>
135     <density>45</density>
      </vertical>
    </initialDistribution>
138 <!-- Parameters of the tracking -->
    <iterator plot='yes' kicks='1'>
      <turns>15000.0</turns>
141   <intermediateTurns>10000</intermediateTurns>
      <!-- These values (partial tunes) are used to -->
      <!-- rotate the coordinate system if one      -->
144   <!-- want to have islands at a given position -->
      <phaseAdjustment>
        <horizontal>-0.13</horizontal>
147     <vertical>0.0</vertical>
      </phaseAdjustment>
      <!-- Implicit limitation: the first kick must contain a non linearity -->
150   <!-- Otherwise the normalization does not make sense -->
      <kick0 type='SO'>
        <!-- This normalization (of the first kick) -->
153     <!--        is used for the dimensionless    -->
        <!--        coordinates normalization.       -->
        <!-- Sextupolar normalization -->
156     <lambda unit='m1/2'>1</lambda>
        <!-- Octupolar coefficient -->
        <kappa unit='' curveType='fixed'>
159       <value>-1.8</value>
        </kappa>
        <!-- Ratio of the beta functions -->
162     <chi>0.5</chi>
        <!-- Horizontal phase advance -->
        <nuHorizontal curveType='linear'>
165       <start>0.252</start>
          <end>0.245</end>
        </nuHorizontal>
168     <!-- Vertical phase advance -->
        <nuVertical curveType='fixed'>
          <value>0.29</value>
171     </nuVertical>
      </kick0>
    </iterator>
174 </alessandroFlow>
  </flows>
</manzoniSimulation>
```

Bibliography

[1] CERN, *CAS - CERN Accelerator School: Intermediate Course on Accelerator Physics*, (Geneva), CERN, 2006.

[2] "Cern document server." http://cdsweb.cern.ch/record/951445, 2011.

[3] H. Wiedemann, *Particle accelerator physics*. Springer Verlag, 2007.

[4] "The MAD-X homepage." http://mad.web.cern.ch, 2011.

[5] "The CERN website." http://www.cern.ch, 2011.

[6] M. Giovannozzi, D. Quatraro, and G. Turchetti, "Generating unstable resonances for extraction schemes based on transverse splitting," *Phys. Rev. ST Accel. Beams*, vol. 12, p. 024003, Feb 2009.

[7] "Proton synchrotron straight sections pictures." http://psring.web.cern.ch/psring/psring/pscomplex.shtml.

[8] "Cern PS Vistar." http://op-webtools.web.cern.ch/op-webtools/vistar, 2011.

[9] D. Manglunki and M. Giovannozzi, "Ps 50 years: Beam extraction," 2010.

[10] K. e. a. Elsener, *The CERN neutrino beam to Gran Sasso (NGS): conceptual technical design*. Geneva: CERN, 1998.

[11] M. Giovannozzi, M. J. Barnes, O. E. Berrig, A. Beuret, J. Borburgh, P. Bourquin, R. Brown, J. P. Burnet, F. Caspers, J. M. Cravero, T. Dobers, T. Fowler, S. S. Gilardoni, M. Hourican, W. Kalbreier, T. Kroyer, F. Di Maio, M. Martini, V. Mertens, E. Métral, K. D. Metzmacher, C. Rossi, J. P. Royer, L. Sermeus, R. Steerenberg, G. Villiger, and T. Zickler, *The CERN PS multi-turn extraction based on beam splittting in stable islands of transverse phase space: Design Report*. Geneva: CERN, 2006.

[12] S. Gilardoni, M. Giovannozzi, M. Martini, E. Métral, P. Scaramuzzi, R. Steerenberg, and A. Muller, "Resonant multi-turn extraction: Principle and experiments.," *Nucl. Instrum. Methods Phys. Res., A*, vol. 561, Sep 2005.

[13] G. Servizi, D. Bortolotti, E. Todesco, M. Giovannozzi, and M. Vrahatis, "GIOTTO: A Code for the Nonlinear Analysis of Area-Preserving Mappings," *International Journal of Modern Physics C-Physics and Computer*, vol. 6, no. 5, pp. 651–662, 1995.

[14] S. Y. Lee, *Accelerator Physics; 2nd ed.* London: World Scientific, 2004.

[15] P. Germain, D. Dekkers, and D. Manglunki, *Introduction aux accélérateurs de particules.* Geneva: CERN, 1989.

[16] CERN, *CAS - CERN Accelerator School: General Accelerator Physics, v.1*, (Geneva), CERN, 1985. distribution.

[17] CERN, *CAS - CERN Accelerator School : 5th General Accelerator Physics Course*, (Geneva), CERN, 1994. distribution.

[18] CERN, *CAS - CERN Accelerator School : 50 Years of Synchrotrons*, (Geneva), CERN, 1997. Early synchrotrons in Britain. Early work for CERN/J Lawson ; The CERN synchrotrons/G Brianti. - short version of RAL-97-011.

[19] Y.-P. Sun, R. Assmann, J. Barranco, R. Tomás, T. Weiler, F. Zimmermann, R. Calaga, and A. Morita, "Beam dynamics aspects of crab cavities in the cern large hadron collider," *Phys. Rev. ST Accel. Beams*, vol. 12, p. 101002, Oct 2009.

[20] W. Herr and F. Schmidt, "A MAD-X primer," *CAS - CERN Accelerator School: Intermediate Course on Accelerator Physics, Zeuthen, Germany*, p. 32 p, Jun 2004.

[21] D. A. Edwards and M. J. Syphers, *An introduction to the Physics of High Energy Accelerators.* Wiley Beam Phys. Accel. Technol., New York, NY: Wiley, 1993.

[22] J. R. Rees, "Symplecticity in beam dynamics: An introduction," 2003. SLAC-PUB-9939.

[23] H. Goldstein, C. Poole, and J. Safko, *Classical Mechanics; 3rd ed.* San Francisco, CA: Addison-Wesley, 2002.

[24] J. José and E. Saletan, *Classical dynamics: a contemporary approach.* Cambridge University Press, 1998.

[25] A. Streun, "The simplified Hamiltonian for transverse beam dynamics," pp. 1–8, oct 2010.

[26] J. Bengtsson, "The sextupole scheme for the Swiss Light Source (SLS): an analytic approach," *SLS Note*, vol. 9, p. 97, 1997.

[27] A. Bazzani, G. Servizi, E. Todesco, and G. Turchetti, *A normal form approach to the theory of nonlinear betatronic motion.* Geneva: CERN, 1994.

[28] M. Giovannozzi and J. Morel, "Principle and analysis of multiturn injection using stable islands of transverse phase space," *Phys. Rev. ST Accel. Beams*, vol. 10, p. 034001, Mar 2007.

[29] D. J. Simon, "The cern ps complex: a versatile particle factory," p. 4 p, Jun 1996.

[30] E. Regenstreif, *Le synchrotron à protons du CERN, pt.1.* Geneva: CERN, 1958. English version published as CERN 59-29.

[31] R. Cappi and M. Giovannozzi, "Novel method for multiturn extraction: Trapping charged particles in islands of phase space," *Physical review letters*, vol. 88, no. 10, p. 104801, 2002.

[32] R. Cappi and M. Giovannozzi, "Multiturn extraction: performance analysis of old and new approaches," *Nuclear Instruments and Methods in Physics Research Section A: Accelerators, Spectrometers, Detectors and Associated Equipment*, vol. 519, no. 1-2, pp. 442–452, 2004.

[33] R. Cappi and M. Giovannozzi, "Multiturn extraction and injection by means of adiabatic capture in stable islands of phase space," *Phys. Rev. ST Accel. Beams*, vol. 7, p. 024001, Feb 2004.

[34] A. Franchi, S. Gilardoni, and M. Giovannozzi, "Progresses in the studies of adiabatic splitting of charged particle beams by crossing nonlinear resonances," *Phys. Rev. ST Accel. Beams*, vol. 12, p. 014001, Jan 2009.

[35] M. Giovannozzi, "Design and tests of a low-loss multi-turn ejector for the cern ps.," Tech. Rep. CERN-AB-2006-021, CERN, Geneva, May 2006.

[36] S. Gilardoni, M. Giovannozzi, M. Martini, E. Métral, P. Scaramuzzi, R. Steerenberg, and A.-S. Müller, "Experimental evidence of adiabatic splitting of charged particle beams using stable islands of transverse phase space," *Phys. Rev. ST Accel. Beams*, vol. 9, p. 104001, Oct 2006.

[37] M. Henon, "Numerical study of quadratic area-preserving mappings," *Quarterly of applied mathematics*, vol. 27, pp. 291–312, 1969.

[38] S. Tzenov, *Contemporary accelerator physics*. World Scientific Pub Co Inc, 2004.

[39] V. Arnold, V. Kozlov, and A. Neishtadt, *Mathematical Aspects of Classical and Celestial Mechanics*. Springer-Verlag., 2006.

[40] F. Schmidt, C. Y. Chiu, B. Goddard, D. Jacquet, V. Kain, M. Lamont, V. Mertens, J. Uythoven, and J. Wenninger, "MAD-X PTC integration," *21st IEEE Particle Accelerator Conference*, p. 4 p, Jul 2005.

[41] M. Giovannozzi. Personal communication, 2010.

[42] "The GSL - GNU Scientific Library homepage." http://www.gnu.org/software/gsl/, 2011.

[43] T. Veldhuizen, "The Blitz++ homepage." http://www.oonumerics.org/blitz/, 2011.

[44] T. A. project, "The Xerces-C++ XML Parser homepage." http://xerces.apache.org/xerces-c/, 2011.

[45] T. R. Team, "The ROOT homepage." http://root.cern.ch, 2011.

[46] "The ruby programming language." http://www.ruby-lang.org, 2011.

[47] "The CERN batch system website." http://batch.web.cern.ch, 2011.

[48] M. Giovannozzi, "Fortran code for mte simulations." Personal communication, 2010.

[49] C. K. Allen and T. P. Wangler, "Beam halo definitions based upon moments of the particle distribution," *Phys. Rev. ST Accel. Beams*, vol. 5, p. 124202, Dec 2002.

[50] R. Bartolini and F. Schmidt, "A computer code for frequency analysis of non-linear betatron motion," Tech. Rep. SL-Note-98-017-AP, CERN, Geneva, Feb 1998.

[51] C. Hernalsteens, "Mathematica notebook for the normal form coefficients." Personal communication, 2011.

Index

MTE, 34

Accelerator complex, 34

Betatron, 6

CNGS, 40
Commutation diagram, 53
Conjugating function, 53
Coupling, 68
CT extraction, 41
Cyclotron, 4, 6

Design orbit, 7
Dipole magnet, 8
Dynamics, 3, 10

Emittance, 69

Fast extraction, 38
Fourier analysis, 70

Hénon, 45
Hénon map, 45
Hénon mapping, 45
Hamiltonian, 14, 58
Hill's equation, 12

Interpolating Hamiltonian, 58

Manzoni, 63, 64, 104
Microtron, 6
MTE, 42
Multi-Turn extraction, 34
Multi-turn extraction, 40

Nonresonant normal form, 55
Normal Form, 52
Normal form, 53
Normal form (definition), 53
Normal form (formal), 55
Normal form of Hénon map, 56

Orbit, 7

Poincaré, 24
Poincaré map, 24
Proton Synchrotron, 36
PS, 36

Quasi-resonant normal form, 56

Resonant normal form, 55

Slow extraction, 39
SPS, 41
Symplectic map, 23
Symplectic matrix, 23
Symplecticity, 23
Synchrotron, 3, 5, 6

Tracking, 24
Tracking code, 63, 65
Transfer map, 22
Transverse dynamics, 3